TiO_2-BASED PHOTOCATALYSTS AND PHOTO-REACTIVE COATINGS FOR WATER AND AIR CLEANING

PHD THESIS

ÁGNES VERES
Environmental scientist

Supervisor: Dr. Imre Dékány
Full professor,
Member of Hungarian Academy of Sciences

UNIVERSITY OF SZEGED
Faculty of Science and Informatics
Doctoral School of Chemistry
2015
Szeged

Table of content

1. Introduction

Pollution of water and air due to intensive human activity is undoubtedly a major concern worldwide. This challenge urges the scientific community to look for sustainable, green solutions to obtain the purity of these media without exposing more strain on the environment. To produce drinking water for human consumption, a wide range of toxic compounds have to be eliminated such as pathogens, viruses, bacteria, pharmaceutical compounds and a variety of chemicals originating from industrial and household activities. The current methods to process drinking water require a huge amount of energy and money and they often include addition of chlorine, which can also relate to health issues, moreover, these technologies are not or partially available in developing countries. Considering several industrial activities, emission of toxic wastes into our natural waters is also an unsolved problem having adverse influence on aquatic life. Unfortunately, the same implies on the emission of toxic chemicals into the air, which is heavily noticed especially in highly populated and industrial areas, causing severe problems such as asthma and other health related issues. Undoubtedly, there is an urgent need for the development of safe, sustainable and efficient protocols to purify these media without putting more strain on the environment. Related to air pollution problems, there is also an increasing concern on indoor air pollution which has an increasing relevance in daily life as most people are spending a vast amount of their time in poorly ventilated offices, work environment, public places or in their homes.

Photocatalysis offers promising solution to reduce the level of unwanted compounds both in air and water. For this purpose, semiconductor nanomaterials, especially titanium dioxide (TiO_2) has attracted a lot of attention. Thanking to the fact that the properties and thus the optical and the electronic properties of the submicron sized semiconductor particles are exceedingly different than that of the bulk, thus these materials have exciting properties and provide possible alternatives for solar applications with high relevance to fields such as energy and environment.

2. Literature overview

Heterogeneous photocatalysis has received growing popularity due to its wide-ranged practical interest in applications including disinfection of water and air [1] hydrogen and solar chemical production [2-3], artificial photosynthesis (CO_2 reduction) [4-5] production of electrochemical energy, [6] construction of functional surfaces such as antibacterial [7-8] and anti-fogging [9-10] surfaces and many others. Photocatalysis using TiO_2 has an established role among Advanced Oxidation Processes

(AOPs) [11] besides UV-or vacuum- UV (VUV) photolysis [12] with or without the use of H_2O_2 and O_3, photo-Fenton [13] reaction and radiolysis techniques. [14] The advantage of these techniques that due to the generation of reactive radicals the process is non-selective, therefore oxidation of organic compounds and non-biodegradable toxic soluble pollutants can be facilitated by means of these processes and it can be effectively used as a pre-treatment step to enhance biodegradation of recalcitrant organic pollutants prior to biological water treatment.

Despite of the widespread interest, heterogeneous photocatalysis to be applied as a part of current water cleaning technologies is still delayed and several key technical challenges need to be solved first which are low photonic efficiency, especially under Vis light irradiation; separation/immobilisation of the photocatalyst; limitation of activity by pH of the reaction medium. Basically, better photocatalyst design with higher activity, new integrated or coupling system for enhanced photo-mineralisation or photo-disinfection kinetics, furthermore efficient design of photocatalytic reactor systems are required. [15]

2.1. Fundamentals of photocatalysis on TiO_2

The term photocatalysis refers to reactions where photons are absorbed by the solid, which remains unchanged during the entire reaction and induce chemical transformation of the surrounding compounds. From the thermodynamic point of view, "catalysis" is limited to those reactions which can be described with a negative Gibbs energy change ($\Delta G < 0$) and decrease of activation energy of the chemical reaction by the catalyst. In this sense, the solid can act as a catalyst under light, therefore the term photocatalysis is adequate. [16] However, there are certain reactions regarded as "photocatalytic", which are energy-storing (such as splitting of water), therefore these reaction should not be nominated as "photocatalytic".[17] Nevertheless, the term *photocatalysis* is widely used to describe the process in which the acceleration of a reaction occurs when a material, usually a semiconductor, interacts with light having sufficient energy to produce reactive oxygen species (ROS) which can lead to the photocatalytic transformation of pollutants. [18] It has been a widely investigated area since Fujishima and Honda reported water splitting on TiO_2 photoanode, without applying external bias, in *Nature* in 1972. [19] TiO_2 was first used for environmental remediation in 1977 when Frank and Bard reported that it was used for the oxidisation of CN^- in water. [20]

TiO_2 is an n-type semiconductor due to the small amount of oxygen vacancies in the crystalline phase which is compensated by the presence of Ti^{3+} centres. [21-22] Owing to the semiconductor nature, TiO_2 can be widely applied in electrochemical and redox reactions. Semiconductors are differentiated from conductors and insulators by their special electronic band structure. Typically, TiO_2 possesses a valance band (VB), which is formed by the overlapping of the oxygen 2p orbitals, and a conduction

band (CB), which is constituted by the 3d orbitals of Ti^{4+}cations. A "forbidden" energy level called *band gap*, is located between the aforementioned energy states where no electrons can be found in any circumstances. The "size" of band gap is described by the band gap energy (E_g, eV) which is representative of the catalyst and determined mostly by the crystal structure. When the solid is irradiated with light, possessing energy, high enough to overcome the band gap energy (E_g) of the semiconductor, the electron (e^-) in the filled VB is promoted to the empty CB, leaving a positive hole (h^+) behind. The process is demonstrated in *Figure 1*. As TiO_2 is a typical wide band gap semiconductor, the energy of incoming photons is required to be fairly high, i.e., at least 3.2 eV and 3.0 eV for anatase and for rutile, respectively, to overcome the band gap energy of the semiconductor. The as-generated charges carriers (*excitons*) initiate the production of reactive oxygen species (ROS) in contact with water or molecular oxygen, according to Eq 1-2:

$$h_{VB+} + H_2O \rightarrow {}^{\bullet}OH + H^+ \qquad \text{Equation 1}$$

and

$$e_{CB}- + O_2 \rightarrow {}^{\bullet}O_2- \qquad \text{Equation 2}$$

These ROS play the most important role in the degradation and eventual mineralisation of the adjacent organic molecules (Eq. 3-4):

$$^{\bullet}OH + \text{pollutant} \rightarrow \rightarrow \rightarrow CO_2 + H_2O \qquad \text{Equation 3}$$

$$^{\bullet}O_2^- + \text{pollutant} \rightarrow \rightarrow \rightarrow CO_2 + H_2O \qquad \text{Equation 4}$$

but the oxidation or reduction of the substrates can occur on the surface of the semiconductor through direct chemical interactions with the charge carriers. However this latter process has a lower chance to happen because the substrate needs to be in direct contact with the semiconductor NP, whereas ROS possess some mobility up to a certain extent. Nevertheless, the photo-electrochemical reactions need to be thermodynamically favoured which is dependent on the relative relationship between the band energy positions of the semiconductor and the redox potential of the adsorbed species. The relevant potential level of the acceptor species needs to be below (more positive than) the CB and the potential level of the donor species needs to be above (more negative than) the VB position of the semiconductor. [22, 23, 24] The potential of holes in the VB is low enough to oxidise most of the organic compounds, therefore, TiO_2 is applicable to decompose a variety of organic pollutants.

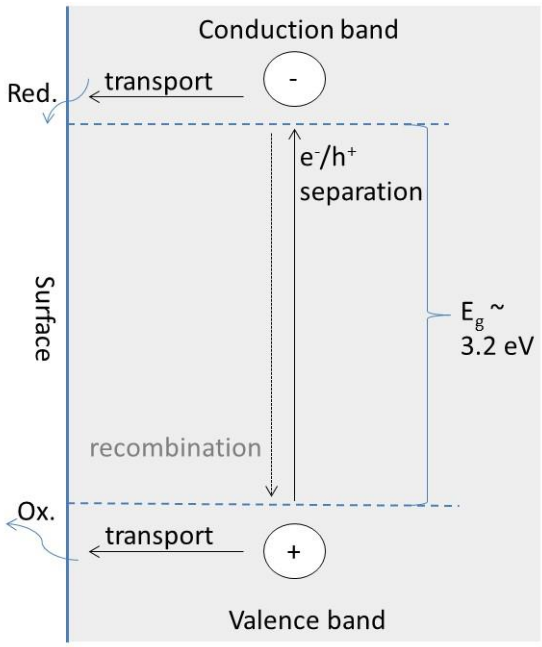

Figure 1 Scheme of electron – hole separation on anatase TiO_2

It is crucial on the photocatalytic process that the charge carriers reach the surface, because without this to occur, the photocatalytic reaction will not happen. Very often these excitons will undergo recombination which is one of the major limitations in the semiconductor photocatalysis, decreasing the overall quantum efficiency. [23] The recombination sometimes happens through radiative mechanisms to dissipate energy in the form of light or heat according to Eq 5:

$$e^-_{CB} + h^+_{VB} \rightarrow \text{energy} \qquad \text{Equation 5}$$

Nonetheless, the original structure (or chemical composition) of semiconductor remains unchanged if equal number of electrons and holes are consumed for chemical reaction and/or recombination. [25]

2.2. Physical and chemical properties of TiO_2 that influence its photocatalytic activity

Photocatalytic activity is a function of several physical and chemical properties of the NPs and it is not possible to try to determine it by one or three properties. However, if it is possible to strictly narrow down the question, the photocatalytic activity of a semiconductor is basically determined by three parameters: i) its light absorption property; ii) the rate of reduction and oxidation of reaction substrate by electrons and holes, respectively and iii) the rate (or probability) of electron – hole recombination. [25] All these parameters are determined by intrinsic physical and chemical properties of the solid which will be discussed below without being exhaustive.

TiO_2 has several allotropic forms, among which the most common forms are the tetragonal anatase and rutile and the orthorhombic brookite (*Figure 2*). Rutile is the thermodynamically most stable form of TiO_2 while anatase and brookite readily transform into rutile when heated [26] the basic building units of these TiO_2 polymorphs are the TiO_6 octahedra, where the titanium (Ti^{4+}) atoms are co-ordinated with six oxygen atoms (O_2^-). The difference between the polymorphs is basically the arrangement and the distortion of the TiO_6 building blocks in their structures. Therefore anatase can be described as tetragonal crystal, built of edge-sharing octahedra forming (0 0 1) planes; brookite and rutile exhibit both corner- and edge-sharing octahedra configurations. The differences in lattice structure cause different mass densities which basically results in alterations between electronic and optical properties of the polymorphs. By definition, the band structure is characterised as series of energetically closed spaced energy levels: the valance band is associated with covalent bonding between atoms that compose the crystallite and the conduction band is associated with a second series of spatially diffuse, energetically similar levels, lying at higher energy levels in the macromolecular crystallite. [23]

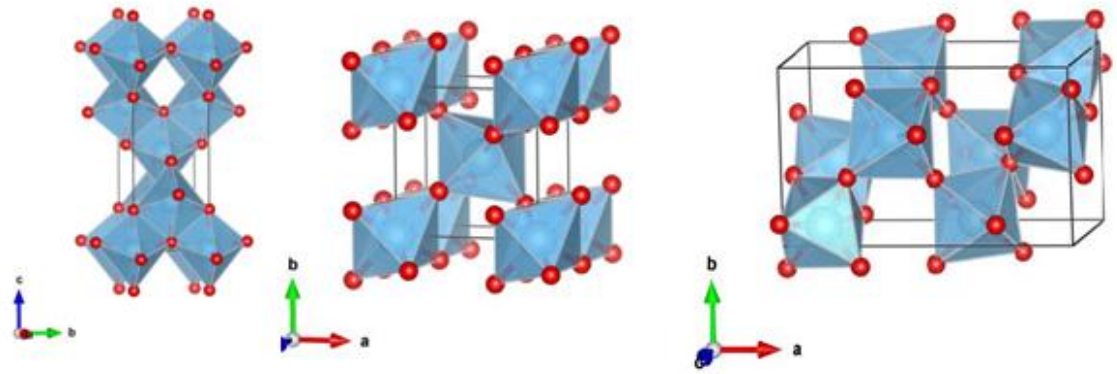

Figure 2 Crystal structure of *a)* anatase *b)* brookite and *c)* rutile illustrated by VESTA visualisation program [27]

Among the three polymorphs anatase and rutile are the more investigated, more often than brookite for photocatalytic studies. The reason for that might be that it is fairly difficult to synthesise pure brookite without the presence of the other two polymorphs. [26] Despite of anatase has a larger band gap than rutile, therefore it might seem less useful when one considers to use it under solar light irradiation, most often it is reported to be the most active form of TiO_2. [28, 29] This latter has multiple reasons. It is reported to have a higher capacity to adsorb O_2 which process goes on with the generation of O_2^- and O^- which are highly reactive species. [30] It has also been reported that the recombination rate is relatively lower on anatase than on rutile. [30] This latter is closely related to the finding of M. Batzill *et al*, where they found that that the bulk transportation of charge carriers in anatase was higher which obviously

means lower rate of recombination. [31] J. Zhang et al showed using first-principle density calculation theory that the lifetime of charge carrier is longer in anatase as it seems to be an indirect semiconductor and the direct transition from the CB to the VB is impossible. They also suggested that the lightest effective mass of produced electrons and holes is representative of anatase and it contributes to retarded recombination in the bulk and higher probability that the charge carrier reaches the surface of the NP before recombination would occur. [32] Nevertheless, it seems that better photocatalytic efficiencies can be obtained polycrystalline samples due to the better electron transport between different phases. [33, 34]

For catalyst materials, it is generally accepted that high surface area is an advantage in terms of a higher concentration of active sites per square metre leading to higher reactivity. Certainly, the surface area is closely related to the NP size i.e., the smaller the particle size, the higher the surface area is. The issue of particle size is so critical, that under a certain size it influences the size of the band gap. This phenomenon is the so-called *quantum size effect*, which is representative of NPs in the size range of 10-100 Å, where the size of NPs become comparable to the de Broglie wavelength of the charge carriers in the semiconductor. As a result of confinement, the electron and hole do not experience a delocalisation in the bulk and a quantisation of discrete electronic states is produced, therefore the effective band gap of the semiconductor increases resulting in changed optical, electronic and catalytic properties. [23] The degree of crystallinity is inversely proportional to the surface area of the catalyst and since these two properties are very difficult to achieve simultaneously, the synthesis conditions have to be carefully planned. Furthermore, pore size and pore volume are also some of those physical parameters which can significantly influence heterogeneous catalytic reactions.[25, 35] Furthermore, particle morphology and exposed crystalline phases also significantly influence the photocatalytic activity. It has been found that polyhedral shaped TiO_2 had superior photocatalytic activity to degrade phenol and methanol compared to spherical NPs with otherwise similar structural characteristics. [36, 37] It has been reported that exposed facets dramatically influence the reaction mechanism and selectivity. [38, 39] For example, it has been shown by *ab initio* density functional theory (DFT) calculations that generation of superoxide radical is facilitated over anatase (1 0 1) exposed facet from molecular oxygen. [40] Not only the exposed facets, but the overall morphology of primary NPs may influence the photocatalytic activity. Many indications can be found in the literature that 1D (elongated) morphology of NPs may result in better efficiency because the electron transport is facilitated along the longitudinal dimension of the nanocrystal which results in retarded electron-hole recombination and increased reaction rates. [40] Besides structural properties and morphology, surface chemistry has to be also acknowledged as a determinant parameter in control of aggregation state, O_2

consumption properties and adsorption/complexation of the target compounds, significantly influencing the activity of the photocatalyst among the studied reaction conditions. [41, 42]

2.3. Photocatalyst supports, nanocomposite materials

For heterogeneous catalytic reactions, it is very common that supports are added to the catalyst to contribute to the catalytic process which will be discussed in this chapter. Depending on their chemical nature they can be classified as organic or inorganic supports.[43] Generally, supports are nano- or micron-sized particles, which carry the reactive NPs anchored to them. These nano- or sometimes micron-sized assemblies of nanoparticles are often referred as nanocomposites in the field of material science and nano-engineering. The supports either simply immobilise the catalyst, providing good stability and resistance against mechanical impacts, limit sintering or aggregation of the reactive NPs and/or they can actively contribute to the chemical stability of the catalyst and govern its useful lifetime.[43] The support may also contribute to the catalytic process with its high surface area and good adsorption properties. This phenomenon is known as the "Adsorb & Shuttle" (A&S) effect, i.e. the adsorption of molecules on the inert, adsorptive, domains, followed by diffusion to the photocatalytic domains. [44] Historically, active carbon (AC) was the first to be used as an adsorbent to demonstrate the concept of A&S and up to now it is commonly used. Besides AC, [45, 46] zeolites [47, 48] metal oxides such as silica, [49] alumina, [49] glass fibres, pumice stones and polymers, [50] furthermore, layered silicates showed preferential adsorption towards organic pollutants. [50, 52] These materials therefore have double functions: anchoring the catalyst NPs and perform adsorption functions towards organic compounds. Therefore, they have been used to prepare versatile nanocomposite materials with semiconductor NPs for photocatalytic purposes. [53, 54, 55, 56, 57, 58, 59 60]

In heterogeneous (thermal) catalytic reactions metal oxides, including TiO_2, are often used compounds to support catalytic reactions on noble metal. It has been shown that the support influences the activity of the catalyst by influencing its electronic properties. This is attributed to the direct electronic interactions between small metal NP and reducible oxide support, which is called *strong metal-support interaction* (SMSI). [61] A good example is the catalytic hydrogenation of CO on Rh catalyst or better known as the Fischer-Tropsch synthesis. [62] TiO_2 not only immobilise Rh, but more importantly, it promotes the dissociation of the chemisorbed CO through enhanced partial electron transfer from TiO_2 to Rh. This process accelerates the donation of electrons from Rh into an antibonding π-orbital of the CO, thereby strengthening the Rh-C bond and weakening the CO-bond. [63] This phenomenon is referred as “carrier-effect” in the literature and well known for catalytic reactions of metal oxide supported metal NPs. [64,65 66] Graphene oxide (GO) and reduced graphene oxide (rGO) are recently gaining prominent attention as supporting materials, especially graphene, owing to its

extended sp^2-bonded carbon network and excellent conductivity. [67] The unique 2D structures of GO and rGO possess extremely high specific surface area which makes them excellent supporting materials. GO has as large as 1700 m^2/g geometrical specific surface area as it has been revealed earlier in our department as well .[68] These materials have been reported to improve the photocatalytic activity of TiO_2 because they acts as an electron acceptor and a photosensitizer. [69] It is especially true for rGO, because it shows exceptionally high conductivity owing to the existence of an extended sp^2-bonded carbon network therefore individual sheets of graphene possess excellent conductivity and it has been reported to efficiently promote electron-hole separation in irradiated GO-TiO_2 [69] or rGO-TiO_2. [70,71,72] Polymers can also be used as binding materials to support TiO_2 and to obtain nanocomposite films. However, due to their limited resistance towards UV-induced degenerative processes we have to take their limited stability into account when applying them as photocatalyst supports. As most polymers tend to photodegrade under UV-irradiation, even without the presence of photocatalyst, it may cause problems with its long term stability. [73]

2.4. Separation of the solid phase photocatalyst from the reaction medium

In recent R&D processes for water treatment, photocatalytic reactors can generally be classified as i) slurry phase reactors and ii) fixed-bed reactors. [15] Slurry phase reactors have the huge advantage over fixed-bed reactors, i.e., the contact area between pollutants and NPs is much larger which facilitates a higher rate of degradation. However, separation of the photocatalyst is undoubtedly a serious issue once the photocatalytic run is over. The question is raised not only for economic, but environmental reasons as well, therefore the question of catalyst separation cannot be neglected. Practically, the longer the photocatalyst can be used, the lower the cleaning costs are. For that reason, easily recoverable, stable catalyst are desired for real applications. So far the recovery of nanoparticulate photocatalysts is neither fast, nor cheap. [74-75] Being these photocatalytic substances submicron sized colloids most often with electric surface charge, the phenomenon of colloid stability often makes these endeavours even more tedious. Metal oxides, including TiO_2, show pH dependent surface charge stemming from the protonation and deprotonation of surface OH-groups on low and on high pH values, respectively. Moreover, all metal oxides can be characterised with a point of zero charge (p.z.c.) on the pH scale, where the net surface charge is close to zero, therefore the repulsive forces between the particles are minimised and the colloid stability of the suspension is highly limited and the aggregation of NPs are facilitated. As a result of that the hydrodynamic diameter of TiO_2 NPs and the settling rate is the highest on this pH value (~7 for TiO_2), the separation of the catalyst is slightly more promoted. [76] Some progress have been made to separate the solid phase photocatalyst by addition of different supports. For example the previously mentioned clay mineral/TiO_2

nanocomposites are not only beneficial for environmental remediation due to their high adsorption capacity towards pollutants, but also owing to their accelerated sedimentation in aqueous phase. Photocatalysts, functionalised with magnetic NPs can be also. [54, 55, 57, 77, 78 79, 80]

Fixed bed reactors offer practical solution to separate the photocatalyst from the polluted medium, because the NPs are attached to a support and there is no need for posterior separation. Due to lower exposed surface area, however, the immobilised NPs lost a great potential of their photocatalytic activity. Despite of that, this arrangement is often desired because it is very easy to maintain. Moreover, fixed bed photoreactors can be applied for both, water and air cleaning.

2.5. Vis-light responsive and plasmon-enhanced photocatalysts

Probably, the major motivation of scientists, working on the field of photocatalysis using TiO_2, is to enhance its photocatalytic activity preferably under solar light irradiation. As it is known, natural sunlight contains only ca. 5 % of UV rays at sea level that is not very sufficient to induce significant photochemical reactions on wide band gap semiconductors. Excellent reviews are available which summarise the currently known methods to induce Vis light activity of TiO_2-based photocatalysts [81, 82]. Doping, i.e. introduction of metal impurities such as iron, made by sol-gel and flame hydrolysis methods, [83, 84] vanadium [85] and non-metal elements, such as nitrogen [86, 87, 88, 89, 90, 91, 92], carbon, [89, 93, 94] sulphur [94, 95] and fluorine [96, 97] into the TiO_2 lattice, is a widely investigated approach to narrow the band gap of the material by modulating the band positions or by introducing mid-gap states.
There are numerous promising results in this area, however, in some cases, especially for metal doping, it turned out that the procedure actually decrease the photocatalytic efficiency due to the formation of recombination centres. Introduction of colour centres by creating defect sites can also lead to Vis light activity of the photocatalyst. [98] Dye sensitisation has also been reported to be a successful method to extend the Vis light response of TiO_2. [99] Furthermore, the previously discussed TiO_2-GO and TiO_2-rGO needs to be credited here again for their Vis light due to the presence of carbonate structural fragments bonded with titanium. [100]

Recently, plasmon-enhanced nanomaterials have attained considerable attention due to their high activity for photovoltaic and photocatalytic applications. [101, 102, 103, 104, 105] In general, plasmonics is related to the localisation, guiding and manipulation of electromagnetic waves beyond the diffraction limit and down to the nanometre-length scale. [106] In metal/semiconductor nanocomposites the advantageous properties of plasmonic noble metal and semiconductor NPs are merged. Several excellent reviews are available in the literature discussing the topic. [106, 107] The term, plasmonics, is basically related to the localisation, guiding and manipulation of electromagnetic waves. This phenomenon is observable in metal NPs when they are irradiated by light with a wavelength much

larger than their dimensions. [106] The term "plasmonic photocatalysis" was introduced by K. Awazu et al. in 2008. [108] Generally speaking, processes that feature a collective oscillation of electrons in the solid when light is shined on them and the oscillation of the electrons is in resonance with the incident light can be nominated as plasmonic [109] (*Figure 3*). Thus, these nanostructures can be utilised to concentrate and guide light on a nanometre scale. [110] This property can further be utilised to enhance photocatalytic processes as these nanostructures can readily concentrate the energy of light into the close vicinity of photocatalyst NPs. Thus the shape and location of optical absorbance band will be highly dependent on the size, shape aggregation state of the material and dielectric constant of the material and the environment, thus it can be well controlled by changing these parameters. [111 112, 113 114 115 116, 113 117, 118, 119] The advantageous fact that noble metal/semiconductor heterostructures when used in photocatalytic and photoelectrochemical applications, they require only a very small amount of noble metal to provide good efficiency. As a matter of fact, too high amount of metal content deposited on the TiO_2 can significantly inhibit the photocatalytic process as the metal nanoclusters will attract the electrons too strongly and as a result of that the electrons will be trapped. Several metals are known to support plasmon modes in the Vis and near IR range, e.g. Au, Cu, Li or Al, but above all them Ag is probably the most interesting. Not only that its surface plasmon modes can be tuned in the range from 300 to 1200 nm and it is considerably cheaper than gold (which is the other most often used material for plasmonic applications), but it has the highest quality factor (Q) from all of them which is directly proportional of the strength of surface plasmon. [106]

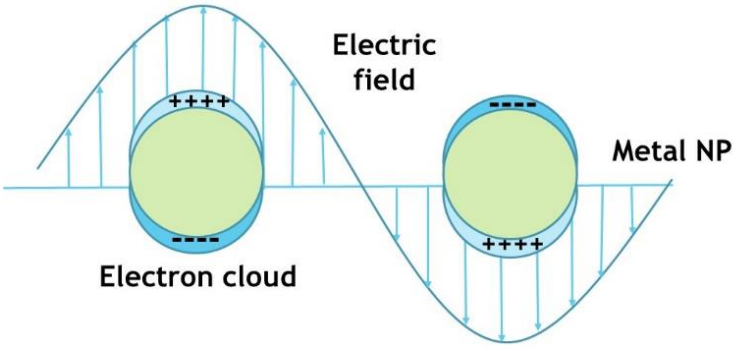

Figure 3 Depiction of localised surface plasmons of noble metal NPs

Another prominent feature besides the plasmon enhanced properties of noble metal/semiconductor heterostructures, considered from a prospective of solid state physics, is the Schottky-barrier which is technically the metal/support interface where the charge carrier transfer takes place between the two components owing to the differences in the work functions between metal and

semiconductor which induces a continuous flow of electrons. Kamat et al. showed the shift of Fermi-level in TiO_2 towards the CB and corollary enhancement of charge carrier transfer towards the metal NP.[120, 121] Zhang et al. attributed forced e^-/h^+ pair separation and fast-lane charge transfer to the presence of metal-semiconductor junction and Vis light response, enhanced UV-Vis absorption, reduced e^-/h^+ diffusion length, enhanced local electric field, LSPR-powered e^-/h^+ generation, local heat effect and molecule polarisation effect. [107] The combined effect of these all contribute to significantly higher rates of photocatalytic activity under UV and UV-Vis light than that on pure TiO_2. [122, 123]

2.6. Photocatalysis in application, commercially available photocatalytic products

Photocatalytic applications using TiO_2 have already been taken to the stage of commercialisation and the slowly but steadily growing availability of products on the market indicates the worldwide recognition of this group of materials. Products with photocatalytic activity are gaining emerging popularity, primarily in Asian countries, such as Japan or South Korea and China, but photocatalytic products tend to show up more and more in the area of European Union and United States also. The most popular photocatalytic products are self- cleaning coatings or external building elements to prevent build-up of dirt on, such as photocatalytically active cement from Taiheiyo Cement Corp., Japan [124] self-cleaning windows (*Pilkinton Active*™*),* based on the super-hydrophilic property of TiO_2. Today's people spend the most amount of their time indoor, either in their offices or other workplaces, schools or in their homes, therefore the quality of indoor air can undoubtedly affect our well-being. Unfortunately, "Sick Building Syndrome" (SBS) is a well-known phenomenon among urban population. It is known that irrespectively of regular ventilation of the rooms, concentration of volatile organic compounds (VOCs) can be very high which are originated from building materials, furniture, cleaning agents and from cooking gas. High concentrations of VOCs can cause several adverse health effects such as asthma, dizziness, respiratory and lung diseases, and they might higher the risk to develop cancerous diseases. [125] In addition to VOCs, particulate pollutants, airborne bacteria, viruses, mould and other pathogens, are also present and can be highly concentrated in our indoor spaces. These latter has particular relevance in hospitals and other public premises. It has to be considered that there are several cases when casual ventilation (as simple as opening the window) cannot be executed, because either the outdoor air is even more polluted or the building is constructed in a way that it is ventilated by its special built-in ventilation system. In these cases, it is particularly important to obtain good quality indoor air relying on alternative solutions. Nowadays, a variety of indoor air purification devices can be found in the market to fight off the above mentioned problems. Most of them rely on physical separation of particulate pollutants and bacteria by circulating the air through their filtration system. In most cases the so-called high-efficiency particulate arrestance

(HEPA) filters are used which remove 99.999% of particles ≤ 0.3 µm size. These filters may contain silver to kill germs and microbes (*Alen Breathsmart HEPA Air Purifier for Asthma and Mold*, Alen, USA). Recently designed air purifiers also include germicidal UVC-lamps for its sterilising effect. In addition to the built-in UV lamps, some brands (*Air Oasis 5000*; Air Oasis, USA) can also be found incorporating photocatalysts to enhance the antibacterial effect of UV-irradiation and trigger decomposition processes of organic pollutants such as VOCs. Depending on the needs of the consumers, air purifiers are sold for household and commercial use with different air cleaning capacities (10-100 cubic feet per minute, CFM). However, I found that manufacturers rarely publish any detailed information about their products, especially, concerning their performance, which makes it fairly challenging to compare their efficiency.

3. Objective and scope of dissertation

This work aims to contribute to the research field of water cleaning and air purification technologies by means of heterogeneous photocatalysis using TiO_2. Although, photocatalysis has shown a great potential as a low-cost, environmental friendly and sustainable technology for purification of water and air using this material, there are still momentous technical challenges to overcome. The most urging problems are probably the low quantum efficiency – especially under solar irradiation – and the problem of catalyst separation after the photocatalytic cycle. This work focuses on these issues and the core structure of this document is shown below in *Figure 4*.

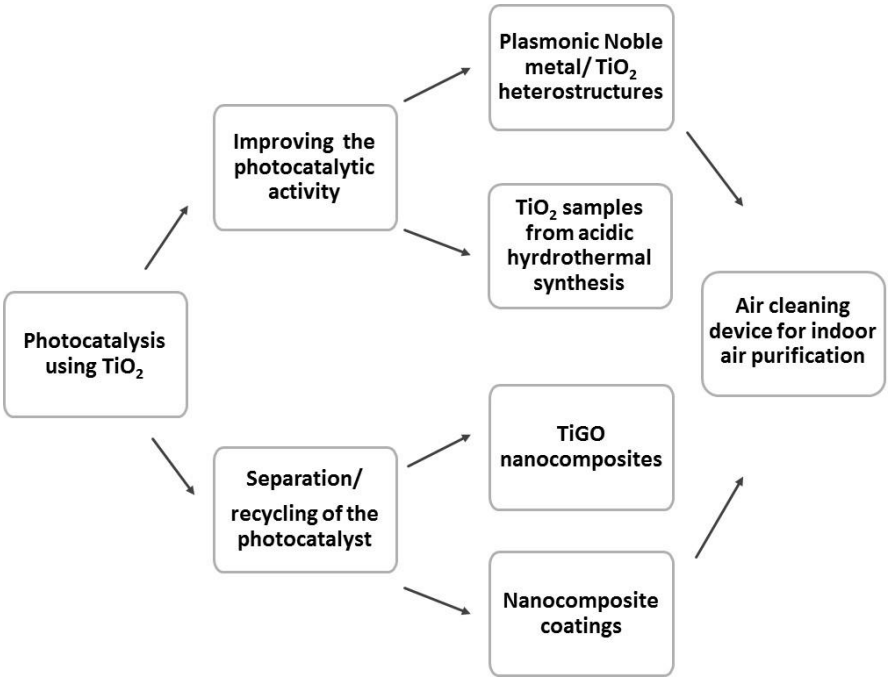

Figure 4 Scope of thesis

4. Experimental

4.1. Materials and methods

4.1.1. Materials

Aeroxide P25 (Evonik Degussa GmbH) TiO_2 was used to prepare noble metal modified titania heterostructures, TiGO nanocomposites and it was used for the synthesis of sodium titanate NSs. Sodium hydroxide (NaOH) pellets, hydrogen chloride (37 wt% HCl) and nitric acid (65 wt% HNO_3) were purchased from Reanal or from Sigma Aldrich. Gold(III) chloride tryhidrate ($HAuCl_4 \cdot 3\ H_2O$, puriss, $m_{wt}\% \geq 49$) and silver nitrate ($AgNO_3$, puriss) were purchased from Sigma-Aldrich for the preparation of noble metal NPs. 2-propanol (puriss, as an electron donor to assist the reduction of noble metal ions, was received from Molar, Hungary. Poly-acrylate [poly-(ethyl acrylate-co-methyl methacrylate; p(EA-co-MMA)] was obtained from PannonColor Kft. and it was used without any purification. For all the synthesis and preparation work d.i. water was used.

4.1.2. Preparation of hydrogen titanate nanofibres (H-TNFs) and their consecutive transformation intoTiO_2 NPs by hydrothermal post treatment (HPT)

First, sodium titanate nanofibres (Na-TNFs) were obtained by high alkali hydrothermal treatment of TiO_2. Typically, 3.84 g P25 TiO_2 was dispersed in 80 ml 10 mol/L aqueous NaOH solution in a Teflon-lined autoclave, and the mixture was hydrothermally treated at 180 °C for 48 hrs. In order to obtain H-TNFs, the hydrothermal product was washed with 3 L of ultrapure water then stirred in 1 L of 0.5 mol/L HCl overnight (~0.05- 0.055 mol HCl/g TNF). The sample was washed again with 1 L ultrapure water then dried at 60 °C.

Titania NSs were prepared by acidic hydrothermal treatment as follows: 1.0 g of the as-prepared H-TNFs was hydrothermally treated at 120 °C for 24 hrs in 80 mL 0.05 – 4 mol/L HNO_3 solution to obtain samples HPT0.05; HPT0.1; HPT0.5; HPT1; HPT2 and HPT4. The samples were centrifuged and washed with ca. 0.5-0.8 L water, until pH~5, then dried at 60 °C. The samples were ground in mortar and kept in closed glass vessels until use.

4.1.3. Preparation of noble metal modified TiO_2 photocatalysts

5 g TiO_2 was dispersed in 0.5 L d.i. water then $1.48 \cdot 10^{-2}$ L $1 \cdot 10^{-2}$ mol/L $AgNO_3$ or $6.37 \cdot 10^{-3}$ L $1 \cdot 10^{-2}$ mol/L $HAuCl_4 \cdot 3H_2O$ was added to prepared Ag- and Au- modified TiO_2 ($wt_{metal}\% = 0.5$) samples. The pH of the suspension was adjusted to 7.2 then 0.1 mol/L $NaBH_4$, as reducing agent, was added to the suspensions: $7.39 \cdot 10^{-3}$ L and $3.19 \cdot 10^{-3}$ L for Ag-TiO_2 and for Au-TiO_2, respectively. The suspensions were stirred for 60 min, washed with d.i. water, centrifuged and dried.

Silver (I) oxide (Ag_2O) was prepared as follows: 30 ml 0.1 mol/L $AgNO_3$ was added dropwise to 0.06 L 2 mol/L NaOH solution. After 5 min of stirring, the suspension was filtered, washed, and dried at 60 °C in air. Silver (II) oxide (AgO) was prepared by heating up 0.15 L 0.34 mol/L NaOH to 85 °C then 25 ml $K_2S_2O_8$ was added to the hot alkali solution. Finally, 0.025 L 0.34 mol/L $AgNO_3$ was added to the solution dropwise. The temperature of the mixture was raised to 90 °C then it was mixed further for 15 min. The precipitate was filtered through a Büchner funnel, and the sulphate ion was heartily washed with doubly distilled water. The product was dried in air at 60 °C.

Further Ag-containing samples were prepared using these obtained silver oxide samples. Ag_2O-TiO_2 and AgO-TiO_2 were obtained by adding required amount of these oxides to aqueous suspensions of TiO_2 (c = 1 wt/V%; V= 0.2 L). The suspensions were filtered then dried at 60 °C.

Ag_2O-TiO_2 sample was also prepared using commercially available Ag_2O, purchased from Sigma Aldrich (≥99.9 %). The sample was entitled as Ag_2O-TiO_2 (Sigma)

4.1.4. Preparation of TiO_2 – Graphite oxide (TiGO) nanocomposites

Graphite oxide (GO) and the TiGO nanocomposites were previously prepared in our department by a self-assembly method. Graphite oxide was synthesised from natural flaky graphite (Graphitwerk Kropfmühl AG, Germany) by the Brodie method. The graphite was highly oxidised ($C_2O_{0.98}H_{0.40}$) and it is identical with that codenamed "GO-2" used in earlier publication. **[126]** To prepare TiGO composites with GO content of 1 to 10 wt%, first 40-400 mg of GO was dispersed in 1.6 L of water. In each case, the pH was adjusted to 8.5 ± 0.3. After 15 minutes of sonication and one day of continuous stirring in the dark the pH was reset to 8.5 ± 0.3. Next, these suspensions were poured into 0.4 L of 9-9.9 g/L aqueous colloid dispersions of TiO_2 (pH = 5) upon which the oppositely charged colloids rapidly coagulated. After decantation the wet sediments were dried at 50 °C then ground. The prepared nanocomposites are denoted hereafter as TiGO-1; TiGO-2; TiGO-5 and TiGO-10 referring 1; 2; 5 and 10 wt% of GO content, respectively.

4.1.5. Preparation of nanocomposite films

Nanocomposite films, containing TiO_2 or noble metal modified TiO_2 and organic or inorganic supports, were prepared by spray coating. This is a feasible method to obtain thick films with homogenous consistency and also with good reproducibility of the thickness. 10 – 30 m/V% suspension of the mixture of selected photocatalyst and organic or inorganic support was sprayed on 45 cm^2 glass slides from a distance of 20-30 cm in several steps and briskly dried. It was repeated until 1.25 mg/cm^2 dry material built up on the slides.

Nanocomposite films were prepared using TiO_2 as photocatalyst and inorganic supports, namely, zirconium oxide (Riedel-de Haen, purum) and sodium hectorite (Hect) ($Na_{0.3}(Mg,Li)_3Si_4O_{10}(OH)_2$, Fa-Laponite, Solvay). The photocatalyst content of the films was 20 wt%; 40 wt%; 60 wt%; 80 wt% and 100 wt% and the relative amount of supporting materials (ZrO_2: Hect) was kept constant (9:1).

Nanocomposite films were prepared using TiO_2, Ag-TiO_2 as photocatalyst and [poly(ethyl acrylate-co-methyl methacrylate; p(EA-co-MMA)] as organic support. The polymer layer was loaded with 13-15 wt% photocatalyst. The average thickness of films was 100 ± 20 μm. The films were irradiated by a low-pressure mercury lamp (GCL307T5VH/HO type, LightTech, Hungary, P =35 W) from a distance of 5 cm for 0, 1, 4, 24, and 48 hrs. The emission spectrum of the light source is presented under *Appendix 1*.

4.2. Characterisation techniques

4.2.1. UV-Vis diffuse reflectance spectrophotometry (UV-DR)

UV-Vis diffuse reflectance spectra of the powder samples were recorded by a NanoCalc 2000 Micropack spectrometer equipped with an integrated sphere and HPX 2000 Micropack high power Xenon lamp.

The band gap energy (E_g) values were obtained from the UV-Vis diffuse reflectance spectra. The absorption coefficients (α_{KM}) were calculated from the reflectance spectra using the Kubelka-Munk function (Eq. 6), where α_{KM} stands for the absorption coefficient and R_∞ is the reflectance of an infinitely thick sample with respect to a reference at each wavelength [127]

$$\alpha_{KM} = \frac{(1 - R_\infty)^2}{2R_\infty}$$

Eq. 6

To determine the band gap energies, *Tauc plot* ($\alpha_{KM}\, h\nu$ *vs.* $h\nu$) correlation was used.

4.2.2. Attenuated Total Reflection Fourier-Transformation Infrared (ATR-FTIR) Spectroscopy

A Biorad FTS-60A FTIR spectrometer was used to analyse the chemical composition of photocatalyst/polymer nanocomposite films before and after photo-aging. The spectra were recorded in the wavelength range of 4,000–400 cm^{-1}. For each measurement 256 scans were collected with a resolution of 4 cm^{-1}.

4.2.3. Raman spectroscopy

A Biorad FTS-60A Fourier Transformation Infrared (FTIR) spectrometer equipped with Attenuated Total Reflection crystal detector was used to record the spectra of the nanocomposite films. The scans were recorded in the range of 4000–400 cm^{-1} at a resolution of 4 cm^{-1}.

4.2.4. X-ray diffraction (XRD)

X-ray diffraction measurements for TiO_2 samples were carried out on Bruker D8 diffractometer (Bruker-AXS GmbH, Karlsruhe, Germany) equipped with a, 2.5 degree soller slits, 0.5 degrees divergence slit, an air scattering screen and a gas-filled position sensitive detector. As a radiation source, Cu-Kα radiation ($\lambda = 0.1542$ nm) was used. Rietveld refinements of the TiO_2 samples prepared by HPT of H-TNFs. were performed with Topas v4.2 (Bruker-AXS-GmbH, Karlsruhe, Germany) using the fundamental parameter approach (Cheary, Coelho, & Cline, 2004). The background was fitted with a Chebychev polynomial of order 15. Zero-shift, lattice parameters, an over isothermal parameter, scale factors and Lorentz crystallite size broadening were refined. The crystallite size was determined based on the volume weighted integral peak width.

4.2.5. Nitrogen sorption measurements

To characterise the surface properties of TiO_2 samples, prepared by HPT of HNFs, N_2 sorption measurements were carried out at 77 K using a Micromeritics ASAP2420 type instrument. Prior to measurements, the samples were degassed at 200 °C for 24 hrs. For the noble metal modified TiO_2 samples and TiGO nanocomposites, the measurements were carried out on a Micrometrics Gemini 2375 type instrument. The Brunauer- Emmett-Teller (BET) method was used to determine the specific surface area of the samples and Barrett-Joyner-Halenda (BJH) method to determine the pore size distribution.

4.2.6. Transmission Electron Microscopy (TEM)

TEM images were recorded by a Phillips CM 100 microscope at University of Szeged in Hungary or by a TECNAI TF20 SuperTwin microscope in ICES, Singapore, using 200 eV accelerating voltage.

4.2.7. Scanning Electron Microscopy (SEM)

SEM images were taken on a Hitachi S-4700 SEM device at 10 kV accelerating voltage.

4.2.8. X-ray Photoelectron Spectroscopy (XPS)

X-ray photoelectron spectra (XPS) of $Ag_x(O)$-TiO_2 and TiGO-2 nanocomposite were recorded with a SPECS instrument equipped with a PHOIBOS 150 MCD 9 hemispherical electron energy

analyzer operating in the FAT mode. The excitation source was the Kα radiation of a magnesium anode (hν = 1253.6 eV). The X-ray gun was operated at 220 V power (14 kV, 15 mA). The pass energy was set to 20 eV, the step size was 25 meV, and the collection time in one channel was 100 ms. Typically five scans were added to get a single spectrum. The C 1s binding energy of adventitious carbon was used as energy reference; it was taken at 285.1 eV. For data acquisition, both manufacturer's (SpecsLab2) and commercial (CasaXPS, Origin) software were used.

4.2.9. Contact angle (CA) measurements

Advancing and receding CAs were measured by EasyDrop (Krüss GmbH, Hamburg, Germany) drop shape analysis system equipped with an Peltier temperature chamber and a syringe steel needle of 0.5-mm diameter, under atmospheric pressure. The measurement method, used for the analysis was the tilting plate method at 30° tilt angle. With the use of a syringe, a sessile drop of water was formed at the tilted plate. The drop shape was recorded by a CCD camera of the goniometer with frequency of a 2.77 frames/s. To determine the CA, the drop contour was mathematically described by the Young–Laplace equation using DSA100 software, and the CA was determined as the slope of the contour line at the three-phase contact point. Water used in this experiment was purified by Q-Millipore system.

4.2.10. Photocatalytic experiments

The photocatalytic activity of TiGO nanocomposites was tested in liquid phase. 375 mg nanocomposite powder was dispersed in 375 mL 1mmol/L phenol solution (1 g/L catalyst loading) in a double-walled immersion well photochemical reactor. The suspension was irradiated under continuous stirring from inside of the reactor by a Heraeus TQ 150 type high pressure mercury lamp (P = 150 W, λ = 240-580 nm) The emission spectrum of the light source is presented under *Appendix 1*. The high energy photons (λ < 320 nm) were filtered by a Pyrex tube in which the light source was placed. The cooling jacket of the reactor kept the temperature of the suspension at ~25 °C. 1 mL amount of samples were taken in 5-10 min frequency then centrifuged and filtered before measuring the phenol content by HPLC. The equipment was build up by Knauer injector, degasser and pump, an RPC18 column (LiChroCART125-4, Merck) and a Knauer WellChrom K-2600 UV-VIS detector. A mixture of 35 vol% methanol and 65 vol% water was used as eluent. To study the reusability of the composites, TiGO-2 was irradiated in four consecutive runs. After each recovery, the solid was washed with deionised water and centrifuged before re-suspending it in the test solution. The catalyst concentration in the system was kept constant by adjusting the volume of phenol solution to the amount of remained catalyst.

Photocatalytic activity of the samples were tested by following photocatalytic oxidation of ethanol EtOH vapour in a flat photoreactor (ca. 0.165 L) at 25 °C ± 2 °C. Low pressure Mercury lamps were used for the flat film reactions. The photodegradation tests for Ag_xO-modified TiO_2 samples and for organic and inorganic supported TiO2 nanocomposite films were conducted under UV-Vis emitting GCL303T5/# type 2 (Light-Tech, Hungary; P= 15 W, λ =254- 612 nm) light source; while for HPT TiO_2 samples tests were conducted under UV-rich GCL303T5/# type 1 (254-435 nm). The emission spectra of the light sources are presented in *Appendix 1* for comparison. The photocatalytic runs were carried out after 30 min adsorption equilibration time of EtOH with initial concentration of 2.73 ± 0.018 mg/L. The chemical composition of the vapour phase was analysed by a Shimadzu GC-14 type gas chromatograph equipped with a thermal conductivity detector and a flame ionisation detector (FID). The flow rate of the gas mixture in the photoreactor system was kept at 0.375 L/min. The reaction rates (*k*) for the photocatalytic degradation of phenol in aqueous phase and for ethanol vapour were determined according to Eq.7

$$-ln\frac{c}{c_0} = kt$$

Eq. 7

, where c_0 is the initial concentration of model pollutant and c is the concentration at t irradiation time.

5. Results and discussion

5.1. TiO_2 – GO nanocomposites

5.1.1. Optical, structural and electrical characterisation of TiO_2 – GO nanocomposites

GO is a non-stoichiometric compound with and empirical formula of C_4O_2H for well oxidised samples.[126] Depending on the state of oxidation, it possesses different amount of O and H constitute functional groups such as cyclic ethers, –OH and –COOH groups which are covalently attached to the carbon skeleton and non-oxidised aromatic regions or isolated C=C double bonds may also feature the chemical structure. [126] Owing to the surface functional groups it is highly hydrophilic therefore a stable colloidal dispersion can be obtained once it is delaminated into single lamellae among highly basic conditions.

It is known that in highly alkali medium GO sheets spontaneously exfoliate due to the progressive deprotonation of acidic functional groups and the evolution of highly negative surface

charge of the GO planes.[68] As a result, this material can be well applied as a support for metal oxide photocatalysts with a high specific surface area (1700 m^2/g). [68] TiGO nanocomposites, prepared by heterocoagulation of positively charged TiO_2 NPs and negatively charged GO sheets, were probed as photocatalyst nanocomposites.

Addition of GO (≤ 10 wt%) to TiO_2 significantly increased absorbance of the catalyst in the Vis-range *Figure 5*. The calculated E_g values are summarised in *Table 1*. According to Shen et al, the band gap of GO can be tuned between 2 to 0.02 eV depending on the state of oxidation. [128] As a result of heterocoagulation, and nanocomposite formation, the band gap energies of pure TiO_2 decreased due to the presence of GO which could be coupled with induced Vis-light activity as well.

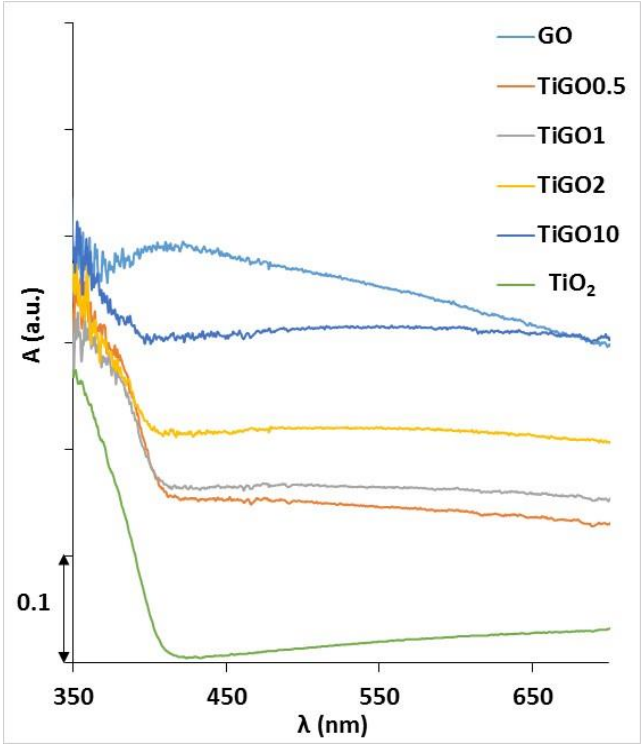

Figure 5 Diffuse reflectance spectra of TiGO nanocomposites, GO and reference TiO_2

Table 1 Calculated band gap energies and corresponding wavelengths

Nr	Sample ID	E_g (eV)	λ (nm) [a]
1	TiO_2	3.10	400.00
2	TiGO-0.5	2.80	442.85
3	TiGO-1	2.80	442.85
4	TiGO-2	2.65	469.92
5	TiGO-10	2.22	558.56

[a] $\lambda = 1240/E_g$

FTIR spectra of pure GO, TiO_2 and selected nanocomposites are shown in *Figure 6*. Typical vibrations of TiO_2 correspond to the broad band between 400-800 cm^{-1} detected in pure TiO_2 and TiGO nanocomposites. It is reported that the development of Ti-O-C vibration at 798 cm^{-1} represents the chemical bonding between TiO_2 and GO [129, 130] which was absent from our TiGO samples. There is a broadening, however, for double oxidised GO, which was rich in surface functional groups: Characteristic bands at 810 and 940 cm^{-1} refer to C-H bonds in the aromatic carbon rings of GO backbone with sp^2 hybridisation; a sharp band at 1047 cm^{-1} assigns C-O (alkoxy) vibrations; a wide band at 1340 cm^{-1}. These bands are also represented TiGO-10 sample as well. Furthermore, a very broad band between 2400-2900 cm^{-1} is assigned to the C-H vibrations with sp^3 hybridisation for pure GO. The sharp peak at 1615 cm^{-1} represents the presence of surface adsorbed water which can be observed for all samples. For GO and TiGO nanocomposites, this band is probably overlapping with the skeletal C=C vibrations which is normally represented in this region. [131] A smaller band at 1705 cm^{-1} refers to the C=O stretching vibration of carboxyl groups. It is shown that GO is rich in O-H functional groups, indicated by the broad band between 2900 – 3600 cm^{-1}, which are mostly responsible for the changeable acidic character of GO. Vibrations of surface O-H groups were also observed for pure TiO_2, obviously, and for TiGO nanocomposites as well.

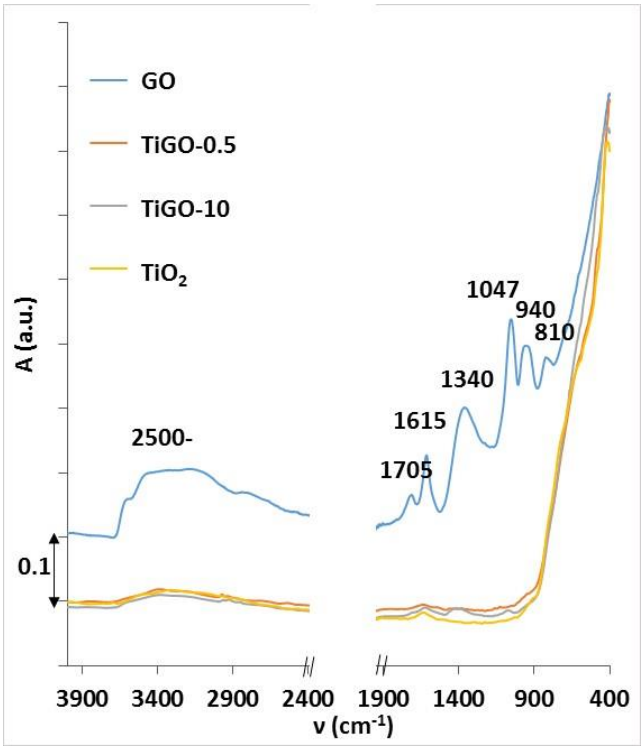

Figure 6 Normalised FTIR spectra of GO, TiO_2 and selected TiGO nanocomposites

The TEM images in *Figure 7* are representing TiGO-10 with 10 wt% of GO content. It was established from the TEM images of the nanocomposites that TiO_2 NPs nearly completely covered the exfoliated GO sheets, therefore the good adsorption property of GO was highly hindered towards the model pollutant.

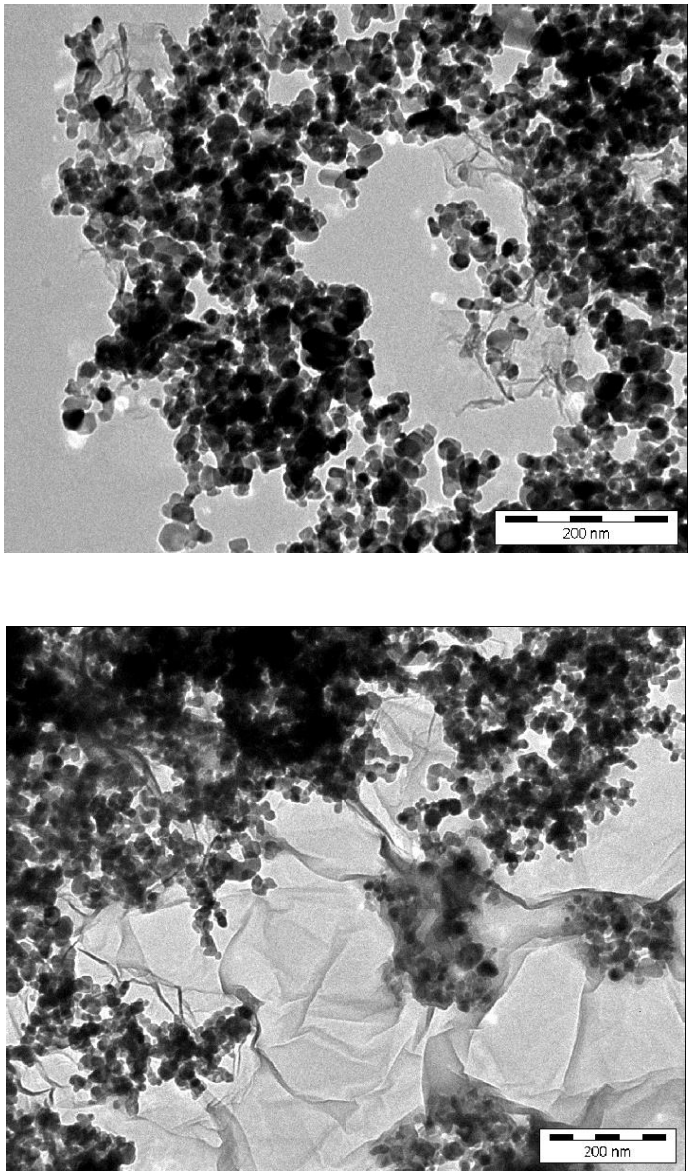

Figure 7 TEM images of TiGO-10 nanocomposite.

5.1.2. Photochemical transformation of GO in TiGO due to UV-irradiation

It has been reported that chemical transformation of GO into rGO occurs in the presence of reducing agents, e.g. hydrazine [132,133] or sodium borohydride, by means of electrochemical reduction

[134, 135] during hydrothermal reaction in the absence [136] or presence of TiO_2. [130] It has been also shown that the loss of functional groups and restoration of extended 2D graphene sheets can be facilitated by UV-irradiation [137] in the sole presence of an electron donor [138] and in the presence of electron donor, catalysed by TiO_2. [139]

The colour of originally light grey TiGO nanocomposites became darker and eventually black with the duration of UV-irradiation either suspended in d.i. water, phenol solution or casted on an electrode as a film. [140] This was a clear sign of the chemical transformation of GO into a more reduced graphene-like carbonic compound (rGO). The phenomenon was then evidenced by XPS and electric conductivity measurements. XPS spectra was obtained for TiGO-2 nanocomposite. The sample was collected from the photoreactor before and after 2 hrs of photocatalytic run (will be discussed later under *Section 5.1.3*) to study the photochemical transformation of the material. *Figure 8* shows the region of C 1s at binding energy of between ca 282-289 eV. After deconvolution of the data, three components were identified which were assigned to aromatic/graphitic carbon atoms (C=C) at ~ 285 eV; epoxy and hydroxyl groups (C-O-C and C-OH, respectively) at ~287 eV; and finally carbonyl and carboxyl groups (C=O and O=C-OH), respectively. The area of peak at ~287 eV, assigned to epoxy and hydroxyl groups, relative to the peak at ~885 eV, assigned to C=C aromatic carbon rings, significantly decreased which suggests the loss of epoxy and hydroxyl groups due to UV-irradiation. In the same time, the peak at ~ 289 eV did not change significantly which suggests that carbonyl and carboxyl groups remained intact, therefore it which means that the full restoration of the poly-aromatic graphene structure was not complete after one cycle. These findings correspond with the results of another group [139] where it was shown that ~ 50% of the oxygenated sites underwent chemical reduction in the presence of TiO_2 and EtOH under UV-illumination but not the carboxylic group. It strongly suggest that these functional groups are more resistant to reduction. A charge induced shift of the peak positions with ca 0.5 eV towards higher energies also confirms the transformation of GO into a more conductive material (rGO).

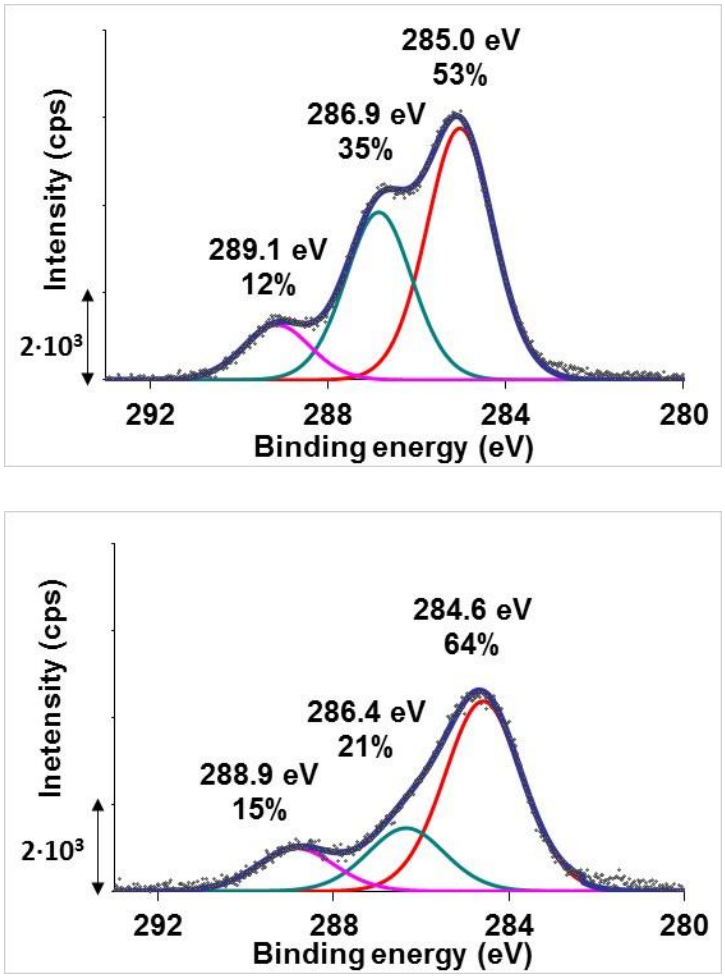

Figure 8 High resolution XP spectra of TiGO-2 (a) before and (b) after the first photocatalytic cycle

Along with the chemical transformation, a significant increase of the electric conductivity of the nanocomposite was facilitated which was due to the restoration of the extended π-electron structure of graphene-like sheets. To study the resulted changes of electric conductivity of the nanocomposite, TiGO-2 was cast on an interdigitated gold electrode and irradiated by a 70 W UV-rich light source (emission spectrum not presented) in ambient conditions and in saturated water vapour. As-synthesized GO sheets or films are typically insulating, exhibiting a sheet resistance of about 1012 Ω/sq or higher. The relative electric conductance (G/G_0, where G is the conductance measured after a certain time of the irradiation and G_0 is the conductance before irradiation) is plotted in the function of irradiation time in a logarithmic representation in *Figure 9***.** The GO-G transformation was found to be more pronounced in saturated water vapour: while the relative electric conductance increased 25-fold times in ambient conditions, it increased 100-fold times under saturated water vapour. It has to be noted that using the same light source did not induce the reduction of pure GO in the absence of TiO_2 irradiated for 2 hrs, however a 630-fold increase of electric conductivity increase was realised when using a 400

W Hg-arc lamp (emission spectrum not presented). This finding indicated that the reduction of GO can be facilitated using UV-light only, but the presence of TiO_2 significantly accelerates the process due to the produced electrons in the valence band.

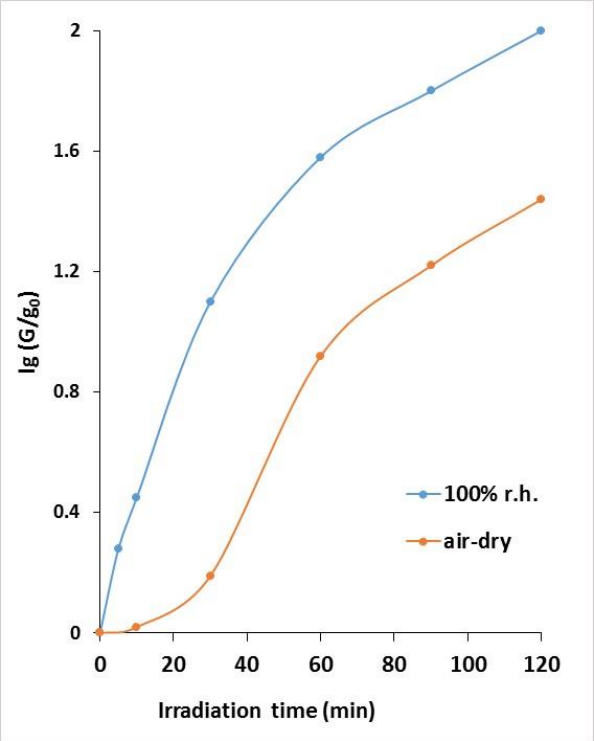

Figure 9 Figure G/G_0 Logarithmic plots of relative electrical conductance of TiGO-2 films at U = 10 V as a function of irradiation time in air-dry state and in 100% relative humidity.

5.1.3. Photocatalytic activity and reusability of TiGO nanocomposites

Photocatalytic activity of TiGO-1; TiGO-2 and TiGO-5 nanocomposites were probed for the UV-Vis assisted photocatalytic degradation of 1 mmol/L aqueous phenol solution and contrasted to that of reference P25 TiO_2. It was found that the presence of GO decreased the photocatalytic activity which was more pronounced with GO content. While the photocatalytic conversion rate of phenol for pure TiO_2 was 98%, it was 85%; 82% and 73% for TiGO-1; TiGO-2 and for TiGO-5, respectively (*Table 2*). This is controversial to most reported papers where the authors reported increased charge separation and increased photocatalytic activity of TiO_2-graphene oxide nanocomposites prepared by similar method.[141] The reason of the observed phenomenon might be rooted in the followings: first of all, TiO_2 NPs are deprived from a high amount of active surface (and active sites) to interact with the phenol molecules because they were immobilised on a support. This phenomenon for supported photocatalysts is quite common. Second, since GO absorbed a high amount of photons in a wide range of the UV-Vis spectrum therefore hindered the excitation of TiO_2 which eventually led to retarded photocatalytic activity. From a practical point of view, a photocatalyst should be able to perform under

repeated photocatalytic cycles. The reusability of TiO_2 on different supports, such as silica gel, glass beads and quartz sand for photocatalytic degradation of phenol was investigated by another research group. [142] They found 5-12 % decrease of photocatalytic efficiency by the end of the 4th run. Other researchers found 10% decrease of the catalyst on active carbon support after the 5th run of phenol decomposition. [143] To investigate the reusability of the nanocomposite, TiGO-2 was irradiated in 1 mmol/L phenol solution and then regained by centrifuging the irradiated suspension.

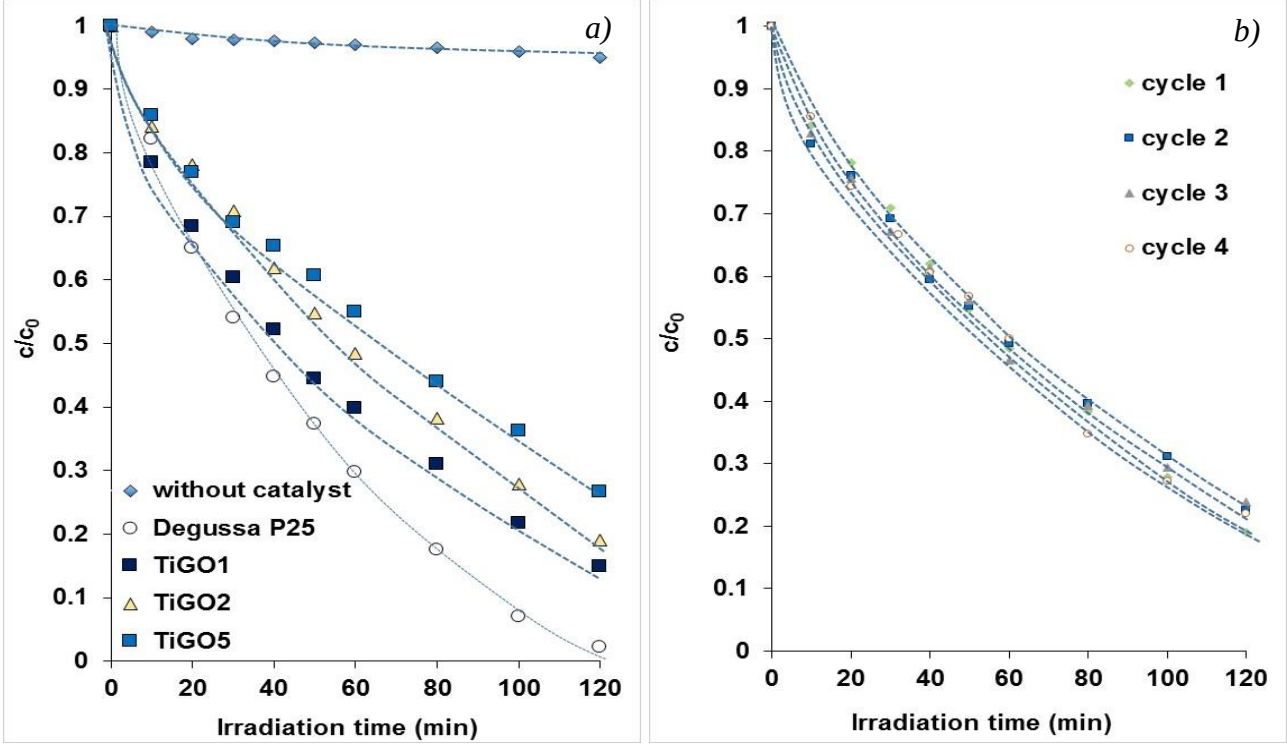

Figure 10 Photodegradation of phenol *a)* on different TiGO samples *b)* on TiGO-2 under repeated photocatalytic cycles

Table 2 Photocatalytic activity of TiGO nanocomposites and reference TiO_2 in the photooxidative phenol degradation reaction

Nr	Sample ID	Conversion (%)	k (1/min)	R^2	Δm_{Phenol} (mg) 120 min	Δm_{Phenol} (mg /g TiO_2)
1	Degussa P25	97.9	0.0263	0.9269	32.8	87.5
2	TiGO-1	85.1	0.0156	0.9925	30.0	80.7
3	TiGO-2 *cycle 1*	80.9	0.0129	0.9891	27.0	73.5
4	TiGO-5	73.3	0.0106	0.9901	25.6	71.8

5	TiGO-2 cycle 2	77.5	0.0121	0.9918	27.02	67.4
6	TiGO-2 cycle 3	76.0	0.0121	0.9942	24.8	67.8
7	TiGO-2 cycle 4	77.9	0.0126	0.9931	24.9	71.8

The photocatalytic cycles were repeated 4 times and between each cycle the nanocomposite was regained from the reaction medium, washed with distilled water, dried and re-suspended in 1 mmol/L of phenol solution. Similar phenol conversions were found (*Table 2*, rows 3 and 5-7) implying that the nanocomposite was suitable for repeated use without observable loss of the photocatalytic efficiency (~3 -4 %). As it was shown before, that the photochemical transformation of GO into rGO occurred after 1 photocatalytic cycle.

5.1.4. Sedimentation properties of the nanocomposites

As it has been pointed out earlier, obtaining efficient recovery of the photocatalyst NPs from the reaction medium after the photocatalytic treatment is a key aspect to both cost and public health concerns when considering commercialised applications. It is known that TiO_2 forms a kinetically very stable colloid dispersion in aqueous medium due to its high surface charge and electric double layer and it can be destabilised only at around the p.z.c. (pH~6.6) where the repulsive charges are minimised and slight aggregation of the NPs and slow sedimentation can occur. This property makes TiO_2 less desired as a potential candidate as a large-scale photocatalytic water cleaning agent, because its recovery requires special chemical treatment or filtration. On this motivation, the sedimentation properties of TiGO nanocomposites were compared to TiO_2 in distilled water and in aqueous phenol solution. In *Figure 11* sedimentation of P25 (on the left) and TiGO-5 (on the right) are compared at pH=6, close to the p.z.c. value of TiO_2. The figure clearly shows that TiGO-5 was settling with a much higher settling velocity and the sedimentation time was significantly reduced (note the different time scale for the two systems). Due to the loss of net surface charge around the isoelectric point at pH = 6.6, suspensions of bare TiO_2 undergo coagulation, i.e. formation of aggregates by cohesion between particles of the same kind. These aggregates are large enough to be dragged down by gravitational force, which cannot be compensated by Brownian motion. However, the TiO_2 aggregates will settle with different velocities due to their poly-disperse size distribution, which results in a diffuse sedimentation front and a very slow rate for the smallest fractions. Complete sedimentation of the TiO_2 NPs could be observed after 24 hrs but only in the pH range close to the p.z.c (pH = 6 –8). In contrast

to that, TiGO-5 was settling with a sharp settling interface, leaving a clear supernatant above and it formed voluminous and easily re-dispersible sediments indicating that it was a highly destabilised disperse system composed of large aggregates. After 5 minutes of settling almost the entire solid phase was settled. This was followed by slow syneresis, i.e. decrease of the sediment volume by a slow expulsion of the aqueous medium from the coherent inorganic gel network formed by the flock-like particles.

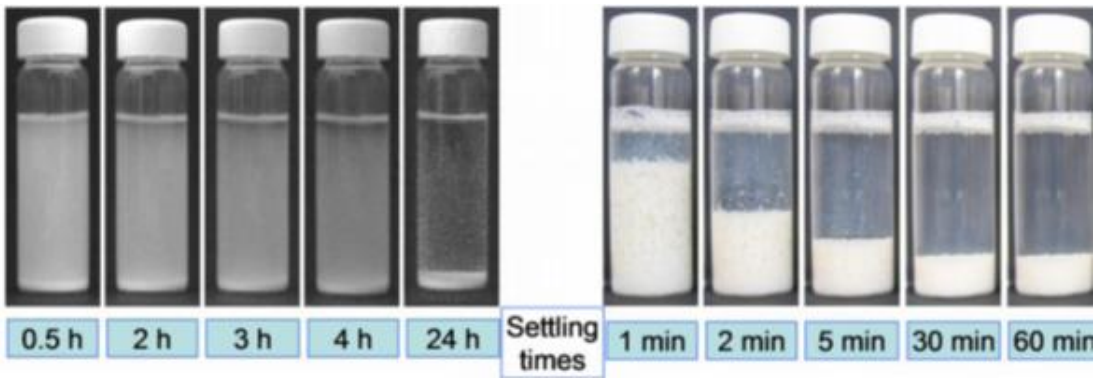

Figure 11 Photographs of sedimentation 1g/L P25 TiO_2 (left) and 1g/L TiGO-5 (right) suspensions in distilled water at pH = 6.

To quantify the sedimentation of TiGO nanocomposites, sedimentation profiles were studied by observing the sedimentation of 1 g/L TiGO dispersions in the function of settling time. Two factors; the effect of GO content in the nanocomposite; and the effect of irradiation time on the sedimentation were investigated. Sigmoidal curves with a nearly linear middle section were obtained for all samples, which is typical for suspensions exhibiting zone settling characteristics. The slope of the line fitted over this range equals to the terminal settling velocity (TSV) of suspended particles, which is the maximum attainable settling rate established when the drag forces just compensate gravitational pull. The inset of *Figure 12 a)* shows that the TSV changed inversely with the GO loading. This means that the sedimentation was gradually hindered by the presence of large, anisometric GO particles. As proven by turbidimetry, the clarified supernatants contained less than 5 mg/L TiO_2 for all GO loadings, which means that at least 99.5% of catalyst particles were efficiently separated from the liquid phase. The process of sedimentation of the nanocomposites was accelerated due to the occurrence of UV-induced chemical transformation since the loss of functional groups endowed the TiGO nanostructures with a more hydrophobic character. It was represented by the accelerated displacement of settling fronts *Figure 12 b). Inset b* shows that the TSV = 2 cm/min of the non-treated TiGO-5 exceeded 10 cm/min after prolonged illumination. TiGO-5 nanocomposite was irradiated with UV-light (same as that was used for the photocatalytic test reactions) in 1 mmol/L phenol solution and samples were

taken after 0; 20; 40; 60; 80 and 120 min. Photographs of the settling suspensions were taken after 1; 30 and 60 min of storage time (Please refer to the photographs in *Appendix 2*). Turbidimetry showed that no more than 0.3% of the solid remained in the supernatant for these dispersions. Since the supernatant was transparent, it was a clear indication that the progressive decomposition of GO did not result in the detachment of the nanosized TiO_2 aggregates. As a consequence, it was assumed that van der Waals adhesion forces took the key role to immobilise TiO_2 on the GO sheets. However, these interactions are very weak and thus heterocoagulation can be reversed by mechanical energy. This assumption was also studied when exposing TiGO suspensions to strong acoustic irradiation (300 kHz, 80 W).

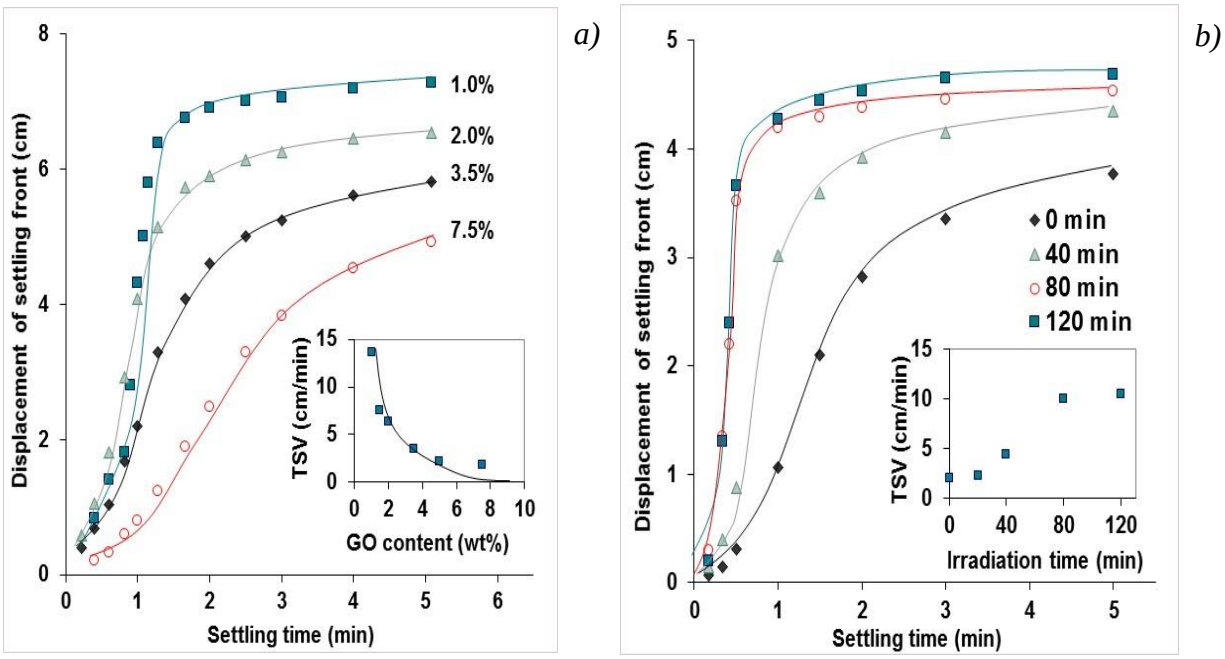

Figure 12 Settling profiles of 1 g/L TiGO nanocomposite dispersions *a)* at different GO contents and *b)* 1 g/L TiGO-5 in 1 mmol/L phenol solution after different illumination times. The insets show the terminal settling velocities as the function of GO loading and the irradiation time, respectively.

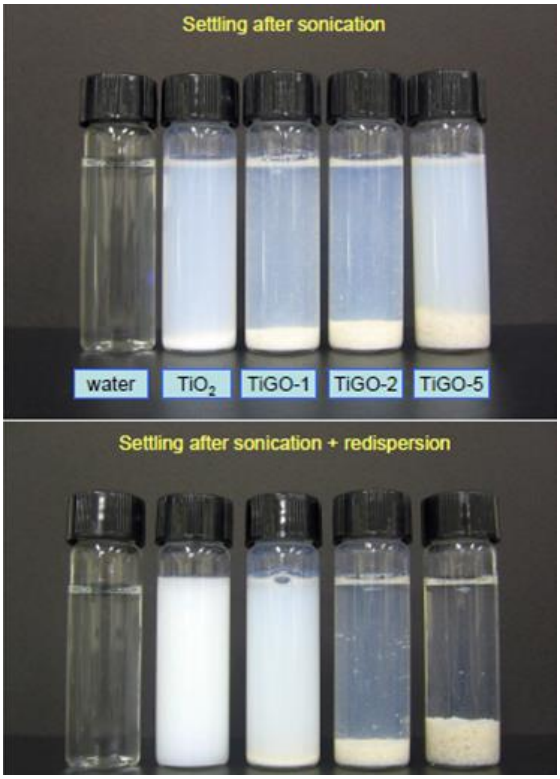

a)

b)

Figure 13 Photographs of 0.1 g/L P25 TiO_2 and TiGO suspensions *a)* after 20 min of sonication at 300 kHz and 80 W and *b)* after sonication followed by gentle redispersion
Settling time: 30 min and 5 min for *a)* and *b)*, respectively

It was observed that the nanocomposites could be disintegrated to a certain extent when applying short (maximum of 20 min) sonication cycles. Photographs of P25 TiO_2, TiGO-1, TiGO-2 and TiGO-5 are shown in *Figure 13 a)* after acoustic irradiation. The nanocomposites were almost as turbid as TiO_2 after 30 min of settling time. Surprisingly, when these dispersions were gently re-stirred and were left again to settle, accelerated sedimentation could be observed, representative of well-aggregated dispersions, but leaving a lot of worn off TiO_2 in the supernatant. After that, gently re-shaking the suspensions facilitated the re-organisation of TiGO network (*Figure 13 b)).* The above phenomena was observed after arbitrarily repeating the strong and mild re-dispersion steps.

5.2. Nanocomposite films

5.2.1. TiO_2/ZrO_2/Hect nanocomposite films

First, nanocomposite films were prepared using inorganic compounds, i.e. ZrO_2 and Na-Hect ($Na_{0.3}(Mg,Li)_3Si_4O_{10}(OH)_2$) to support TiO_2 and to provide better dispersion of this material within the matrix of nanocomposite films. The added inorganic supports were optically transparent in the UV-

Vis region as it is illustrated in *Figure 14*. From a practical point of view, it is important that the incoming light can be absorbed by the photocatalyst within the nanocomposite film thus TiO_2 can be activated or with other words the generation of electron-hole pairs can be triggered. The ratio of support to photocatalyst was changed between 0-1, but the ratio of ZrO_2 and Hect was kept constant (9:1), accordingly, nanocomposite films with photocatalyst content of 0; 20; 40; 60; 80; 100 wt% were prepared.[144] The compositions for the prepared nanocomposite films are shown in Figure 15. The most advantageous properties of the supports were that they kept the TiO_2 NPs well dispersed in the nanocomposite structure resulting in a microporous structure therefore EtOH could easily enter into deeper layers of the films. SEM image illustrates the porous structure of the nanocomposite coating *Figure 16*. Besides preventing TiO_2 from aggregation, Na-Hect had another prominent role in the photocatalytic process: Due to its high surface area (305.0 m^2/g) it readily adsorbed EtOH vapour. As the EtOH molecules were adsorbed on the surface of the nanocomposite films (and inside of the pores) they were easily attacked by the generated ROS. Until the eventual event of complete mineralisation of EtOH into CO_2 and H_2O, a series of chemical transformation and generation of intermediate products occur on the surface of TiO_2. Studies in the literature agree that the reaction pathway starts with the formation of acetaldehyde, but its further transformation into intermediate products i.e., acetic acid, formaldehyde and formic acid can go through different pathways depending on the reaction conditions**.** [145, 146] Study of the generation of different intermediate products and determination of the reaction pathway are out of the scope of this work.

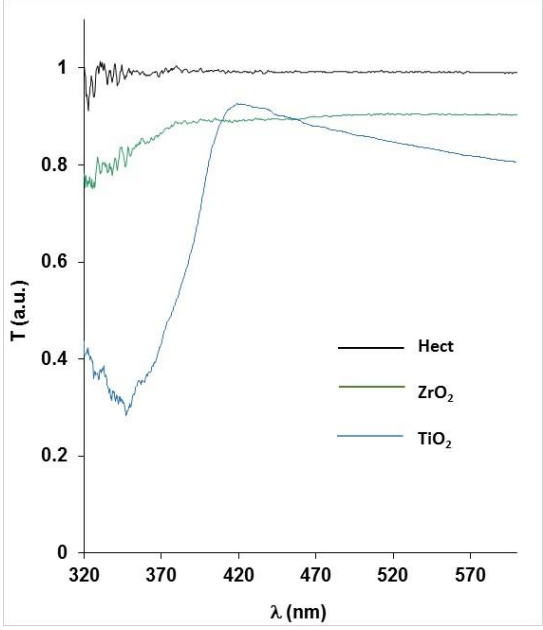

Figure 14 Transmission spectra of Hect and ZrO_2 supports and reference TiO_2

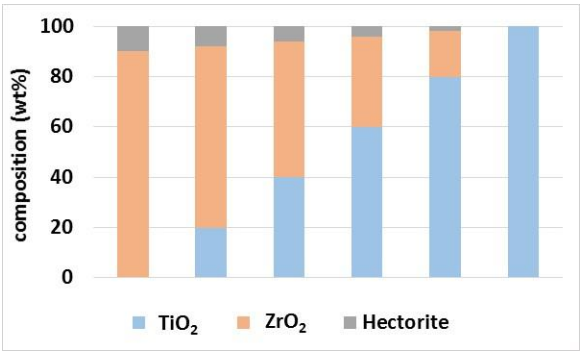

Figure 15 Composition of nanocomposite films prepared with inorganic supports

The as-prepared nanocomposite films were probed for the photocatalytic degradation test on EtOH. The obtained data is summarised in *Table 3*.

It is seen that after addition of more than 40 wt% of photocatalyst to the nanocomposite layer, the photocatalytic efficiency did not improve. With other words, similar photocatalytic activity could be obtained with nearly half as much of photocatalyst as it was obtained in the case of pure TiO_2 film. This effect is owing to the propitious properties of supporting materials and the phenomenon is nominated as a synergistic effect. *Figure 17* illustrates the correlation between photocatalyst content and photocatalytic activity. The dotted line corresponds to a theoretical value of decomposed TiO_2 if a linear relationship is assumed between catalyst content and degraded amount of EtOH. The black curve represents the measured values. It does not start from zero, because there some decrease of EtOH concentration due to the adsorption of the supports without any TiO_2 (*Table 3*, first row: 0 wt% TiO_2).

Table 3 Photocatalytic degradation of EtOH on TiO_2/ZrO_2/Hect nanocomposite films

Nr	TiO_2 content (wt%)	Conversion (%)	k (1/min)	R^2	ΔmEtOH (mg)	ΔmETOH (mg/g kat)	ΔmETOH (µg/cm^2)
1	0	15.43	0.0028	0.9912	0.35	-	7.74
2	20	40.73	0.0091	0.9910	0.66	58.59	14.61
3	40	51.86	0.0129	0.9696	1.04	44.27	23.02
4	60	48.22	0.0113	0.9958	1.10	33.00	24.55
5	80	51.50	0.0122	0.9979	1.16	25.45	25.79
6	100	47.67	0.0107	0.9999	1.09	19.87	24.33

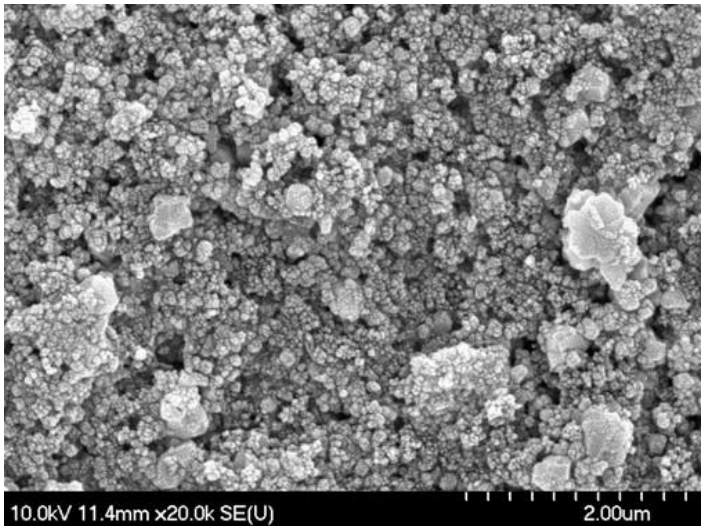

Figure 16 SEM image of nanocomposite film containing 80 wt%TiO_2 and 20 wt% supports (ZrO_2:Hect = 9:1)

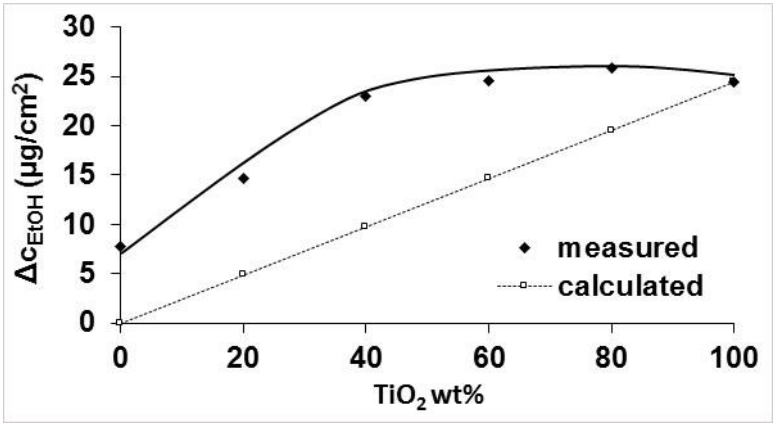

Figure 17 Synergistic effect between TiO_2 and supports in the nanocomposite film

5.2.2. TiO_2/p(EA-co-MMA) nanocomposites

Concerns has been shown, not surprisingly, about the applicability of organic substances, such as polymers, as photocatalyst supports due to their limited stability. It is known that most polymers show limited resistance towards high energy UV-photons (UV-B and higher energy range). Furthermore, once this material is contacted with a photocatalyst, the degradation process may be even more accelerated due to the presence of generated ROS. Furthermore, the question is raised: Can this feature be turned into an advantage?

In this section, photocatalytic properties and applicability of polymer supported photocatalyst nanocomposite films are investigated. The coatings (d ~ 100 μm) were prepared in such a way that only the upper 25% region of the coating contained evenly distributed photocatalyst NPs in the matrix

and the bottom region was functioning as a base to provide strong attachment to the glass support. p(EA-co-MMA) is a water-soluble compound and transparent in the UV-Vis range, therefore it is an ideal material to provide a matrix for hydrophilic TiO_2 well-dispersed in its network and also to allow UV photons to penetrate in the layer and be absorbed by the embedded photocatalyst NPs. However it is a common problem that immobilisation of the photocatalysts results in decreased photocatalytic activity owing to the unavoidable decrease in active surface area. As a matter of fact, the polymer thoroughly covers the photocatalyst NPs expectedly resulting in momentous decrease of the photocatalytic activity. Furthermore, it is known that most polymers tend to photodegrade under UV-irradiation which can be a huge drawback of applying them as photocatalysts supports. Below in *Table 4*, photocatalytic activity of TiO_2 nanocomposites are compared to pure TiO_2 with organic or inorganic binding. It is clear that addition of 40% Hect did not decrease significantly the rate of ethanol conversion on TiO_2. However, owing to the notable amount of adsorbed EtOH on Hect, the absolute amount of degraded EtOH is half of that on pure TiO_2. The addition of polymer results in tremendous decrease in the photocatalytic activity by enwrapping the catalyst NPs, but the film can be "re-activated" by a long UV-irradiation with high energy UV (UV-B,-C). The emission spectrum of light source is attached in *Appendix 1*.

Table 4 Photocatalytic activity of nanocomposite films supported by Hect and p(EA-co-MMA)

Nr	Film ID with 60% TiO_2 content	Conversion (%)	k (1/min)	R^2	Δm_{EtOH} (mg)	Δm_{EtOH} (mg /g kat)	ΔmETOH ($\mu g/cm^2$)
1	TiO_2	58.6	0.0107	0.9999	1.27	22.6	13.35
2	TiO_2/Hect	52.5	0.0128	0.9957	0.60	16.3	13.45
3	TiO_2/(EA-co-MMA) before UV	23.8	0.0044	0.9926	0.60	17.3	13.35
4	TiO_2/(EA-co-MMA) after UV	58.5	0.0145	0.9997	1.37	39.4	30.44

When exposed to UV irradiation, polymers suffer photo-induced oxidative degradation which involve breaking of the polymer chains, production of free radicals, reduction of molecular weight and eventually, deterioration of mechanical properties.[73] The chemical formula of the p(EA-co-MMA) and

the schematic representation of photocatalyst/polymer nanocomposite films are shown in *Figure 18* before and after the UV-treatment. On the left it can be seen that the polymer fully covers TiO_2 NPs on the surface, which can significantly hinder the photocatalytic activity of the coating. After exposing the nanocomposite film, surface TiO_2 NPs are expected to show up due to partial degradation of the upper layers of the polymer matrix. As the UV-irradiation proceeds, deeper and deeper layers of the film are affected resulting in a more porous structure.

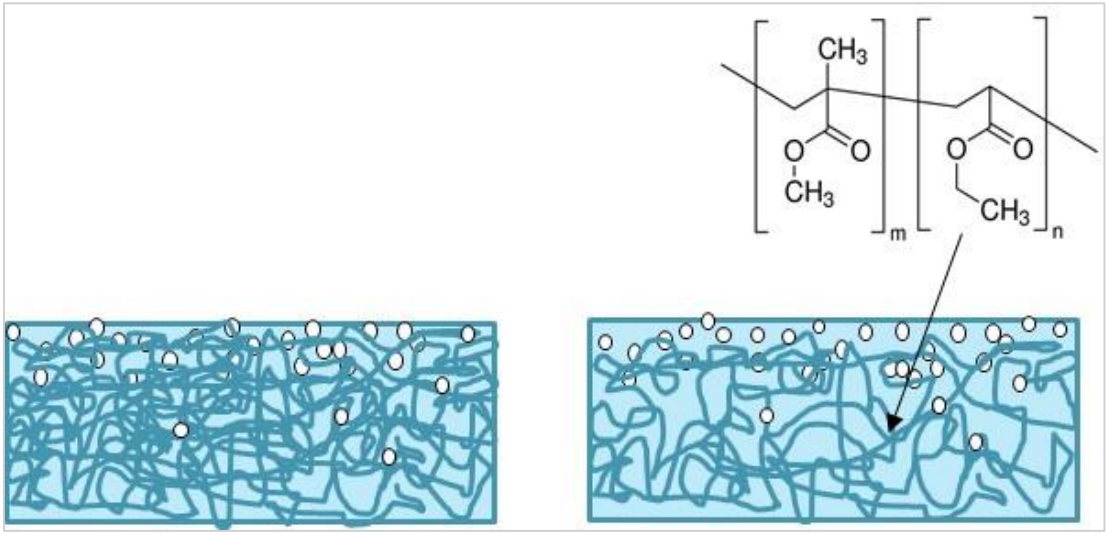

Figure 18 Scheme representing the concept of UV-treatment

To investigate the phenomenon further both TiO_2 and Ag-TiO_2-containing nanocomposites were prepared with addition of polymer binder. After that the nanocomposite films along with the pure polymer film were irradiated by high-energy UV-C photons for different time intervals (0-48 hrs) and the resulted changes in the structrure were analysed.

The chemical transformation of the nanocomposite films were represented by FTIR measurements.[147] FTIR spectra of the pure polymer film and nanocomposite coatings before and after irradiation were recorded. The characteristic IR vibration regions representing the chemical structure of p(EA-co-MMA), i.e., the stretching vibrations of C – O and C = O at 1157 and at 1725 cm^{-1}, respectively and the symmetric and assymetric vibrations of – CH_3 groups at 1382 and at 1447 cm^{-1}, respectively are shown in *Figure 18 a*) and C– H vibrations at 3100- 2800 cm^{-1} are shown in *Figure 18 b*) (only shown for TiO_2/p(EA-co-MMA). The decreasing absorbance of these characteristic bands, due to irradiation, indicated the photodegradation of p(EA-co-MMA) in case of all films, but, not surprisingly, the degradation was accelerated in the presence of photocatalyst due to the generated ROS. The broad absorption band at around 3000 cm^{-1} increased due to UV irradiation, indicating the generation of O – H bonds, referring to the generation of surface – OH groups and the presence of

adsorbed water. After 48 hrs of irradiation, a slight increase of peak at 1623 cm^{-1}, indicative of H – O – H vibrations was assigned to the presence of physisorbed water. It is known that due to UV irradiation, TiO_2 reversibly adsorbs both, dissociative and non-dissociative water. [148] This leads us to the well-known phenomenon of super-hydrophilic property of TiO_2 which is induced due to UV-irradiation, starting with the formation of photo-generated electrons and holes. The electrons tend to reduce Ti(IV) cations to the Ti(III) state and the holes oxidise O^{2-} anions and oxygen atoms are ejected creating oxygen vacancies. Water molecules then can occupy these vacancies producing adsorbed – OH groups which are responsible for the super-hydrophilic surface [24] It was reported earlier that this feature can be maintained for not longer than 1 or 2 days before re-exposed to UV-light again. Therefore it is important to note that the FTIR spectra were recorded within 24 hrs after irradiation, or with other words, within the timeframe of the probable existence of UV-induced super-hydrophilicity. [149]

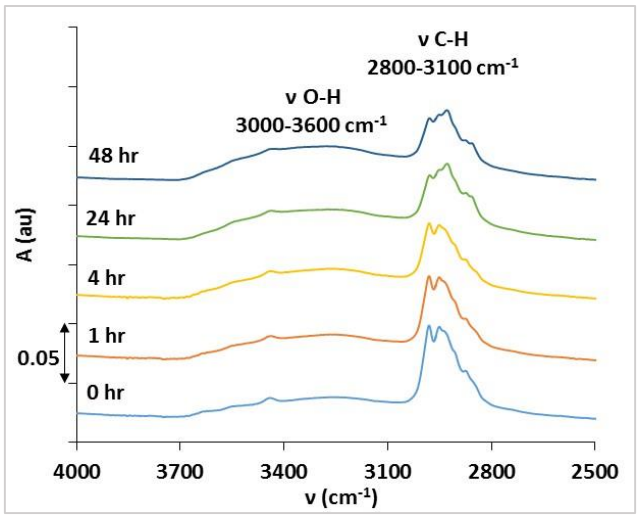

a)

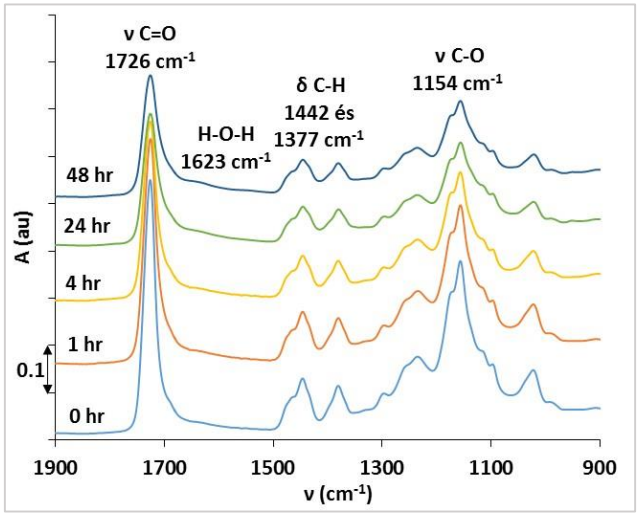

b)

Figure 18 FTIR regions *a)* 900-1900 cm^{-1} *b)* 2500-4000 cm^{-1}, recorded on irradiated (0–48 hrs) TiO_2/p(EA-co-MMA) film

The kinetics of polymer degradation obviously differ for the pure polymer and for nanocomposite films. To compare the alterations in photo(catalytic) degradation of the polymer matrix for the three systems, a summary of values for decrease of absorbance (%) of at the characteristic group frequencies are given in *Table 5***.** It can be seen that the polymer degraded much faster in the presence of photocatalyst NPs, especially in case of Ag-TiO_2, which is the photocatalyst with higher photocatalytic activity and the rate of generated ROS is expectedly higher than that on TiO_2.

Table 5 Relative decrease in absorbance of main group frequencies for pure polymer, TiO_2 and Ag-TiO_2/polymer nanocomposites

Nr	FTIR vibration	p(EA-co-MMA)	TiO_2/p(EA-co-MMA)	Ag-TiO_2/p(EA-co-MMA)
		% decrease in absorbance		
1	ν C-O	19.5	43.4	58.5
2	δ C-H, sym	21.1	21.3	34.0
3	δ C-H, asym	0.0	24.2	42.9
4	ν C=O	26.6	51.7	67.3
5	ν C-H	14.5	17.7	28.6

Furthermore, comparing the FTIR regions of irradiated and non-irradiated films show significant differences in the region of 1710-1740 cm^{-1}(*Figure 20* a-b**).** There is an obvious broadening of the C=O peak towards the lower wavenumber regions for the pure polymer (*Figure 20 a)* as the UV-irradiation proceeds. This shoulder was not found in case of nanocomposites, where photocatalyst NPs were present (only for TiO_2/p(EA-co-MMA) is shown in *Figure 20 b*). This refers to the formation of some side products (unidentified) which was obviously present in the highest amount for the pure polymer. It is possible that for each system the polymer degrades through the same reaction pathway, but in the case of nanocomposites, the intermediate transforms further into CO_2 and H_2O.

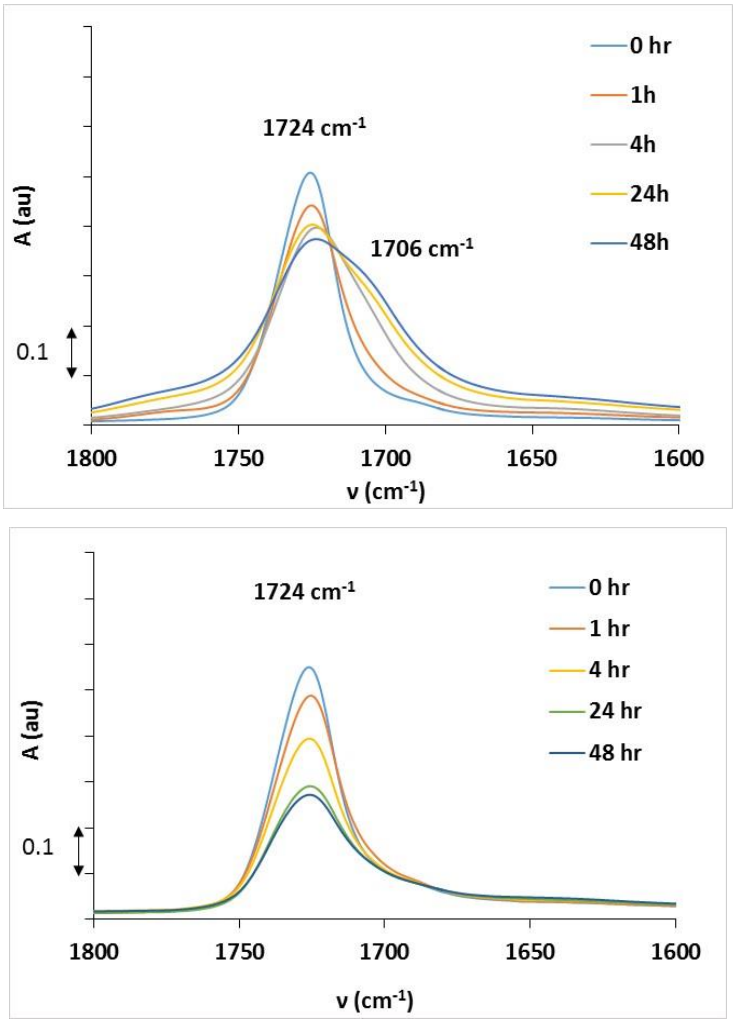

Figure 20 FTIR spectra at the C=O region for *a)* pure p(EA-co-MMA) and *b)* TiO_2/p(EA-co-MMA) after different irradiation times with UV-light

Morphological changes of the surface of the nanocomposite films were well represented by the SEM images which were taken on a nanocomposite film containing 60 wt% TiO_2 before (*Figure 21 Figure 21 a)* and after 24 hrs of irradiation (*Figure 21 b*). It can be well seen that for the non-irradiated film the polymer almost completely covers the NPs forming a continuous, rather smooth surface. In contrast to this, it can be seen that the polymer visibly wear off from the surface and most of the TiO_2 NPs are uncovered.

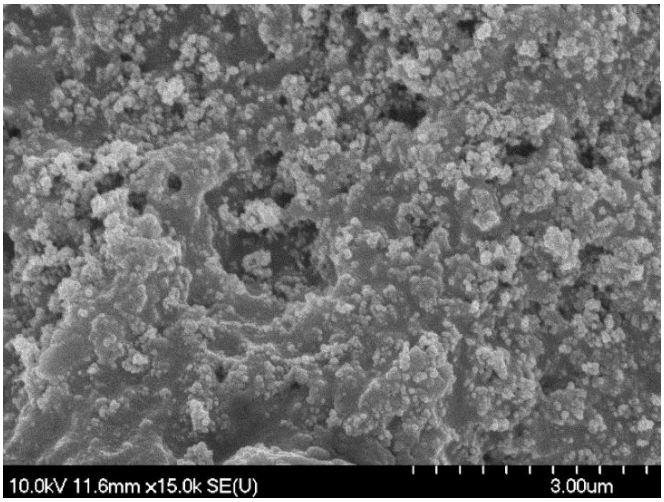

a)

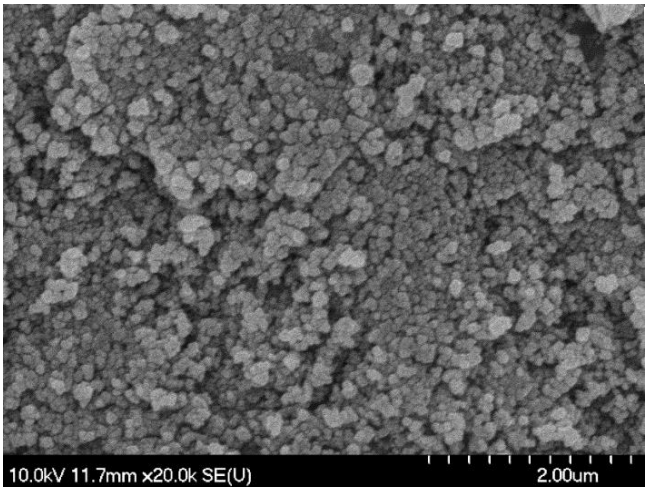

b)

Figure 21 SEM images of TiO_2/p(EA-co-MMA) films *a)* before and *b)* after 24 hrs of UV-irradiation.

The change of surface morphology and chemical composition (increased photocatalyst to polymer ratio) could be also registered by contact angle measurements. The wettability profiles of the nanocomposite films were obtained in the function of UV-irradiation time. The wetting properties are basically determined by the surface free energy on the solid/liquid/vapour interface and it is greatly affected by the chemical and topological properties of the solid surface.

In case of chemical or topological heterogeneity, there is a difference between the advancing and receding contact angles, which is manifested in the contact angle hysteresis, which is basically the difference of the previous two.

Advancing and receding contact angles were recorded before irradiation (*Figure 22 a*) and after given periods of UV irradiation on the pure polymer film and on the nanocomposite films and equilibrium contact angles were calculated following Tadmor's approach (Eq. 6-8). [150]

$$\theta_0 = \arccos\left(\frac{\Gamma_a\theta_a + \Gamma_r\theta_r}{\Gamma_a + \Gamma_r}\right)$$

Eq. 6

where

$$\Gamma_a = \left(\frac{sin^3\theta_a}{2 - 3cos\theta_a + cos^3\theta_a}\right)^{1/3}$$

Eq. 7

$$\Gamma_r = \left(\frac{sin^3\theta_r}{2 - 3cos\theta_r + cos^3\theta_r}\right)^{1/3}$$

Eq. 8

The surface free energy of the solid surfaces was consequently calculated from the measured contact angle data, following Chibowski, [151] where the total apparent surface free energy (γ_s^{tot}) of the solid is determined according to Eq. 9:

$$\gamma_s^{tot} = \frac{\gamma_l(1 + cos\theta_a)^2}{(2 + cos\theta_r + cos\theta_a)}$$

Eq. 9

wher γ_l describes the surface tension of the probe liquid (which is 72.8 mN/m for water at 20 °C) contact and θ_a and θ_r are the advancing and receding contact angles, respectively. While the equilibrium contact angle and calculated surface free energy did not change significantly due to the high-energy UV-treatment in case of pure polymer surface, a rapid decrease of contact angle values was observed for the nanocomposite films. The equilibrium contact angles and surface free energies are presented in *Figure 22b and c*, respectively. This observation was due to the change of surface chemistry. Firstly, it was because of the evolution of well-known super-hydrophilic property of TiO_2. The generated charge carriers due to photo-excitation migrate to the surface of the NP where the holes become trapped at bridging oxygen-sites and facilitate their ejection. This is followed by dissociation of water molecules which causes the evolution of hydroxyl-groups on the surface. The process can continue until the surface becomes saturated with highly polar hydroxyl-group.[152]

Secondly, the more hydrophilic TiO_2 NPs were unfold from the polymer cover, thus the surface energy was increasing and it was manifested by decrease of measured contact angles. The photo-induced super-hydrophilic feature of the surface also contributed to the accelerated increase of contact angle values in case of the nanocomposites. This phenomenon, however was observed to be much more significant for the TiO_2-containing nanocomposite than that for its Ag-TiO_2 counterpart. The evolution of surface – OH groups on TiO_2 was so pronounced after 60 minutes of irradiation that the contact angle was measured to be 0°. It was found that the measured contact angles on the Ag-TiO_2/polymer nanocomposite film showed a much slower rate of decrease due to irradiation. With other words, the evolution of – OH surface groups on the Ag-TiO_2 was slightly limited. The reason for that might be, according to our speculation, was that the nucleation of Ag NPs on the TiO_2 surface started on the high energy active sites (oxygen vacancies) [153] which retards the formation of – OH groups on the TiO_2 surface therefore the surface free energy of the Ag-TiO_2 containing nanocomposite film was increased much slower due to UV irradiation than that of measured on the TiO_2/polymer film.

a)

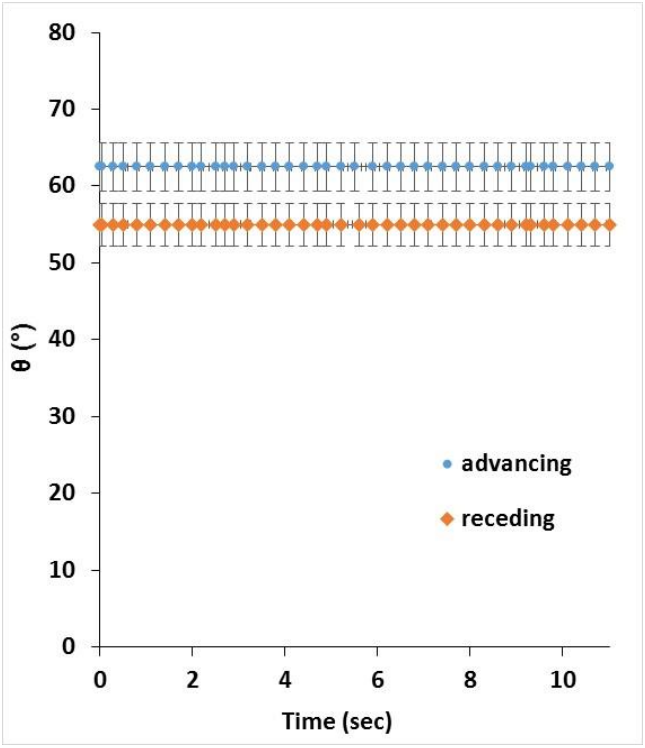

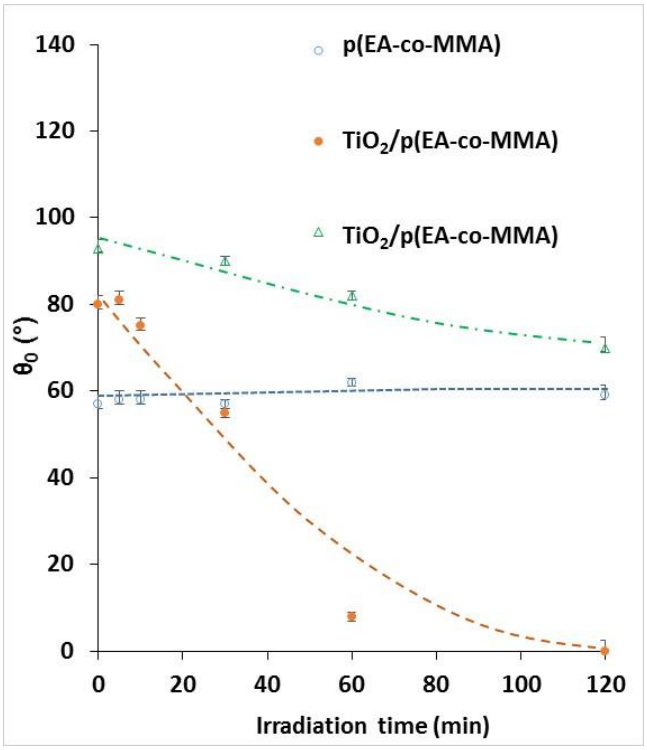

b)

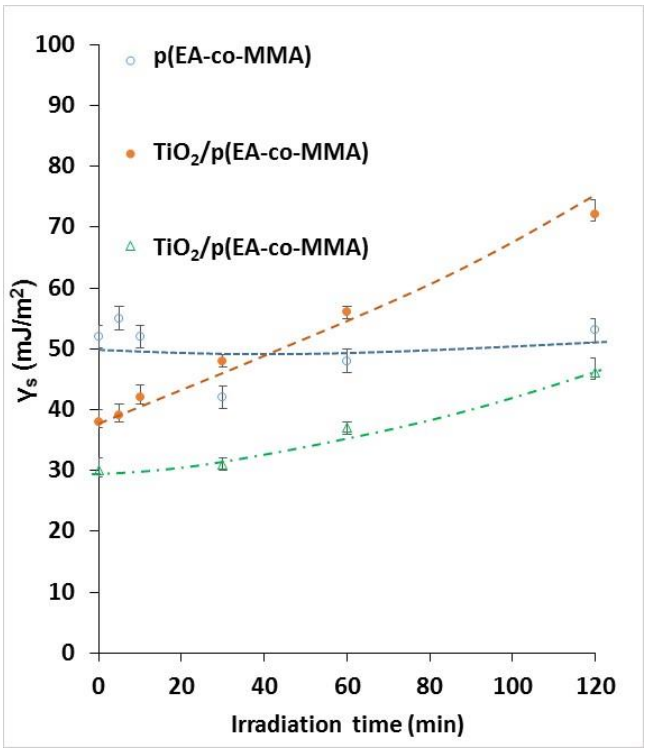

c)

Figure 22 a) Recorded advancing and receding contact angles on pure polymer film *b)* equilibrium contact angles and *c)* surface free energies of polymer and TiO_2- and Ag-TiO_2-containing nanocomposite films in the function of irradiation time with high energy UV

A facile validation method to estimate the mechanical stability of the coatings was carried out by the adhesive tape test. Stripes of adhesive tapes were attached to the surface of the non-irradiated and irradiated films and were removed by a rapid pull. The adhesive tapes removed from the surface of non-irradiated and irradiated coatings are shown in *Figure 23*. After 4 hrs of UV-treatment of the TiO_2/p(EA-co-MMA) coating, the amount of NPs attached to the tape started to visibly increase. The appearance of solid particles on the tape for the Ag-TiO_2/p(EA-co-MMA) coating it was obvious after 1 hr of irradiation. This finding is in correlation with the FTIR results, showing that the photodecomposition of polymer matrix was accelerated in the presence of Ag-TiO_2, since this material is more active than pure TiO_2. The method is not quantitative, but suitable to measure the effect of UV-deterioration on the coherence of the network of the nanocomposite films.

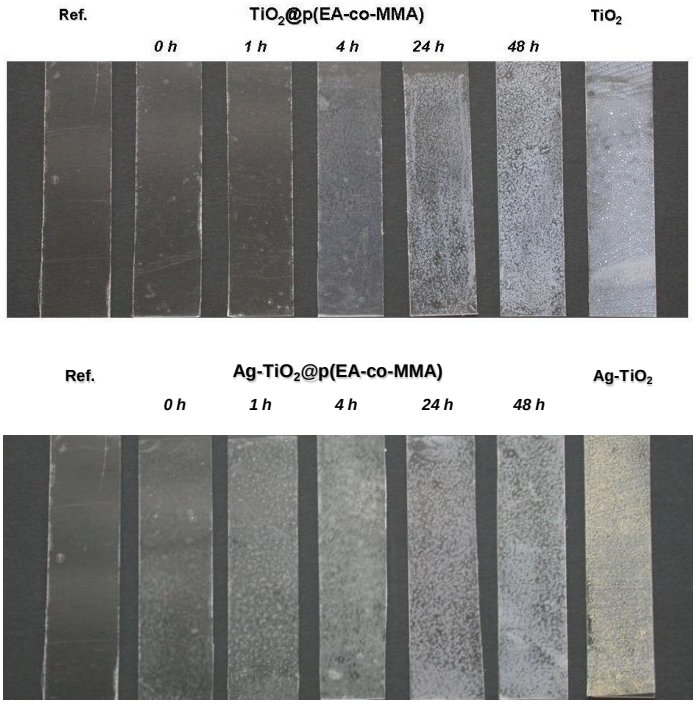

Figure 23 Photographs of adhesive tapes, applied then removed from the surface of coatings and fixed on glass slides for *a)* TiO_2 and *b)* Ag-TiO_2 containing nanocomposite coatings. On the left reference is shown: clean adhesive tape fixed on glass slide

As for the photocatalytic activity tests, a light source had much less intensive emission lines in the UV range than that was used for the UV-treatment. Evaluation of the photocatalytic activity of the nanocomposite films was carried out by the standard EtOH photodegradation test and the results are summarised in *Table 6.* It can be seen that the non-pre-irradiated TiO_2 and Ag-TiO_2/polimer nanocomposites showed fairly low conversion rates of EtOH; 23.9 and 36.0%, respectively. As the

irradiation time intervals for the preliminary UV-treatment was increased, consequently higher rates of EtOH conversions were observed. Due to the UV-treatment, on one hand, a loss of mechanical stability was observed as a consequence of declining integrity of the polymer network. On the other hand, significant increase in the photocatalytic activity was found owing to a higher local catalyst content. Photo-induced degenerative oxidation was observed due to high-energy photon irradiation in the absence of photocatalyst. Furthermore, the degradation of polymer was accelerated in the presence of TiO_2 and Ag-TiO_2 photocatalysts due to the deteriorating effect of generated ROS. However, it is important to note that during the photodegradation of polymer matrix, even if there were some degradation products of the polymer, they did not poison the photocatalyst NPs or block the active sites of TiO_2 because the photocatalytic efficiency of the nanocomposites showed positive correlation with the duration of UV-treatment. However, the decrease of mechanical stability can be a significant drawback in case of long-term use and for practical applications.

Table 6 Photocatalytic degradation of EtOH on TiO_2 and Ag-TiO_2/polimer nanocomposite films.

Nr	Sample ID	UV (h)	Conversion (%)	k (1/min)	R^2	Δm_{EtOH} (mg) 60 min	Δm_{EtOH} (mg /g kat)	Δm_{ETOH} ($\mu g/cm^2$)
1	p(EA-co-MMA)	0	26.98	0.0080	0.9980	0.57	16.96	12.67
2	TiO_2/ p(EA-co-MMA)	0	22.92	0.0056	0.9985	0.45	13.39	10.00
3		1	34.82	0.0112	0.9982	0.70	20.83	15.56
4		4	36.12	0.0121	0.9977	0.73	21.73	16.22
5		24	48.34	0.0151	0.9995	0.96	28.57	21.33
6		48	57.58	0.0178	0.9997	1.06	31.55	23.56
7	TiO_2	-	58.64	0.0142	0.9992	1.29	23.04	28.67
8	Ag-TiO_2/p(EA-co-MMA)	0	36.02	0.0113	0.9990	0.72	21.43	16.00
9		1	35.20	0.0114	0.9977	0.73	21.73	16.22
10		4	51.38	0.0161	0.9993	1.05	31.25	23.33
11		24	63.52	0.0219	0.9944	1.30	38.69	28.89
12		48	65.59	0.0223	0.9940	1.28	38.10	28.44
13	Ag-TiO_2	-	81.62	0.0207	0.9882	1.65	29.39	36.58

We found that addition of inorganic compounds, such as layered silicates, can significantly slow down the degenerative processes of the polymer matrix, because up to a certain extent it prevents the polymer from the generated ROS. This is reflected by the photocatalytic activity test results: Photocatalytic efficiency of 60%TiO_2/polymer nanocomposites was compared to that of contained 10 wt% hectorite as well besides the polymer (i.e. 60%TiO_2/30%polymer/10%hectorite nanocomposites). Similarly to previous experiments, significant increase of photocatalytic activity was observed for the photocatalyst/polymer films, but much slower efficiency-increase was observed in the presence of Hect as it is shown in *Figure 24.*

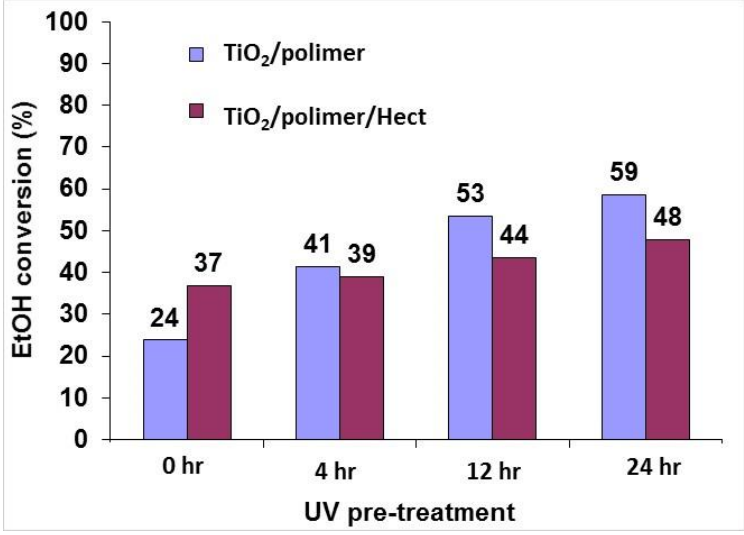

Figure 24 Photocatalytic EtOH conversion on TiO_2/polymer and on TiO_2/polymer/Hect films after 0-24 hrs of UV-treatment

5.3. $Ag_x(O)$-TiO_2 heterostructures

Ag-TiO_2 and Au-TiO_2, prepared by in situ chemical deposition method with a metal content of 0.5 wt%. The colour of the modified TiO_2 was brown and purple for silver and gold modified samples, respectively (*Figure 25* (right)). The measured UV-Vis spectra for the prepared samples are shown on *Figure 25* (left). Strong Vis absorption peaks were detected at λ_{max} = 455 nm and at λ_{max} = 560 nm, for Ag-TiO_2 and for Au-TiO_2, respectively. It has been shown that the size of loaded metal NPs significantly influence the photocatalytic performance of the heterostructure in several ways. Clearly, the size of metal NP determines its optical properties i.e. the location of plasmonic band in the UV-Vis spectrum as it was indicated in the literature summary. However, further results on how the size affect the carrier transport are somewhat contradictory. Subramanian et al. showed that the size of Au NP affects the Fermi-level on the metal-semiconductor interface and smaller the deposited Au NPs were, the more negative shift of the Fermi level was observed which consequently resulted in better

charge separation and reductive power of the composite system.[154] On the other hand, other study by J. Lee et al. suggests that the photogenerated charge transfer was higher in case of larger Au NPs.[155] TEM image of Ag-TiO_2 indicate the particle size of the Ag NPs on TiO_2 which was ca. 10-12 nm *Figure 26*. It can be seen that Ag NPs were attached to the surface of TiO_2 as primary particles and particle aggregates. This variation was manifested in the wide Vis plasmon band.

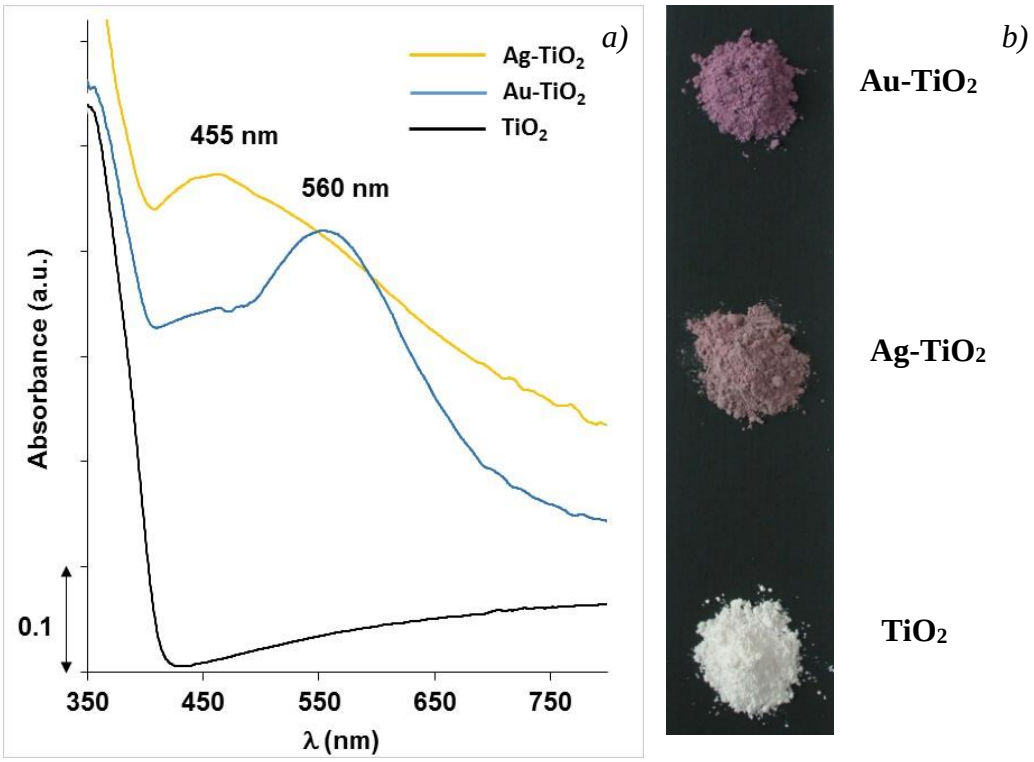

Figure 25 UV-Vis absorbance spectra of unmodified TiO_2, Au-TiO_2 and Ag-TiO_2 and photograph of pure and modified TiO_2 samples

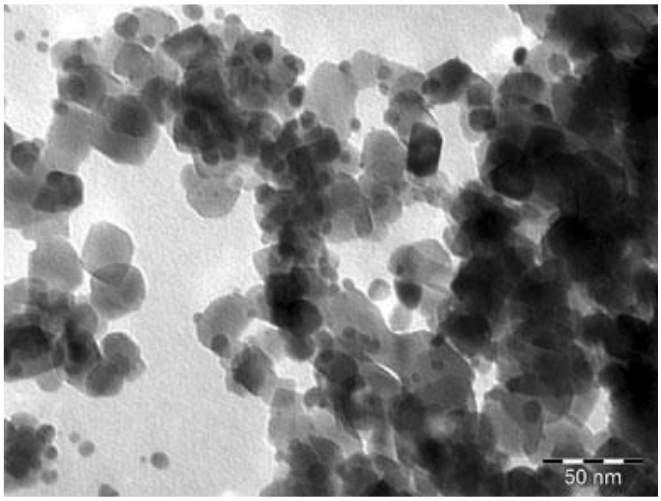

Figure 26 TEM image of Ag-TiO_2

As for the photocatalytic activity, both, Ag and Au-modified samples showed higher photocatalytic performance than pure TiO_2. The results are presented in *Table 7*, rows 2 and 6, respectively. It is shown, that containing 0.5 wt% metal, Ag-TiO_2 is significantly more active than its Au-containing counterparts. It could be owing to the broader Vis-range plasmon peak than that for the Au-TiO_2 since it overlaps with two prominent emission peaks of the light source (λ = 435nm and 545 nm). It might be also owing to the higher quality factor which is in direct correlation with the strength of plasmonic response of metal NPs, [106] however there is not much difference between the absorbance of plasmonic bands for Ag and Au in the samples. Since silver is more economical to use and it showed higher photodegradation rates for ethanol, gave a good reason to carry on our research using silver to modify TiO_2 instead of Au.

Table 7 Summary of data on the photocatalytic degradation of Ag-; AgO-; Ag_2O- and Au-modified TiO_2.

Nr	Sample ID	Conversion (%)	k (1/min)	R^2	Δm_{EtOH} (mg)	Δm_{EtOH} (mg /g kat)	Δm_{ETOH} ($\mu g/cm^2$)
1	TiO_2	58.6	0.0145	0.9994	1.27	22.60	28.13
2	Ag-TiO_2	81.6	0.0207	0.9882	1.65	29.39	36.58
3	Ag_2O-TiO_2	80.8	0.0259	0.9925	1.64	29.24	36.38
4	Ag_2O-TiO_2 (Sigma) no UV	85.3	0.0294	0.9838	1.86	33.13	41.23
5	Ag_2O-TiO_2 (Sigma) after UV	84.78	0.0288	0.9827	1.78	30.72	39.60
6	AgO-TiO_2	81.7	0.0265	0.9905	1.65	29.49	36.70
7	Au-TiO_2	65.4	0.0175	0.9984	1.45	25.97	32.31
8	TiO_2*	41.66	0.0087	0.9954	1.06	103.6	0.023
9	Ag_2O (Sigma)*	11.98	0.0024	0.9537	0.38	30.36	0.008

** Film thickness for TiO_2 and Ag_2O in rows 8 and 9 was ~0.2 mg/cm^2*

It is also known that Ag NPs deposited on TiO_2 showed photochromism, which is a feature of materials that react reversibly to light. [152, 156, 157] As a matter of fact, these materials find exciting applications such as displays, smart windows and memory devices. [158] Silver NPs, deposited on TiO_2 surface, go through reduction and oxidation states which is ensued with a change of colour. The displayed colour can be tuned by the wavelength of irradiating light irradiation. Once the as prepared Ag-TiO_2 film was irradiated with Vis light-emitting LED (λ_{max}=450 nm), the originally brownish colour of the film started to fade and gradually turn into light pink. The change was followed by UV-DR measurements and the recorded spectra are shown in *Figure 27 a).*

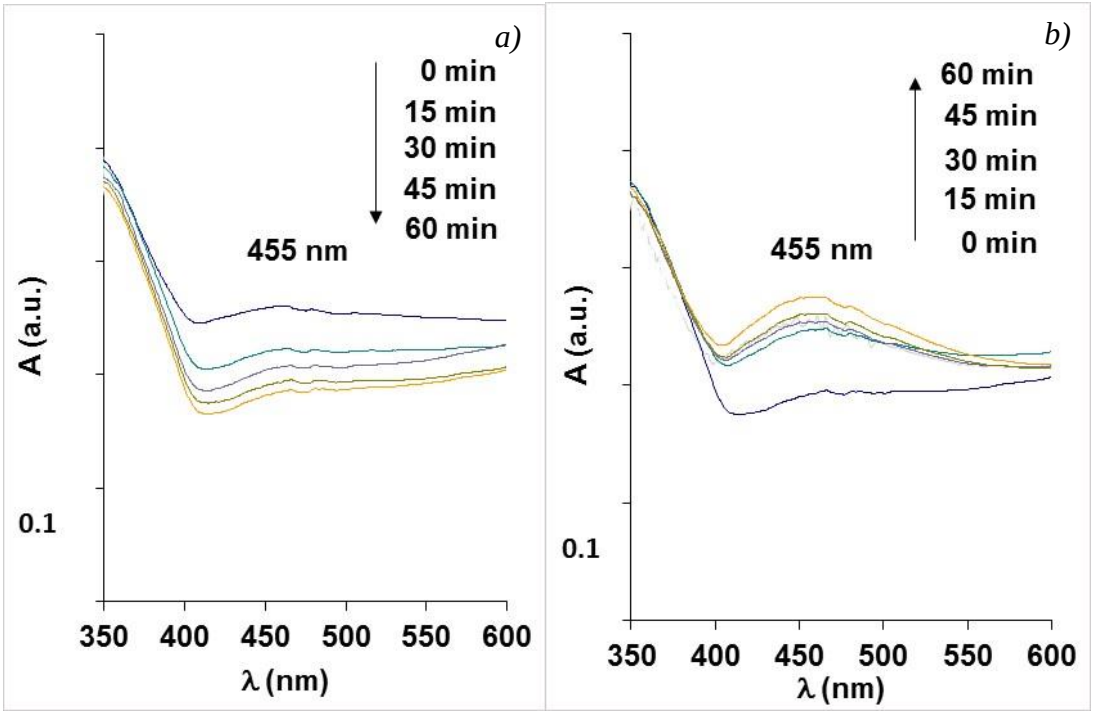

Figure 27 UV-Vis absorbance spectra of Ag-TiO_2 film under Vis (λ_{max}=450 nm) and under UV (λ_{max}=254 nm) irradiation for 1 hr

The process could be readily reversed and the original brownish colour could be re-obtained by shining UV-rich light on the film (λ_{max}=254 nm). The corresponding UV-Vis spectra are shown in *Figure 27 b).* The process was owing to the reversible interconversion of Ag(0) into Ag(I). Once the film was illuminated with Vis light with emission wavelength overlapping the plasmonic band of the nanostructure, the electrons of Ag(0) interacted with the light through surface plasmon resonance and the Ag(0) states gradually converted into Ag(I). The corresponding XPS spectra provided further evidence. The Ag 3d regions of Ag-TiO_2 film before and after 1 hr with illumination with UV light is shown in *Figure 28***.** The peaks at ~374 and ~378 can be attributed to Ag $3d_{3/2}$ and Ag $3d_{5/2}$ binding energies, respectively. The position of XPS peaks, located at 373.3 eV and at 367.4 eV, for Ag $3d_{3/2}$

and $3d_{5/2}$, respectively were shifted towards higher binding energy regions which refers to more metallic environment. [159, 160 161, 162]

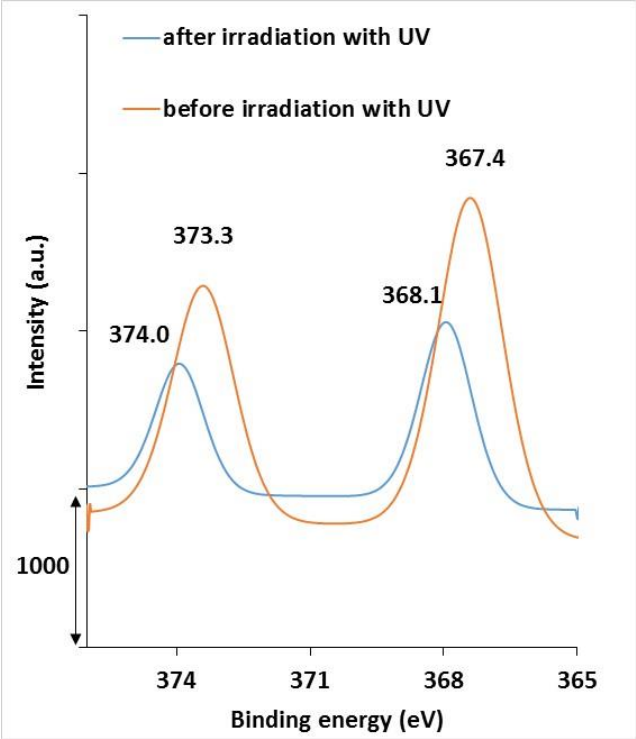

Figure 28 Ag 3d region of XPS spectra of Ag-TiO_2 before and after 1 hr of UV-irradiation (λ_{max}=254 nm)

Further Ag- containing samples were prepared by mixing Ag_2O or AgO with TiO_2 (wt_{Ag}%=0.5). The photocatalytic activity of 4 samples were contrasted. One was the Ag-TiO_2 sample, prepared by in situ wet chemical reduction. Furthermore, Ag_2O and AgO, prepared as described in the *Materials and methods* section were mixed with TiO_2 and named Ag_2O-TiO_2 AgO-TiO_2, respectively. Finally Ag_2O, purchased from Sigma Aldrich was used to prepare a sample similarly to the other Ag_2O-containing counterparts and was entitled as Ag_2O-TiO_2 (Sigma). The purchased Ag_2O powder was grinded in a mortar with TiO_2 then stirred in aqueous suspension. When it was well dispersed, the small amount of added black Ag_2O powder was not visible with the naked eye and the colour of suspension was white. The same was observed for the other Ag_2O containing samples, but after the photocatalytic test runs, the colour of the photocatalyst films became homogeneous orange/brown indicative of appearance of metallic silver due to UV photons coming from the light source. It has to be pointed out that in case of the silver oxide samples there was actually no surface deposition of Ag on TiO_2 only physical mixing which excludes the possibility of strong attachment between TiO_2 and Ag_xO. Furthermore, another crucial point is that there was a different state of oxidation state and also different size of silver (-

oxide) NPs. The light microscopy image of commercially purchased Ag_2O particles after grinding in a mortar is shown in *Figure 29*. Obviously, the size of these particles was much larger, 1-2 µm then that of in situ deposited Ag NPs on TiO_2. Even with ultrasonic irradiation it was impossible to break these particles, thus large Ag_2O particles were visibly settled at the bottom of the glass vessel. Thus the size of Ag particles, mixed to TiO_2, was surely not in the nanoscale range. This is why it is so interesting that there was no significant difference in the photocatalytic activity of the obtained samples. The conversion rates varied between 80.8 and 85.3 % (*Table 7, rows 2-6).* There is surely more about the photocatalytic enhancement than plasmonic effects. Ag_2O is on the other hand a Vis-light sensitive photocatalyst, it is a p – type semiconductor with a band gap of 1.2 eV [163] and with a chemically unstable nature. Considering this, there is a p – n type junction on the Ag_2O/TiO_2 interface. [164] Owing to its limited chemical stability Ag_2O is hardly ever used on its own. Pure Ag_2O was also tested for the photocatalytic test reaction. The only technical difficulty was that it was impossible to prepare a homogeneous film with the same catalyst content as in the previous cases (1.25 mg/cm^2). Thus, a pure Ag_2O film was prepared with a catalyst coverage of 0.27 mg/cm^2 and its photocatalytic activity was compared to a TiO_2 film (m_{TiO2} = 0.25 mg/cm^2) as it is shown in *Figure 27 rows 8-9.* Although less than TiO_2, but Ag_2O also has some activity also under present reaction parameters.

Further experiments were conducted on Ag_2O-TiO_2 (Sigma) film after 1 hr of UV irradiation. The expected change of colour was significant already after 15 min and eventually resulted in a homogenously purple film (*Figure 30)* which indicating the Ag_2O – Ag conversion. However, it was found that the photocatalytic activity was identical as that of the non-irradiated film (*Table 7, rows 4 -* 5). Despite of the obvious change of colour, it is possible that not many metallic Ag sites were formed during the short irradiation time and under the photocatalytic tests both direction takes place Ag to Ag_2O and the other way around because the light source irradiates but UV and Vis rays.

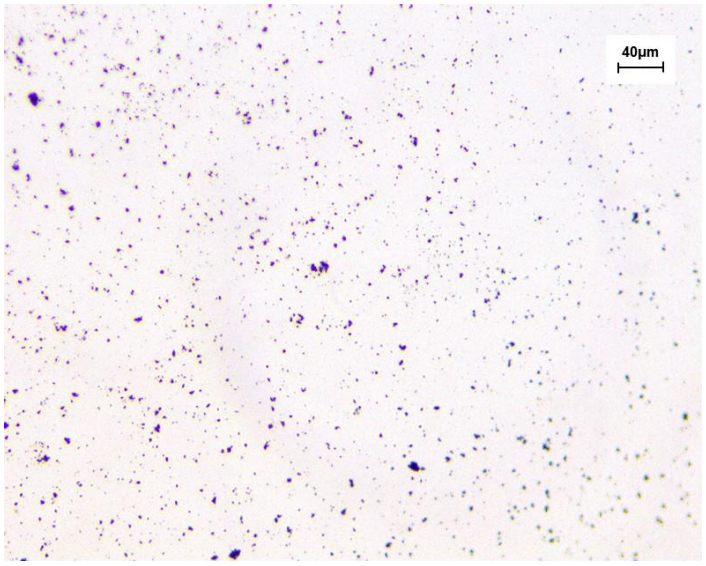

Figure 29 Light microscopy image of commercial Ag_2O after grinding

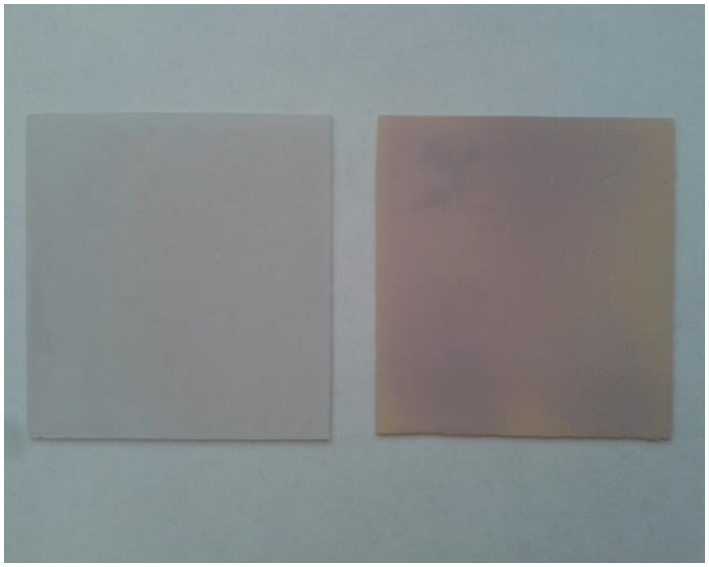

Figure 30 Photograph of Ag_2O-TiO_2 (Sigma) film before and after 1 hr of UV irradiation

5.4. TiO_2 NPs prepared by hydrothermal treatment of H-titanate nanofibers

As it has been pointed out earlier in *section 2.2*, the crystal structure has a paramount importance on the photocatalytic activity. In present section, the correlation between crystal phase composition, photocatalytic activity (PC) and photoelectrochemical (PEC) features is shown through the example of a series of TiO_2 NPs, which were prepared by acidic hydrothermal treatment of H-TNFs.[165] By changing only one parameter of the synthesis reaction, i.e. the concentration of HNO_3 (c= 0.05–4 mol/L), the structural and morphological features of the NPs could be altered. Therefore a variety of TiO_2 samples were obtained such as anatase-rich nanofibers, brookite-rich rhomboid NPs and rutile-rich flower-like assemblies of nanowires.

5.4.1. Structural, optical and electronic characterisation

Due to the acidic hydrothermal process the H-TNFs were re-crystallised as TiO_2 and the composition of crystal phases was fundamentally affected by the acid concentration of the reaction medium. A trend of formation of anatase-, brookite-, and finally, rutile-rich samples was observed as the initial pH of reaction medium was lowered. The XRD patterns of the TiO_2 products are shown in *Figure 31* Reflections at $2\theta = 25.28°$, 37.80°, 48.05°, 53.89° and 55.06° were observed in HPT0.05, HPT0.1, HPT0.5 and HPT1 which can unambiguously be assigned to (101), (004), (200), (105) and (211) planes of anatase, respectively. Furthermore, HPT0.1, HPT0.5, HPT1, HPT2 and HPT4 samples showed reflections at 25.36°, 25.71°, 30.83° and 36.28°, 48.06° and 55.28° which were indicative of

(210), (111), (211), (102), (321) and (421) planes of brookite, respectively. Rutile phase was identified in samples from HPT0.5 to HPT4 from reflections at 2θ = 27.24°, 35.81°, 40.93°, 53.90°, 56.20° and 68.45°, which were referred to (110), (101), (111), (211), (220) and (301) planes of rutile, respectively. By visually comparing the XRD patterns in *Figure 31*, it can readily be recognised that among relatively mild conditions anatase was the dominant crystal phase to be formed. Increasing the concentration of acid (0.5-2 mol/L HNO_3) in the reaction medium led to brookite, and finally rutile-rich samples (>2 mol/L HNO_3).

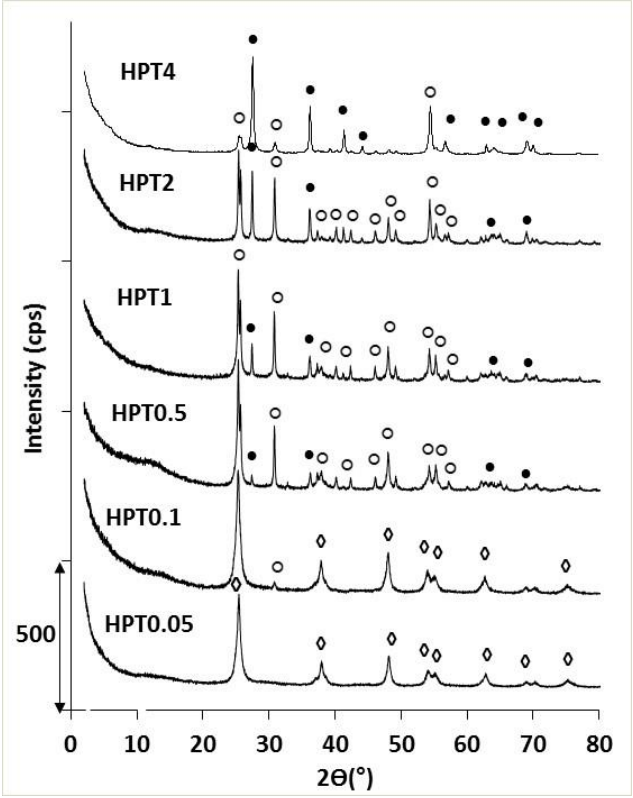

Figure 31 XRD patterns of HPT TiO_2 samples: ◊ Anatase; ○ Brookite; ● Rutile

Quantitative analysis of the crystalline composition of the TiO_2 samples was determined by Rietveld refinement and the composition of crystalline phases are summarised in *Table8.* It is worth noting that there was a small amount of amorphous TiO_2 present in all samples. While HPT0.05 contained solely anatase in the crystalline phase, a low amount of brookite (6.8%) was formed in HPT0.1 besides the dominant anatase phase. Further increasing the acid concentration, the amount of brookite phase became more significant and reached its highest proportion (74.8%) in sample HPT2. After this point ($\geq$ 2 mol/L HNO_3), the formation of brookite was hindered due to the progressive evolution of rutile. This latter phase was first detected in sample HPT0.5 in a small quantity (3.05 %). The volume-weighted domain size of the anatase, brookite and rutile crystallite sizes were determined from XRD

patterns based on Lorentz crystallite size-broadening, as shown in *Table8*. The anatase crystallites were observed to be relatively small (9.5 – 8.0 nm) in samples HPT0.05 to HPT1 and the average dimension slightly decreased with the progressive evolution of brookite at lower pH values. It was a competitive process between the different crystal phases: the size of anatase crystallites was gradually decreased as the proportion of brookite was increased. The brookite phase appeared first in HPT0.1 with an average crystallite size of 37.0 nm. This value was determined to be larger at higher acidic conditions for samples HPT0.5 and HPT1 (53.1 and 50.3 nm, respectively). After this significant increase in crystallite size, the growth was suppressed with the gradual increase of rutile, which first appeared in HPT1. The average crystallite size for rutile was first measured to be 47.0 nm for HPT1. When the pH was further decreased, the crystal size for rutile first increased to 63.4 nm (HPT1), and then gradually decreased to 24.0 nm (HPT4).

Table 8 Table Crystal phase composition of HPT TiO_2 samples obtained from XRD measurements by Rietveld refinement and volume weighted integral crystallite sizes calculated from Lorentz crystallite size broadening. The crystallites were assumed to be spherical.

Nr	Sample ID	Crystal phase composition (%)			Crystallite size (nm)		
		Anatase	Brookite	Rutile	Anatase	Brookite	Rutile
1	HPT0.05	100	-	-	9.5 ± 2.0	-	-
2	HPT 0.1	93.2 ± 1.2	6.8 ± 1.2	0	9.2 ± 3.1	37.0 ± 11	-
3	HPT 0.5	49.2 ± 2.9	47.7 ± 2.9	3.05 ± 2.9	8.0 ± 3.9	53.1± 3.7	47.0 ± 1.4
4	HPT1	34.4 ± 2.6	55.7 ± 2.7	9.9 ± 1.0	7.9 ± 5.4	50.3± 2.8	63.4 ± 7.3
5	HPT2	-	74.8 ± 1.1	25.2 ± 1.1	-	33.9 ± 0.5	49.7 ± 1.4
6	HPT4	-	27.5± 1.5	72.5± 1.5	-	15.9 ± 0.5	24.0 ± 0.3

The structural differences essentially influenced the evolution of morphology of NPs and as a result of various crystal phase compositions, various shapes of nanocrystals – such as fibres, rhomboid NPs and flower-like aggregates *Figure 32 a-i)* – were formed. Under the relatively mild acidic conditions (0.05 – 0.1 mol/L HNO_3), the elongated morphology of H-TNFs was conserved when the crystal phase was

transformed from hydrogen titanate into anatase, as it can be seen in the TEM images of HPT 0.05 and of HPT0.1 in *Figure 32 b)* and in *Figure 32 c-d)* respectively. It is due to the similar crystal structure of hydrogen titanates and anatase. As the transformation reaction does not have a high energy barrier, it take place among relatively mild conditions as an *in situ* rearrangement of the TiO_6 building blocks, the process is therefore considered as a topochemical reaction.[166] Further increase of the acid concentration (0.5 – 2 mol/L HNO_3), however, resulted in disappearance of the fibre-like structures and instead, rectangular (cube-like) NPs were formed with an edge length of ~100 nm for samples HPT0.5, HPT1 and HPT2 *Figure 32 f and g),* respectively). Due to extremely high acidic conditions (as it was the case for HPT0.5 –HPT2) the titanate is dissolved and a dissolution-re-crystallisation process takes place to form TiO_2. Ti–OH is protonised to generate Ti–OH_2^+ thus, due to the large amount of H^+ ions, the dehydration process of the structures is not favoured. The other reason for the hindrance of the formation of anatase is due to the repulsive forces between Ti–OH_2^+ and ^+H_2O–Ti, causing the TiO_6 octahedral units mainly being arranged via edge-sharing and giving rise to the formation of corner- and edge- sharing brookite and rutile polymorphs.[167] Crystal structures of the respective polymorphs were introduced under *section 2.1*., in *Figure 2.* The sample HPT0.1 was found to show interesting structural characteristics where the two reaction mechanisms (topochemical acid catalysed dehydration and dissolution – re-crystallisation took place simultaneously. As a consequence of the parallel processes, rectangular NPs were also observed besides the nanofibers. It is shown on the HRTEM image *Figure 32 d)* that the crystal structure was brookite (d_{111}=0.346 nm) and anatase (d_{101}=0.352 nm) for the nanocubes and for the nanofibers, respectively. In the case of HPT4, where extremely acidic medium was used, the morphological features were significantly different from those observed for the previous samples. HPT4 showed flower-like assemblies with a longitudinal diameter of ca. 1 μm. These structures were found to be built of radially aligned nanorods with a length of ~ 0.8 – 1 μm and a width of ~15 nm, shown in *Figure 32 h).* HRTEM image shows that the thinner fibres were epitaxially attached to each other *Figure 32 i)* as a result of dehydration and consecutive rearrangement and splitting of titanate nanostructure along the connecting corners of four TiO_6 repeating units.[168] The lattice distance was read as d = 0.346 nm from the inverse FFT image (not shown here) and was assigned to the (1 1 1) plane of brookite *Figure 32 i).*

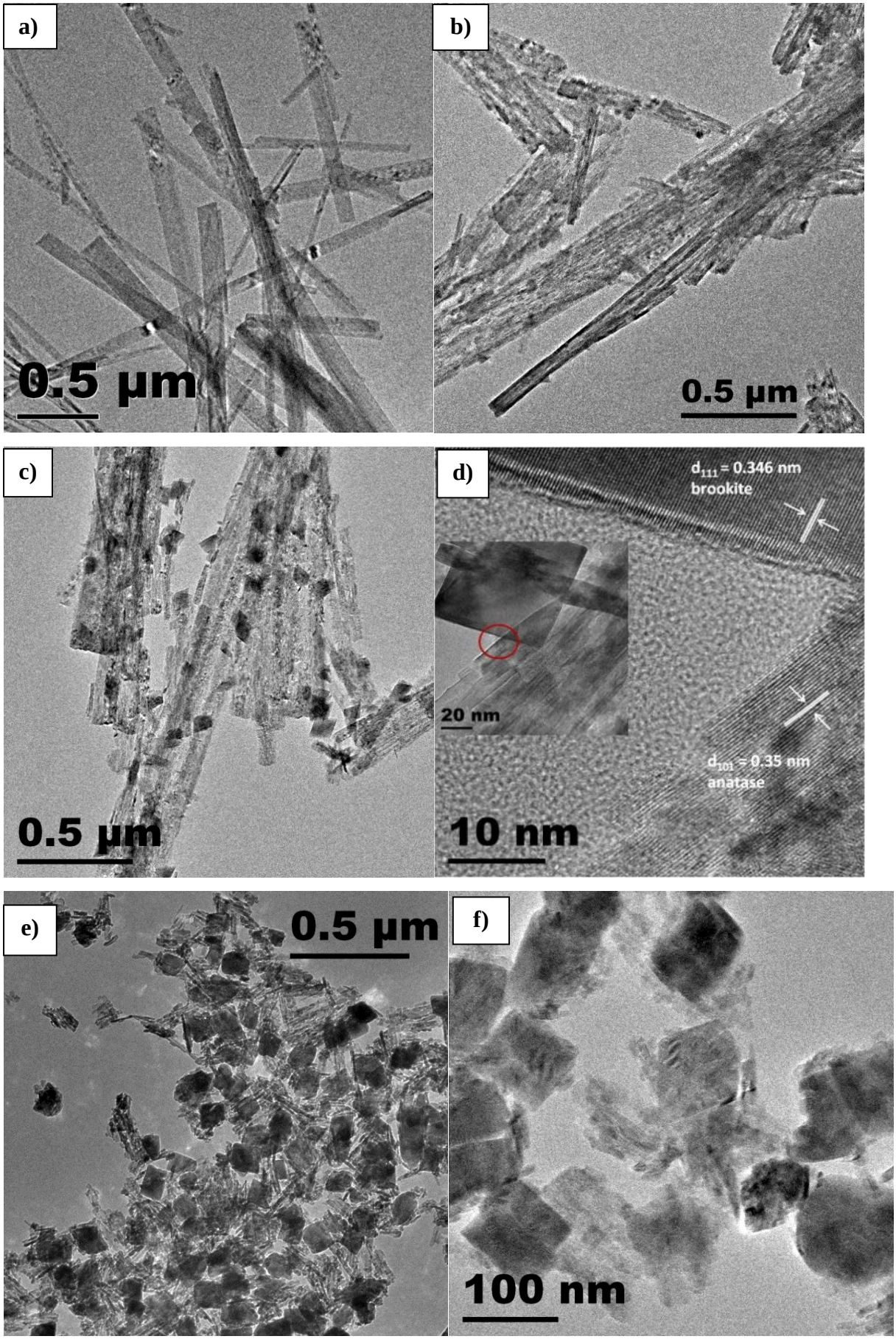
a)
0.5 µm
b)
0.5 µm
c)
0.5 µm
d)
d_{111} = 0.346 nm
brookite
20 nm
d_{101} = 0.35 nm
anatase
10 nm
e)
0.5 µm
f)
100 nm

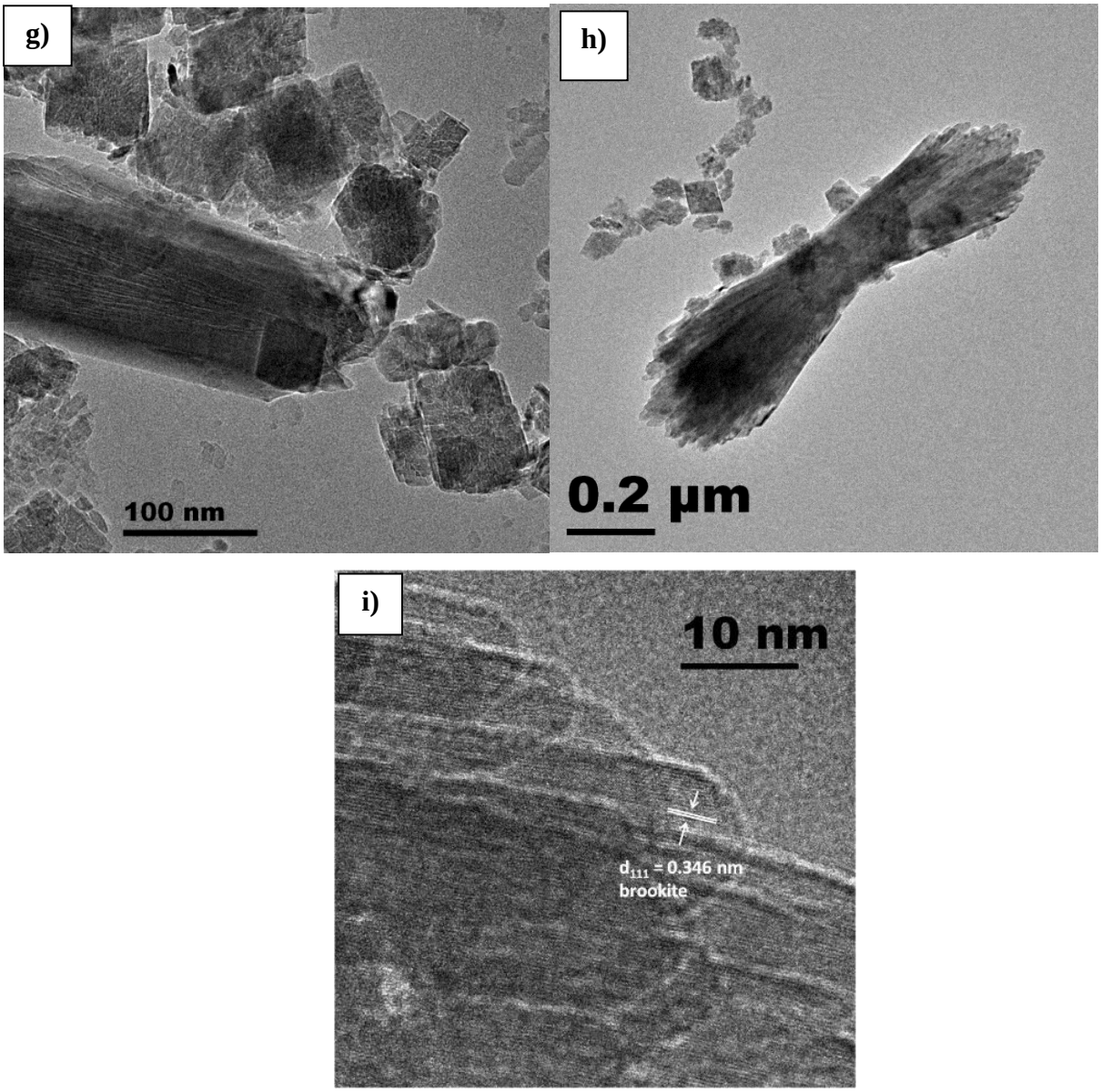

Figure 32 TEM images of *a)* as-prepared H-TNFs, *b)* HPT0.05, *c)* HPT0.1, *d)* HRTEM image of HPT0.1; taken from the area marked by red circle (inset) *e)* HPT0.5, *f)* HPT1, *g)* HPT2, and *h)* HPT4 TiO_2 products *i)* HRTEM of HPT4

Raman measurements showed a qualitative correspondence with the XRD results about the identity of composing crystal phases. *Figure 33* shows the Raman spectra of the HPT0.05 – 4 TiO_2 samples. The characteristic Raman bands of anatase at 144 (E_g), 198 (E_g), 397 (B_{1g}), 516 (A_{1g}, B_{1g}) and 639 cm^{-1} (E_g) were recognized in HPT0.05, confirming the presence of pure anatase phase in the sample. For HPT0.1, weak vibrational bands of brookite were also visible at 247 and 322 cm^{-1} besides anatase. When higher acid concentration was used ($\geq$ 0.5 mol/L), the sharp vibrational band at 144 cm^{-1} slightly shifted towards 153 cm^{-1}, representative for brookite.[26] Further vibrational peaks, assigned to brookite, were observed at 172, 214, 247, 288, 322, 366, 396, 454, 585 and at 636 cm^{-1} in

HPT0.5, HPT1, HPT2 and HPT4. Finally, in HPT1, HPT2 and HPT4 samples obtained at extreme low pH (below pH ~1.1), vibrational Raman modes for rutile were also found besides anatase and brookite with wide bands at 143, 235 and 320 cm^{-1} and sharp bands at 449 and 610 cm^{-1}.[26, 169]

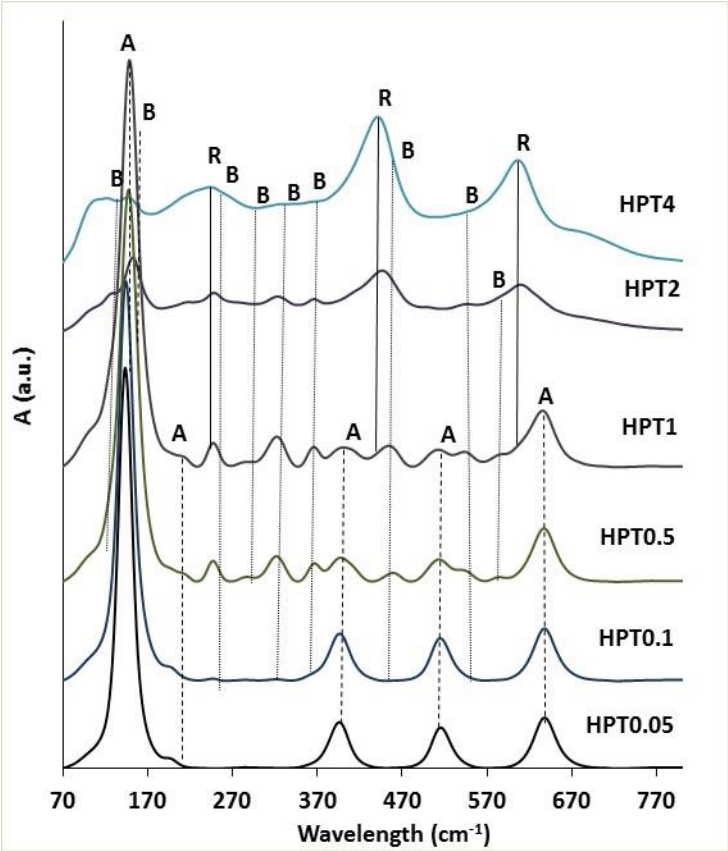

Figure 33 Raman spectra of HPT TiO_2 samples. A, B and R referring to the representative vibrations of anatase, brookite, rutile, respectively.

The textural properties of the TiO_2 samples were analysed using the N_2-sorption method. Specific surface area data were obtained using BET (Brunauer – Emmett–Teller) method. Volume and average diameter of pores were determined by BJH (Barrett –Joyner – Halenda) and the data are summarised in *Table 9*. The specific surface areas varied between 52.0 and 65.4 m^2/g without significant difference.

Table 9 BET surface areas of the prepared TiO_2 samples.

Nr	Sample ID	s^a_{BET} (m^2/g)	Vol. of pores (cm^3/g)[a]	Diameter of pores (Å)[b]

1	HPT0.05	65.4	0.32	203
2	HPT 0.1	62.2	0.30	191
3	HPT 0.5	64.5	0.42	245
4	HPT1	52.0	0.32	235
5	HPT2	52.6	0.20	136
6	HPT4	57.0	0.12	162

[a]*BJH Desorption Cummulative Volume of pores (17.000-3.000.000)*

[b]*BJH Desorption average pore diameter (4V/A)*

The calculated E_g values for HPT0.05 and HPT0.1 samples were 3.25 and 3.22 eV, respectively (*Table 10*). These values were close to the data reported in literature for anatase TiO_2 (3.2 eV). [30] For samples HPT0.5 to HPT4, the band gap energy was shifted towards slightly lower energy values owing to the increasing amount of rutile and brookite which are known to have lower band gap energies, 3.02 eV [170] and 3.12 eV [127], respectively.

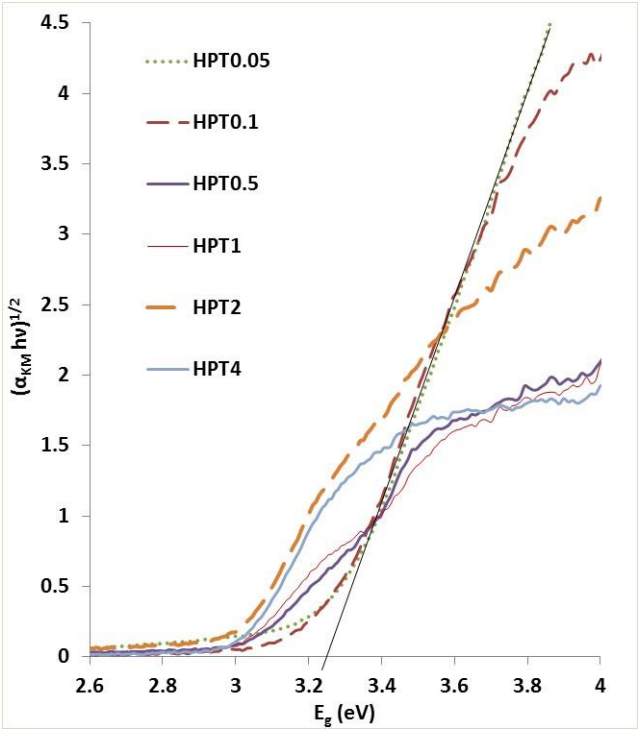

Figure 34 Figure 4 Kubelka-Munk plots of HPT samples

Table 10 Calculated band gap energies and corresponding wavelengths.

Nr	Sample ID	E*g* (eV)	λ (nm)
1	HPT0.05	3.25	381.5

2	HPT0.1	3.22	385.1
3	HPT0.5	3.05	406.6
4	HPT1	3.00	413.3
5	HPT2	2.98	416.1
6	HPT4	2.98	416.1

[a] $\lambda=1240/E_g$

In semiconductor photocatalysis, the rate of electron – hole generation is an important factor that fundamentally affects the photocatalytic activity. The generation of excitons (the separation mechanism) is essential, but not sufficient for the photocatalytic process to occur. Once the separation is successful, the charge carriers have to reach the surface of the semiconductor NPs where they can actively participate in the photocatalytic process by generating radicals or directly interacting with adjacent organic molecules. Often the case is that these charge carriers are trapped in bulk defects before reaching the surface of the NPs. PEC measurements, such as photo-voltammetry, are good preliminary indicators of the electronic mechanisms induced by light irradiation on the semiconductor. *Figure 35* compares linear sweep photovoltammetry data for selected TiO_2 samples (HPT0.05, HPT0.1 and HPT4 with identical film thickness).

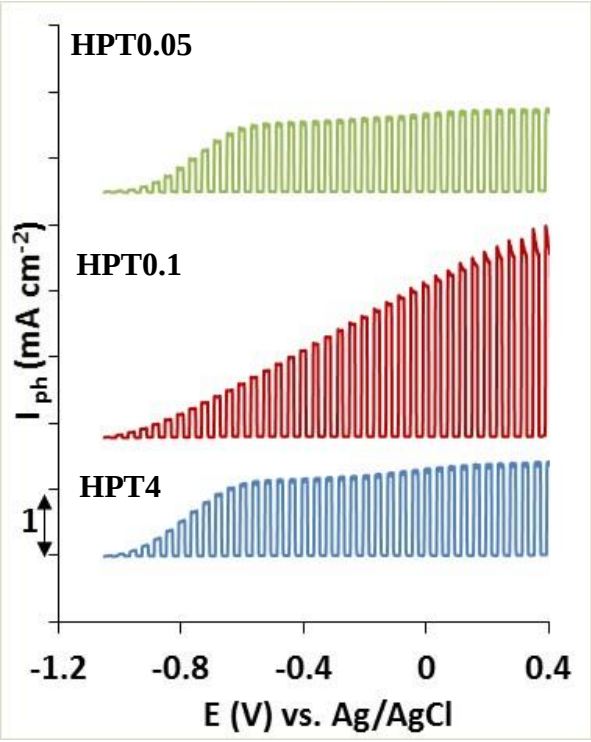

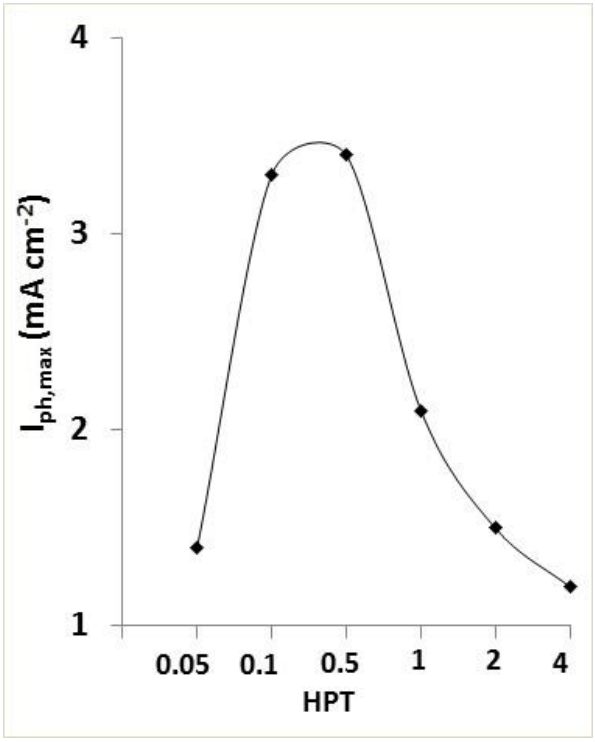

Figure 35 a). Representative photo-voltammograms of selected TiO_2 samples, recorded between -1.1 V and 0.5 V, in 0.1 M Na_2SO_3, at a sweep rate of 2 mV s^{-1} using a 300W Hg-Xe arc lamp. *b)* Comparison of the maximum photocurrent values obtained for the various TiO_2 samples.

This voltammetry technique had been described elsewhere in more details.[171] Briefly, slow scan of the potential was recorded while the irradiation of the film was periodically interrupted. In this manner, both the ‘‘dark’’ and the light-induced photoresponse of the samples could be assessed in a single experiment. As it can be seen in *Figure 35 a),* the photocurrents are anodic in polarity for all the samples, consistent with the n-type semiconductor behaviour of the different TiO_2 phases. The photocurrents arose mainly from the photo-oxidation of the electrolyte ions, which were the hole-scavengers (electron donors). The overall shape of the voltammograms was similar and all of them had the same onset potential. On the other hand, the magnitude of the photocurrent was notably different for the various samples. A careful comparison of the photocurrent values, detected in the plateau region, revealed an important information on the PEC properties. As shown in *Figure 35 b),* a volcano-type curve is obtained, which shows that the highest currents are obtained for samples HPT0.1 and HPT0.5. It is particularly interesting to correlate the maximum photocurrent values with the compositional/morphological features (as shown by XRD, Raman spectroscopy, and TEM) of the samples. The compositional change in the series of samples was reflected in the PEC behaviour. Initially, a sharp increase was observed in the photocurrents with the appearance of the brookite phase (HPT0.1 and HPT0.5). Subsequently, the photocurrent decreased with the gradual increase of the rutile component, as a large amount of rutile could become a barrier for electron transport **172**. These observations can be rationalized with the significant difference in the conductivities of the three phases (brookite > anatase > rutile).[173]

Finally, consecutive photovoltammetric scans were conducted in a wider potential window (i.e., up to E=1.5 V vs. Ag/AgCl) using Na_2SO_4 as electrolyte to avoid dark electrooxidation of sulphite ions (*Figure 36).* In these experiments there was no hole-scavenger used in the solution; therefore, the photogenerated charge carriers stayed longer on the photoanode. These studies reveal significant differences in the stability of the various samples which was reflected by a decrease of the photocurrents in the series of voltammetric scans (as deduced from the plateau-current values). It was found that the rhomboid-shaped brookite-rich samples (HPT0.5; HPT1 and HPT2) showed a decay of the photocurrents already during the second cycle, whereas the anatase- or the rutile-rich samples showed a notable stability. These results highlight the importance of structure and morphology on the PEC properties: the rhomboid-shaped brookite-rich NPs were found to generate high photocurrents,

but showed low stability of the photoresponse; whereas the elongated anatase- and rutile-rich samples had higher stability than the brookite-rich, rhomboid NPs.

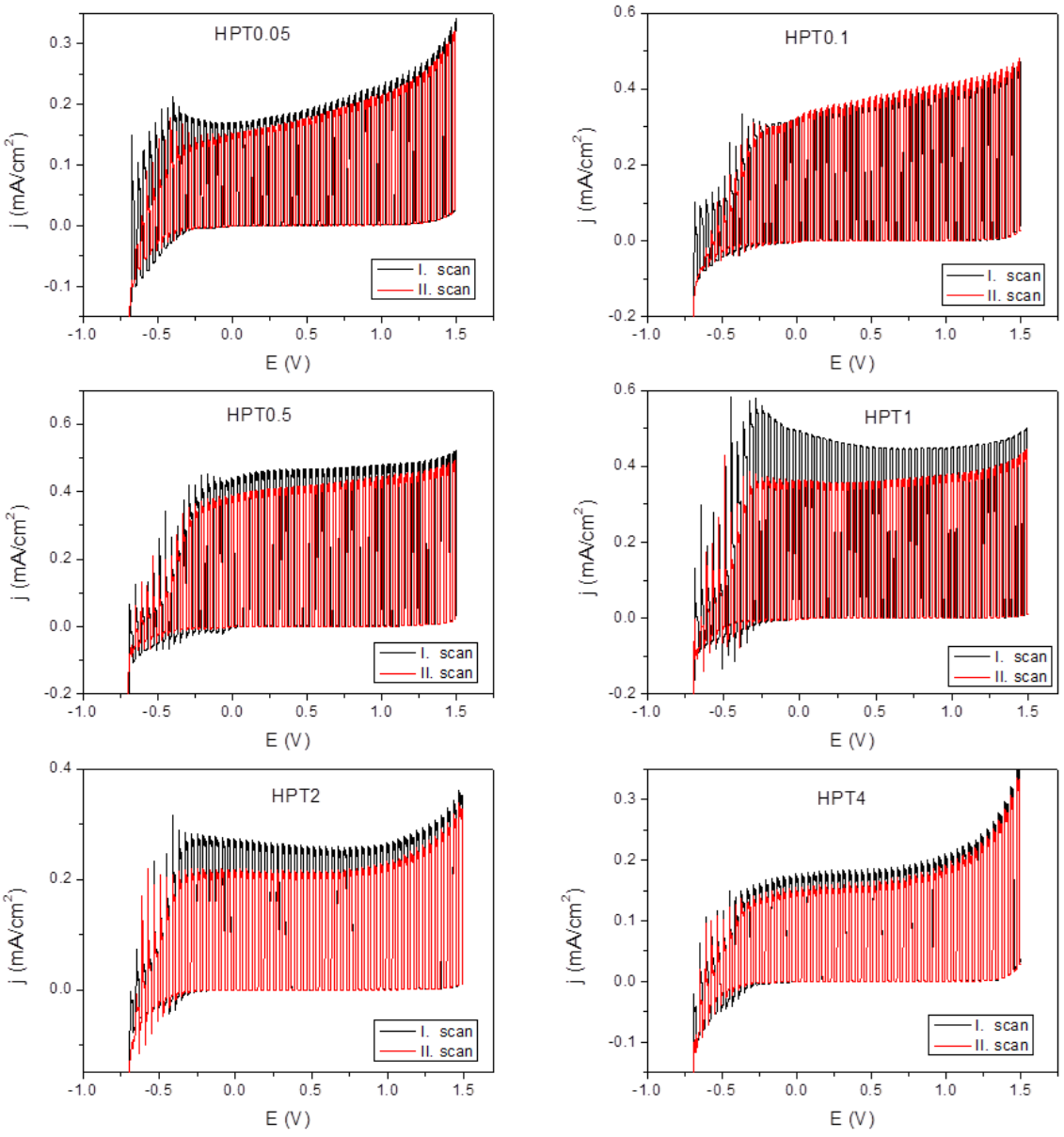

Figure 36 Repeated photovoltammetric scans of TiO_2 samples. The scans were recorded between -0.7 V and 1.5 V, in 0.1 M Na_2SO_4, at a sweep rate of 2 mV s^{-1} under irradiation with a 300W Hg-Xe arc lamp.

5.3.2. Evaluation of photocatalytic activity

Comparing the photocatalytic and reaction rates, normalised for BET surface area, it was found that HPT0.1, the sample containing dominant anatase (93.2%) and small amount of brookite (6.8%), displayed the highest photocatalytic activity. The second most active catalyst was HPT0.05 containing

pure anatase nanofibers. It was followed by the tri-crystalline (anatase, brookite and with a minor rutile phase with 49.2 %; 47.7% and 3.05%, respectively) rhomboid shaped TiO_2 NPs. Furthermore, with the increasing of the rutile-content, the photocatalytic activity was decreased, accordingly. The photocatalytic test data are summarised below in *Table 11*.

Table 11 Summary of data on the photocatalytic degradation of EtOH on HPT TiO_2 samples

Nr	Sample ID	Conversion (%)	*k* (min)	R^2	k/a^s_{BET} (g/ min /m^2) x 10^{-4}	Δm_{EtOH} (mg)	Δm_{EtOH} (mg /g kat)	Δm_{ETOH} (μg/cm^2)
1	HPT0.05	76.62	0.0502	0.9701	7.68	1.62	28.94	36.01
2	HPT0.1	99.60	0.0530	0.9770	8.52	1.78	31.79	39.57
3	HPT0.5	98.51	0.0372	0.9645	5.77	1.93	34.45	42.87
4	HPT1	95.09	0.0247	0.9638	4.75	1.85	32.98	41.04
5	HPT2	97.48	0.0217	0.9930	4.17	2.05	36.63	45.59
6	HPT4	76.62	0.0105	0.9830	1.84	1.89	33.72	41.96

The results are reasonable, if we consider that this sample was very rich in anatase and it has an elongated structure, also it has a bi-crystalline structure, containing only a small amount of brookite. These properties all seem to contribute to better photocatalytic efficiencies. The above observations show good correlation with the photoelectrochemical photoelectrochemical properties of the different TiO_2 samples. The reason why HPT0.1 seems to exhibit enhanced photoelectrochemical properties is because of two factors. First, it is able to generate high photocurrents and second, the generated photocurrent values could be maintained for an extended time of irradiation. These properties are related to the advantageous structural features of this sample including the anatase-brookite bi-crystalline nature and the elongated morphology. The reason for the slightly lower photocatalytic activity of the pure anatase nanofibres (HPT0.05) should also be attributed to the absence of the bi-crystalline structure, which resulted in higher rate of recombination that accordingly led to smaller photocurrents. As for the rutile-rich samples, the generated photocurrents were very low, as rutile is not a very good conductor and it is rather difficult for the charge carriers to move in the structure.

Therefore, it is not a surprise that the rutile-rich samples showed low photocatalytic activity; In spite of the fact that rutile displayed a fairly stable photoelectrochemical response, it had low ability to generate photocurrents which had a detrimental effect on the photocatalytic activity. Clearly, these findings show how the structure influences and determines the photoelectrochemical and photocatalytic properties, and explains why HPT0.1 is the most active TiO_2 photocatalyst among those presented in this work.

5.5. Photoreactor for indoor air purification

Most reported TVOC (Total VOC) concentrations in non-industrial indoor environments are below $1 \cdot 10^{-3}$ mg/L and few exceed $25 \cdot 10^{-3}$ mg/L according to a study conducted by the European Commission Joint Research Centre in 1997.[174] Headaches and discomfort can be realised at TVOC concentration from $22 \cdot 10^{-3}$ mg/L, e.g. in new or renovated buildings.[175,176] A photoreactor was built to be the functional part of an indoor air cleaning device (*Figure 37*). 18 LED light sources, emitting in the Vis range (λ_{max} = 405 nm), were built in the photo-reactor with a total electric power consumption of 25 W/h. The EtOH vapour was circulated by a built-in fan. The initial EtOH concentration was 2.92 mg/L in a closed vessel (V = 16.18 L). Note that this concentration is more than 3 magnitude higher than the TVOC concentration in and average indoor area. Ag-TiO_2/p(EA-co-MMA) nanocomposite film (70wt%/30wt%) was evenly coated on both sides of a removable cylinder with a total surface area (A) of 880 cm^2. The cylinder with the catalyst coating was irradiated by the LEDs from both sides. Prior to the photocatalytic tests, the coating was irradiated for 20 hrs to be "pre-activated", which was followed by three consecutive photocatalytic runs. After the third run, the UV-treatment was repeated, followed by three consecutive runs again.

It was observed that the conversion of EtOH decrease from 89.1% to 64.0% by the end of the third run which is presumably due to deactivation of the photocatalyst by adsorbed intermediate products (*Table 12*). However, the UV-treatment was found to be very efficient to re-activate the nanocomposite layer, and even to slightly increase the photocatalytic activity, which might be owing to the fact that new layers of photocatalyst NPs were uncovered.

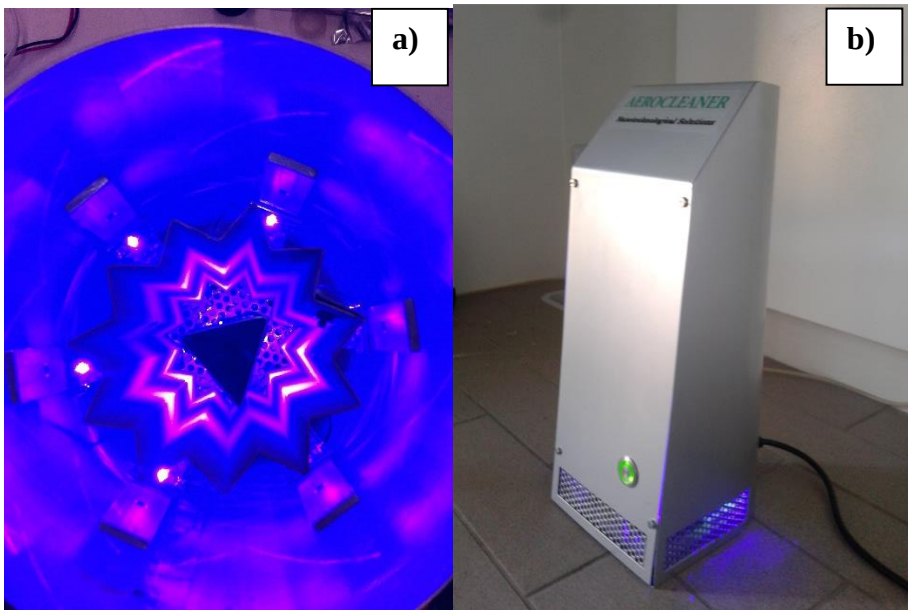

Figure 37 Photographs of the constructed air purification device: a) under operation (EtOH degradation test) under a closed glass vessel from top view b) and covered in reactor jacket

Table 12 Summary of data on the photocatalytic degradation of EtOH in the air cleaning device

No. Photocatalytic run	Conversion $_{EtOH}$ (%)	k (1/min)	R^2	Δm_{EtOH} (mg)	Δm_{EtOH} (mg /g kat)	Δm_{ETOH} ($\mu g/cm^2$)
Cycle 1						
1/1	89.1	0.0285	1.0000	28.40	36.88	32.27
1/2	76.4	0.0186	0.9835	25.59	33.23	29.08
1/3	64.0	0.0129	0.9831	22.48	29.19	25.54
Cycle 2						
2/1	96.3	0.0372	0.9873	25.63	33.29	29.12
2/2	87.3	0.0254	0.9885	25.51	33.12	28.98
2/3	68.2	0.0158	0.9853	21.86	28.39	24.84

6. References

1 C. Mccullagh, J. M.C. Robertson, D. W. Bahnemann, P. K. J. Robertson;The application of TiO_2 photocatalysis for disinfection of water contaminated with pathogenic micro-organisms: a review; *Res. Chem. Intermed*. 33 (2007) 359–375.

2 M. Ni, M. K. H. Leung, D. Y. C. Leung, K. Sumathy; A review and recent developments in photocatalytic water-splitting using TiO_2 for hydrogen production; *Renew. Sust. Energ. Rev*. 11 (2007) 401–425.

3 J. C. Colmenares, R. Luque; Heterogeneous photocatalytic nanomaterials: prospects and challenges in selective transformations of biomass-derived compounds; *Chem. Soc. Rev.* 43 (2014) 765–778.

4 S. N. Habisreutinger, L. Schmidt-Mende, J. K. Stolarczyk; Photocatalytic reduction of CO_2 on TiO_2 and other semiconductors; *Angew. Chem. Int. Ed.* 52 (2013) 2–39.

5 F. Solymosi, I. Tombácz; Photocatalytic reaction of H_2O+CO_2 over pure and doped Rh/TiO_2; *Cat. Lett.* 27 (1994) 61–65.

6 G. J. Meyer; Efficient light-to-electrical energy conversion: Nanocrystalline TiO_2 films modified with inorganic sensitizers; *J. Chem. Educ.* 74 (1997) 652.

7 S. P. Tallósy, L. Janovák, J. Ménesi, E-. Nagy, Á. Juhász, L. Balázs, I. Deme, N. Buzás, I. Dékány; Investigation of the antibacterial effects of silver-modified TiO_2 and ZnO plasmonic photocatalysts embedded in polymer thin films; *Environ. Sci. Pollut. Res. Int.* 21 (2014) 11155–11167.

8 S. P. Tallósy, L. Janovák, J. Ménesi, E. Nagy, Á. Juhász, I. Dékány; LED-light activated antibacterial surfaces using silver-modified TiO_2 embedded in polymer matrix; *J. Adv. Oxid. Technol.* 17 (2014) 9–16.

9 Y. Lai, Y. Tang, J. Gong, D. Gong, L. Chi, C. Lin, Z. Chen; Transparent superhydrophobic/superhydrophilic TiO_2-based coatings for self-cleaning and anti-fogging; *J. Mater. Chem.* 22 (2012) 7420–7426.

10 M. Faustini, L. Nicole, C. Boissière, P. Innocenzi, C. Sanchez, D. Grosso; Hydrophobic, antireflective, self-cleaning, and antifogging sol−gel coatings: An example of multifunctional nanostructured materials for photovoltaic cells; *Chem. Mater.*22 (2010) 4406–4413.

11 I. Arslan, I. A. Balcioglu, T. Tuhkanen, D. Bahnemann; H_2O_2/UV-C and Fe^{2+}/H_2O/UV-C versus TiO_2/UV-A treatment for reactive dye wastewater, *J. Environ. Eng.* 126 (2000) 903–911.

12 T. Alapi, K. Gajda-Schrantz, I. Ilisz,K. Mogyorósi,P. Sipos, A. Dombi; Comparison of UV- and UV/VUV-induced photolytic and heterogeneous photocatalytic degradation of phenol, with particular emphasis on the intermediates *J. Adv. Oxid. Technol.*, 11 (2008) 519–528.

13 S. Malato, J. Blanco, J. Cáceres, A.R. Fernández-Alba, A. Agüera, A. Rodríguez; Photocatalytic treatment of water-soluble pesticides by photo-Fenton and TiO_2 using solar energy; *Cat. Tod.* 76 (2002) 209–220.

14 E. Illés, E. Takács, A. Dombi, K. Gajda-Schrantz, G. Rácz, K. Gonter, L. Wojnárovits; Hydroxyl radical induced degradation of ibuprofen*; Sci.Total Environ.* 447 (2013) 286–292.

15 M. N. Chong, B. Jin, C. W. K. Chow, C. Saint; Recent developments in photocatalytic water treatment technology: A review; *Water Res.* 44 (2010) 2997–3027.

16 B. Ohtani; Photocatalysis A to Z—What we know and what we do not know in a scientific sense; *J. Photochem. Photobiol.* 11 (2010) 157–178.

17 K. Rajeshwar, A. Thomas; C. Janáky; Photocatalytic activity of inorganic semiconductor surfaces: Myths, hype, and reality; *J. Phys. Chem. Lett.* 6 (2015) 139−147.

18 A. Mills, S. Le Hunte; An overview of semiconductor photocatalysis; *J. Photochem. Photobiol. A* 108 (1997) 1–35.

19 A. Fujishima, K. Honda; Electrochemical photolysis of water at a semiconductor electrode; *Nature* 238 (1972) 37–38.

20 S. N. Frank, A. J. Bard; Heterogeneous photocatalytic oxidation of cyanide ion in aqueous solutions at TiO_2 powder; *J. Am. Chem. Soc.* 99 (1977) 303–304.

21 S. N. Habisreutinger, L. Schmidt-Mende, J. K. Stolarczyk; Photocatalytic reduction of CO_2 on TiO_2 and other semiconductors; *Angew. Chem. Int. Ed*. 52 (2013) 2–39.

22 M. D. Hernández-Alonso, F. Fresno, S. Suáreza, J. M. Coronado; Development of alternative photocatalysts to TiO_2: Challenges and opportunities; *Energy Environ. Sci.* 2 (2009) 1231–1257.

23 LinsebieglerCHEMREV95 A. L. Linsebigler, G. Lu, J. T. Yates, Jr; Photocatalysis on TiO_n surfaces: principles, mechanisms, and selected results; *Chem. Rev*. 95 (1995) 735–758.

24 A. Fujishima, T. N. Rao, D. A. Try; Titanium dioxide photocatalysis; *J. Photochem. Photobiol. C* 1 (2000) 1–21.

25 Kaneko and I. Okura, in Photocatalysis, Science and Technology, ed. M Kaneko, I. Okura, Kodansha Spinger, Tokyo, 2002, ch 3.2, p 30.

26 A. D. Paola, M. Bellardita, L. Palmisano; Brookite, the least known TiO_2 Photocatalyst; *Catalysts* 3 (2013) 36–73.

27 K. Momma and F. Izumi; *VESTA 3* for three-dimensional visualization of crystal, volumetric and morphology data; *J. Appl. Cryst.* 44 (2011) 1272–1276.

28 M. A. Fox, M. T. Dulay; Heterogenous photocatalysis, *Chem. Rev.* 93 (1993) 341–357.

29 J. Augustynski; The role of the surface intermediates in the photoelectrochemical behaviour of anatase and rutile TiO_2; *Electrochimia Acta* 38 (1993) 43–46.

30 A. Scalfani, J. M. Hermann; Comparison of the photoelectronic and photocatalytic activities of various anatase and rutile forms of titania in pure liquid organic phases and in aqueous solutions; *J. Phys. Chem.* 100 (1996) 13655–13661.

31 T. Luttrell, S. Halpegamage, J. Tao, A. Kramer, E. Sutter, M. Batzill; Why is anatase a better photocatalyst than rutile? - Model studies on epitaxial TiO_2 films; *Sci. Rep.* 4 (2014) 4043–4051.

32 J. Zhang, P. Zhou, J. Liu, J. Yu; New understanding of the difference of photocatalytic activity among anatase, rutile and brookite TiO_2; *Phys.Chem.Chem.Phys.*16 (2014) 20382–20386.

33 Q. Tay, X. Liu, Y. Tang, Z. Jiang, T. C. Sum, Z. Chen; Enhanced photocatalytic hydrogen production with synergistic two-phase anatase/brookite TiO_2 nanostructures; *J. Phys. Chem. C* 117 (2013) 14973−14982.

34 H. Zhao, L. Liu, J. M. Andino, Y. Li; Bicrystalline TiO_2 with controllable anatase–brookite phase content for enhanced CO_2 photoreduction to fuels; *Mater. Chem. A* (2013) 1 8209–8216.

35 S. Rasalingam, C-M. Wu, R. T. Koodali; Modulation of pore sizes of titanium dioxide photocatalysts by a facile template free hydrothermal synthesis method: Implications for photocatalytic degradation of Rhodamine B; *J. Am. Chem. Soc. Appl. Mater. Int.* 7 (2015) 4368–4380.

36 N. Balázs, K. Mogyorósi, D. F. Srankó, A. Pallagi, T. Alapi, A. Oszkó, A. Dombi, P. Sipos; The effect of particle shape on the activity of nanocrystalline TiO_2 photocatalysts in phenol decomposition; *Appl. Catal.B* 84 (2008) 356–362.

37 N. Balázs, D. F. Srankó, A. Dombi, P. Sipos, K. Mogyorósi; The effect of particle shape on the activity of nanocrystalline TiO_2 photocatalysts in phenol decomposition. Part 2: The key synthesis parameters influencing the particle shape and activity; *Appl. Catal. B* 96 (2010) 569–576.

38 U. Diebold, The surface science of titanium dioxide; *Surf. Sci. Rep.* 48 (2003) 53–229.

39 T. R. Gordon, M. Cargnello, T. Paik, F. Mangolini, R. T. Weber, P. Fornasiero, C. B. Murray; Nonaqueous synthesis of TiO_2 nanocrystals using TiF_4 to engineer morphology, oxygen vacancy concentration and photocatalytic activity; *J. Am. Chem. Soc.* 134 (2012) 6751−6761.

40 N. Wu, J. Wang, D. N. Tafen, H. Wang, J-G. Zheng, J. P. Lewis, X. Liu, S. S. Leonard, A. Manivannan; Shape-enhanced photocatalytic activity of single-crystalline Anatase TiO_2 (101) nanobelts; *J. Am. Chem. Soc.*132 (2010) 6679–6685.

41 A. Testino, I. R. Bellobono, V. Buscaglia, C. Canevali, M. D'Arienzo, S. Polizzi, R. Scotti, F. Morazzoni; Optimizing the photocatalytic properties of hydrothermal TiO_2 by the control of phase composition and particle morphology. A systematic approach; *J. Am. Chem. Soc.* 129 (2007) 3564–3575.

42 K. Mogyorósi, N. Balázs, D.F. Srankó, E. Tombácz, I. Dékány, A. Oszkó, P. Sipos, A. Dombi; The effect of particle shape on the activity of nanocrystalline TiO_2 photocatalysts in phenol decomposition. Part 3: The importance of surface quality*; Appl.Catal. B* 96 (2010) 577–585.

43 K. Pirkanniemi, M. Sillanpää; Heterogeneous water phase catalysis as an environmental application: a review; *Chemosphere* 48 (2002) 1047–1060.

44 Composite Titanium Dioxide Photocatalysts and the "Adsorb & Shuttle" Approach: A Review; *Solid State Phenomena* 162 (2010) 135–162.

45 J. Matosa, J. Laine, J-M. Herrmann Synergy effect in the photocatalytic degradation of phenol on a suspended mixture of titania and activated carbon; *App. Catal. B* 18 (1998) 281–291.

46 J-M. Herrmann, J. Matos, J. Disdier, C. Guillard, J. Laine, S. Malato, J. Blanco; Solar photocatalytic degradation of 4-chlorophenol using the synergistic effect between titania and activated carbon in aqueous suspension; *Catal. Today* 54 (1999) 255–265.

47 SachtlerAdvCat1993 W. M. H. Sachtler, Z. Zhang; Zeolite-Supported Transition Metal Catalysts; *Adv. Catal.* 39 (1993) 129–220.

48 S. Sampath, H. Uchida, H. Yoneyama, Photocatalytic degradation of gaseous pyridine over zeolite supported titanium dioxide; *J. Catal.* 149 (1994) 189–194.

49 N. Nagaraju, A. Fonseca, Z. Konya, J.B. Nagy; Alumina and silica supported metal catalysts for the production of carbon nanotubes; *J. Mol. Catal. A* 181 (2002) 57–62.

50 K. V. S. Rao, M. Subrahmanyam, P. Boule; Immobilized TiO_2 photocatalyst during long-term use: decrease of its activity; *Appl. Catal. B* 49 (2004) 239–249.

51 T. Pernyészi, Á. Patzkó, O. Berkesi, I. Dékány; Asphaltene adsorption on clays and crude oil reservoir rocks; *Coll. Surf. A* 137 (1998) 373–384.

52 G. Lagaly, I. Dékány; Adsorption on hydrophobized surfaces: Clusters and self-organisation; *Adv. Coll. Int. Sci.* 114-115 (2005) 189–204.

53 I. Dékány, L. Turi, A. Szücs, Z. Király; Preparation of semiconductor on colloidal solid supports; *Coll. Surf. A* 141 (1998) 405–417.

54 R. Kun, M. Szekeres, I. Dékány; Photooxidation of dichloroacetic acid controlled by pH-stat technique using TiO_2/layer silicate nanocomposites; *Appl. Catal. B* 68 (2006) 49–58.

55 Robert Kun, K. Mogyorósi, I. Dékány; Synthesis and structural and photocatalytic properties of TiO_2/montmorillonite nanocomposites; *Appl. Clay Sci.* 32 (2006) 99–110.

56 I. Ilisz, A. Dombi, K. Mogyorósi, I. Dékány; Photocatalytic water treatment with different TiO_2 nanoparticles and hydrophilic/hydrophobic layer silicate adsorbents; *Coll. Surf. A* 230 (2003) 89–97.

57 P. Aranda, R. Kun, M. A. Martín-Luengo, S. Letaïef, I. Dékány, E. Ruiz-Hitzky; Titania-Sepiolite Nanocomposites Prepared by a Surfactant Templating Colloidal Route; *Chem. Mater.* 20 (2008) 84–91.

58 J. Ménesi, L. Kőrösi, É. Bazsó, V. Zöllmer, A. Richardt, I. Dékány; Photocatalytic oxidation of organic pollutants on titania-clay composites; *Chemosphere* 70 (2008) 538–542.

59 L. Kőrösi, J. Németh, I. Dékány; Structural and photooxidation properties of SnO_2/layer silicate nanocomposites; *Appl. Clay Sci.* 27 (2004) 29 – 40.

60 T. Pernyészi, I. Dékány; Photocatalytic degradation of hydrocarbons by bentonite and TiO_2 in aqueous suspensions containing surfactants; *Coll. Surf. A* 230 (2003) 191–199.

61 G. L. Haller, D. E. Resasco; Metal–support interaction: Group VIII metals and reducible oxides; *Adv. Catal.* 36 (1989) 173–235.

62 E. Kikuchi, M. Matsumoto, T. Takahashi, A. Machino, Y. Morita; Fischer-Tropsch synthesis over titania-supported ruthenium catalysts; *Appl. Cat.* 10 (1984) 251–260.

63 F. Solymosi, I. Tombácz, M. Kocsis, Hydrogenation of CO on supported Rh catalyst; *J. Catal.* 75 (1982) 78–93.

64 E. B. Maxted, S. I. Ali; The role of supports in catalytic hydrogenation. Part I. Activation effects of various oxide carriers on palladium; *J. Am. Chem. Soc.* (1961) 4137–4140.

65 YatesJACS 1964 D. J. C. Yates, W. F. Taylor, J. H. Sinfel;, Catalysis over supported metals. I. Kinetics of ethane hydrogenolysis over nickel surfaces of known Area; *J. Am. Chem. Soc.*86 (1964) 2996–3031.

66 F. Solymosi, Importance of the electric properties of supports in the carrier effect; *Cat. Rev*. 1 (1968) 233–255.

67 Y. H. Ng, I. V. Lightcap, K. Goodwin, M. Matsumura, P.V. Kamat; To what extent do graphene scaffolds improve the photovoltaic and photocatalytic response of TiO_2 nanostructured films?; *J. Phys. Chem. Lett.* 1 (2010) 2222–2227.

68 T. Szabó, E. Tombácz , E. Illés, I. Dékány, Enhanced acidity and pH-dependent surface charge characterization of successively oxidized graphite oxides; *Carbon* 44 (2006) 537–545.

69 V. Štengl, S. Bakardjieva, T. M. Grygar, J. Bludská, M. Kormunda; TiO_2-graphene oxide nanocomposite as advanced photocatalytic materials; *Chem. Centr. J.* 7 (2013) 41–53.

70 W. Yan, F. He, S. Gai, P. Gao, Y. Chen, P. Yang; A novel 3D structured reduced graphene oxide/TiO_2 composite: synthesis and photocatalytic performance; *J. Mater. Chem. A* 2 (2014) 3605-3612.

71 L-L. Tan, W-J. Ong, S-P Chai, A. R. Mohamed; Reduced graphene oxide-TiO_2 nanocomposite as a promising visible-light-active photocatalyst for the conversion of carbon dioxide; *Nanoscale Res. Lett.* 8 (2013) 465 – 474.

72 H. Gao, X. Li, J. Lv, G. Liu; The interfacial charge transfer and enhanced photocatalytic mechanisms for the hybrid graphene/anatase TiO_2 (001) Nanocomposites; *J. Phys. Chem. C* 11 (2013) 16022–16027.

73 E. Yousif, R. Haddad; Photodegradation and photostabilization of polymers, especially polystyrene: review; *Springer Plus* 2 (2013) 398–430.

74 X.Z**.** Li, Y.G. Zhao; Advanced treatment of dyeing wastewater for reuse; *Water Sci. Technol.* 39 (1999) 249–255.

75 Xi W, Geisen SV. Separation of titanium dioxide from photocatalytically treated water by cross-flow filtration; *Water Res.* 35 (2001)1256–1262.

76 P. Fernández-Ibáñez, J. Blanco, S. Malato, F.J. de las Nieves; Application of the colloidal stability of TiO_2 particles for recovery and reuse in solar photocatalysis; *Water Res.* 37 (2003) 3180–3188.

77 Y. Liu, L. Yu, Y. Hu, C. G. F. Zhang, X. W. (D.) Lou; A magnetically separable photocatalyst based on nest-like g-Fe_2O_3/ZnO double-shelled hollow structures with enhanced photocatalytic activity; *Nanoscale* 4 (2012) 183–187.

78 Y. S. Chung, S. B. Park, D-W. Kang; Magnetically separable titania-coated nickel ferrite photocatalyst; *Mater. Chem. Phys.* 86 (2004) 375–381.

79 Y. Ao, J. Xu, D. Fu, X. Shen, C. Yuan; A novel magnetically separable composite photocatalyst: Titania-coated magnetic activated carbon; *Separation Purif. Technol.* 61 (2008) 436–441.

80 S. Xuan, W. Jiang, X. Gong, Y. Hu, Z. Chen; Magnetically separable Fe_3O_4/TiO_2 hollow spheres: Fabrication and photocatalytic activity; *J. Phys. Chem. C* 13 (2009) 553–558.

81 M. Pelaez, Nicholas T. Nolan, S. C. Pillai, M. K. Seery, P. Falaras, A. G. Kontos, P. S.M. Dunlop, J. W.J. Hamilton, J. A. Byrne, K. O'Shea, .M. H. Entezari, D. D. Dionysiou; A review on the visible light active titanium dioxide photocatalysts for environmental applications; *Appl. Catal. B* 125 (2012) 331– 349.

82 S. G. Kumar, L. G. Devi; Review on modified TiO_2 photocatalysis under UV/Visible light: Selected results and related mechanisms on interfacial charge carrier transfer dynamics; *J. Phys. Chem. A* 115 (2011) 13211–13241.

83 É. G. Bajnóczi, N. Balázs, K. Mogyorósi, D. F. Srankó, Z. Papp, Z. Ambrus, S. E. Canton, K. Norén, E. Kuzmann, A. Vértes, Z. Homonnay, A. Oszkó, I. Pálinkó, P. Sipos; The influence of the local structure of Fe(III) on the photocatalytic activity of doped TiO_2 photoctatalysts – An EXAFS, XPS and Mössbauer spectroscopic study; *Appl. Cat. B* 103 (2011) 232–239.

84 Z. Ambrus, N. Balázs, T. Alapi, G. Wittmann, P. Sipos, A. Dombi, K. Mogyorósi; Synthesis, structure and photocatalytic properties of Fe(III)-doped TiO_2 prepared from $TiCl_3$; *Appl. Catal.* 81 (2008) 27–37.

85 Z. Liu, J. Y., Lei E, Y. Xin, W. Zhao; Effect of V doping on the band-gap reduction of porous TiO_2 films prepared by sol–gel route; *Mat. Chem. Phys* 120 (2010) 277–281.

86 R. Kun, S. Tarján, A. Oszkó, T. Seemann, V. Zöllmer, M. Busse , I. Dékány; Preparation and characterization of mesoporous N-doped and sulphuric acid treated anatase TiO_2 catalysts and their photocatalytic activity under UV and Vis illumination; *J. Solid State Chem.* 182 (2009) 3076–3084.

87 G. Veréb, Z. Ambrus, Z. Pap, Á. Kmetykó, A. Dombi, V. Danciu, A. Cheeseman, K. Mogyorósi, Comparative study on UV and visible light sensitive bare and diped titanium dioxide photocatalysts for the decomposition of environmental pollutants in water; *Appl. Cat. A* 29 (2012) 26–36.

88 R. Asahi; T. Morikawa, T. Ohwaki, K. Aoki, Y. Taga; Visible-light photocatalysis in nitrogen-doped titanium oxides; *Science* **2001**, *293*, 269–271.

89 Y. Cong, F. Chen,J. Zhang, M. Anpo, Carbon and nitrogen-codoped TiO_2 with high visible light photocatalytic activity; *Chem. Lett.* 35 (2006) 800–801.

90 C. Di Valentin, E. Finazzi, G. Pacchioni, A. Selloni, S. Livraghi, M. C. Paganini, E. Giamello; N-doped TiO_2: Theory and experiment; *Chem. Phys.* 339 (2007) 44–56.

91 S. Sakthivel, M. Janczarek, H. Kisch; Visible light activity and photoelectrochemical properties of nitrogen-doped TiO_2; *J. Phys. Chem. B* 108 (2004) 19384–19387.

92 Zs. Pap, L. Baia, K. Mogyorósi, A. Dombi, A. Oszkó, V. Danciu; Correlating the visible light photoactivity of N-doped TiO_2 with brookite particle size and bridged-nitro surface species; *Catal. Commun.* 17 (2012) 1–7.

93 Di Valentin, C.; Pacchioni, G.; Selloni, A.; Theory of carbon doping of titanium dioxide; *Chem. Mater*. 17 (2005) 6656–6665.

94 T. Ohno, T. Tsubota, M. Toyofuku, R. Inaba, Photocatalytic activity of a TiO_2 photocatalyst doped with C^{4+} and S^{4+} ions having a rutile phase under visible light. *Catal. Lett.* 98 (2004) 255–258.

95 H. Irie, Y. Watanabe, K. Hashimoto; Carbon-doped Anatase TiO_2 Powders as a Visible-light Sensitive Photocatalyst; *Chem. Lett.* 32 (2003) 772–773.

96 D. Li, D.; Haneda, H.; Labhsetwar, N.K.; Hishita, S.; Ohashi, N. Visible-light-driven photocatalysis on fluorine-doped TiO_2 powders by the creation of surface oxygen vacancies; *Chem. Phys. Lett.* 401 (2005) 579–584.

97 J. C. Yu, J. Yu, W. Ho, Z. Jiang, L. Zhang; Effects of F- doping on the Photocatalytic Activity and Microstructures of Nanocrystalline TiO_2; *Chem. Mater.* 14 (2002) 3808–3816.

98 Z. Pei, L. Ding, H. Lin, S. Weng, Z. Zheng, Y. Hou, P. Liu; Facile synthesis of defect-mediated TiO_{2-x} with enhanced visible light photocatalytic activity; *J. Mater. Chem. A* 1 (2013) 10099–10102.

99 M. Grätzel; Dye-sensitized solar cells; *J. Photochem. Photobiol. C* 4 (2003) 145–153.

100 Q. Xiang, J. Yu, M. Jaroniec; Graphene-based semiconductor photocatalysts; *Chem. Soc. Rev.* 41 (2012) 782–796.

101 C. Clavero; Plasmon-induced hot-electron generation at nanoparticle/metal-oxide interfaces for photovoltaic and photocatalytic devices; *Nature Photonics* 8 (2014) 95–103.

102 Y-C. Pu, G. Wang, K-D. Chang, Y. Ling, Y-K. Lin, B. C. Fitzmorris, C-M. Liu, X. Lu, Y. Tong, J. Z. Zhang, Y-J. Hsu, Y. Li, Au nanostructure-decorated TiO_2 nanowires exhibiting photoactivity across entire UV-visible region for photoelectrochemical water splitting; *Nano Lett.* 13 (2013) 3817−3823.

103 W. R. Erwin, A. Coppola, H. F. Zarick, P. Arora, K. J. Miller, R. Bardhan; Plasmon enhanced water splitting mediated by hybrid bimetallic Au–Ag core–shell nanostructures; *Nanoscale* 6 (2014) 12626–12634.

104 B. D Mankidy, B. Joseph,V. K Gupta, Photo-conversion of CO_2 using titanium dioxide: enhancements by plasmonic and co-catalytic nanoparticles; *Nanotechnol.* 24 (2013) 405402 – 405410.

105 Z. W. Seh, S. Liu , M. Low , S-Y. Zhang, Z. Liu, A. Mlayah, M-Y. Han; Janus Au-TiO_2 Photocatalysts with Strong Localization of Plasmonic Near-Fields for Efficient Visible-Light Hydrogen Generation, Adv. Mater. 24 (2012) 2310–2314.

106 M. Rycenga, C. M. Cobley, J. Zeng, W. Li, C. H. Moran, Q. Zhang, D. Qin, Y. Xia; Controlling the Synthesis and Assembly of Silver Nanostructures for Plasmonic Applications; *Chem. Rev.* 111 (2011) 3669–3712.

107 ZhangRPPhys13 X. Zhang, Y. L. Chen, R-S. Liu, D. P. Tsai; Plasmonic photocatalysis; *Rep. Prog. Phys*. 76 (2013) 046401– 046442.

108 K. Awazu, M. Fujimaki, C. Rockstuhl, J. Tominaga, H. Murakami, Y. Ohki, N. Yoshida, T. Watanabe; A plasmonic photocatalyst consisting of silver nanoparticles embedded in titanium dioxide; *J. Am. Chem. Soc.* 130 (2008) 1676–1680.

109 S. Linic, P. Christopher, D. B. Ingram; Plasmonic-metal nanostructures for efficient conversion of solar to chemical energy; *Nat. Mater.* 10 (2011) 911–921.

110 J. A. Schuller, E. S. Barnard, W. Cai, Y. C. Jun, J. S. White, M. L, Brongersma;Plasmonics for extreme light concentration and manipulation; *Nature Mater.* 9 (2010) 193–204.

111 B. G. Ershov, E. V. Abkhalimov, V. I. Roldughin, V. M. Rudoy, O. V. Dementva, R. D. Solovov; Adsorption of ozone and plasmonic properties of gold hydrosol: the effect of the nanoparticle size; *Phys. Chem. Chem. Phys.* (2015) DOI:10.1039/C5CP02326B

112 Growing and stability of gold nanoparticles and their functionalization by cysteine A. Majzik, R. Patakfalvi, V. Hornok, I. Dékány, *Gold Bull.* 42 (2009) 113–123.

113 J. K. Young, N. A Lewinski, R. J Langsner, L. C Kennedy, A. Satyanarayan, V. Nammalvar, A. Y Lin, R. A. Drezek; Size-controlled synthesis of monodispersed gold nanoparticles via carbon monoxide gas reduction; *Nanoscale Res. Lett.*, 6 (2011) 428–439.

114 N. Perkas, Z. Zhong, L. Chen, M. Besson, A. Gedanken; Sonochemically prepared high dispersed Ru/TiO_2mesoporous catalyst for partial oxidation of methane to syngas; *Catal. Lett.*103 (2005) 9–14.

115 Z. Zhong, S. Patskovskyy, P. Bouvrette, J. H. T. Luong, A. Gedanken; The surface chemistry of Au colloids and their interactions with functional amino acids; *J. Phys. Chem. B* 108 (2004) 4046–4052.

116 Z. Zhong, F. Chen, A. S. Subramanian, J. Lin, J. Highfield, A. Gedanken; Assembly of Au colloids into linear and spherical aggregates and effect of ultrasound irradiation on structure; *J. Mater. Chem.*, 16 (2006) 489–495.

117 E. Csapó, R. Patakfalvi, V. Hornok, L. T. Tóth, Á. Sipos, A. Szalai, M. Csete, I. Dékány; Effect of pH on stability and plasmonic properties of cysteine-functionalized silver nanoparticle dispersion; *Coll. Surf. B* 98 (2012) 43–49.

118 E. Csapó, A. Oszkó, E. Varga, Á. Juhász, N. Buzás, L. Kőrösi, A. Majzik, I. Dékány; Synthesis and characterisation of Ag/Au alloy and core (Ag)-shell(Au) nanoparticles; *Coll. Surf.* A 415 (2012) 281-287.

119 A. Majzik, L. Fülöp, E. Csapó, F. Bognár, T. Martinek, B. Penke, G. Bíró, I. Dékány; Functionalisation of gold nanoparticles with amino acids, β- amyloid peptides and fragment; *Coll. Surf. B* 81 (2010) 235 – 241.

120 A. Furube, L. Du , K. Hara , R. Katoh, M. Tachiya; Ultrafast Plasmon-induced electron transfer from gold nanodots into TiO_2 nanoparticles *J. Am. Chem. Soc.*, 129 (2007) 14852–14853.

121 A. Dawson, P. V. Kamat; Semiconductor−metal nanocomposites. Photoinduced fusion and photocatalysis of gold-capped TiO_2 (TiO_2/gold) nanoparticles; *J. Phys. Chem. B*, 105 (2001) 960–966.

122 L. Kőrösi, S. Papp, J. Ménesi, E. Illés, V. Zöllmer, A. Richardt, I. Dékány; Photocatalytic activity of silver-modified titanium dioxide at solid–liquid and solid – gas interfaces; *Coll. Surf. A* 319 (2008) 136–142.

123 L. Kőrösi, S. Papp, I. Dékány; Synthesis, structure and photocatalytic activity of titanium dioxide and some of its surface-modified derivatives; *Cat. Alter. En. Gen.* (2012) 459–489.

124 J. Chen, S.-C. Kou, C-S. Poon; Photocatalytic cement-based materials: Comparison of nitrogen oxides and toluene removal potentials and evaluation of self-cleaning performance; *Building Env.* 46 (2011) 1827–1833.

125 H. Guo, N. H. Kwok, H. R. Cheng, S. C. Lee, W. T. Hung, Y. S. Li; Formaldehyde and volatile organic compounds in Hong Kong homes: concentrations and impact factors, *Indoor Air* 19 (2009) 206–217.

126 T. Szabó, O. Berkesi,P-. Forgó, K. Josepovits, Y. Sanakis; D. Petridis, I. Dékány; Evolution of Surface Functional Groups in a Series of Progressively Oxidized Graphite Oxides; *Chem. Mater.* 18 (2006) 2740–2749.

127 D. Reyes-Coronado, G. Rodríguez-Gattorno, M. E. Espinosa-Pesqueira, C. Cab, R de Coss and G Oskam, Phase-pure TiO_2 nanoparticles: anatase, brookite and rutile; *Nanotechnol*. 19 (2008) 145605 – 145615.

128 Y. Shen, S. Yang, P. Zhou, Q. Sun, P. Wang, L. Wan, J. Li, L. Chen, X. Wang, S. Ding, D. W. Zhang; Evolution of the band-gap and optical properties of graphene oxide with controllable reduction level; *Carbon* 64 (2013) 157–164.

129 Y. Sang, Z. Zhao , J. Tian , P. Hao , H. Jiang , H. Liu, J. P. Claverie; Enhanced photocatalytic property of reduced graphene oxide/TiO_2 nanobelt surface heterostructures constructed by an in situ photochemical reduction method; *Small* 10 (2014) 3775–3782.

130 H. Zhang, X. Lv, Y. Li, Y. Wang, J. Li; P25-graphene composite as a high performance photocatalyst; *J. Am. Chem. Soc. Nano* 4 (2010) 380–386.

131 Y. Conga, M. Longa, Z. Cui, X. Li, Z. Donga, G. Yuana, J. Zhang; Anchoring a uniform TiO_2 layer on graphene oxide sheets as an efficient visible light photocatalyst; *Appl. Surf. Sci.* 282 (2013) 400–407.

132 A. Mathkar, D. Tozier, Paris Cox, P. Ong, C. Galande, K. Balakrishnan, A. L. M. Reddy, P. M. Ajayan, Controlled, stepwise reduction and band gap manipulation of graphene oxide; *J. Phys. Chem. Lett.* 3 (2012) 986−991.

133 H-J. Shin, K. K. Kim, A. Benayad, S-M. Yoon, H. Ki Park, I-S. Jung, M. H. Jin, H-K. Jeong, J. M. Kim, J-Y. Choi, Y. H. Lee; Efficient reduction of graphite oxide by sodium borohydride and its effect on electrical conductance; *Adv. Functional Mater*. 19 (2009) 1987-1992.

134 G. K. Ramesha, S. Sampath, Electrochemical reduction of oriented graphene oxide films: An *in situ* Raman spectroelectrochemical study; *J. Phys. Chem. C* 113 (2009) 7985–7989.

135 S. J. An, Y. Zhu, S. H. Lee, M. D. Stoller, T. Emilsson, S. Park, A. Velamakanni, J. An, R S. Ruoff; Thin film fabrication and simultaneous anodic reduction of deposited graphene oxide platelets by electrophoretic deposition; *J. Phys. Chem. Lett.* 1 (2010) 1259–1263.

136 K. Krishnamoorthya, M. Veerapandianb, G-S. Kima, S. J. Kima; A one step hydrothermal approach for the improved synthesis of graphene nanosheets; *Current Nanoscience,* 8 (2012) 934-938.

137 Y. Matsumoto, M. Koinuma, S.Y. Kim, Y. Watanabe, T. Taniguchi, K. Hatakeyama, H. Tateishi, S. Ida, Simple photoreduction of graphene oxide nanosheet under mild conditions, *J. Am Chem. Soc. Appl. Mater. Int.* 2 (2010) 3461–3466.

138 T. Wu, S. Liu, H. Li, L. Wang, X. Sun; Production of reduced graphene oxide by UV Irradiation; *J. Nanosci. Nanotechnol.* 11 (2011) 1–4.

139 G. Williams, B. Seger, P. V. Kamat; TiO_2-graphene nanocomposites. UV-assisted photocatalytic reduction of graphene oxide; *J. Am. Chem. Soc. Nano* 2 (2008) 1487–1491.

140 T. Szabó, Á. Veres, E. Cho, J. Khim, N. Varga, I. Dékány; Photocatalyst separation from water using graphene oxide/TiO_2 nanocomposites; *Coll. Surf. A* 433 (2013) 230– 239.

141 Y. Park, S-H. Kang, W. Choi; Exfoliated and reorganized graphite oxide on titania nanoparticles as an auxiliary co-catalyst for photocatalytic solar conversion; *Phys. Chem. Chem. Phys.,* 13 (2011) 9425–9431.

142 M. Tasbihi, C. R. Ngah, N. Aziz, A. Mansor, A. Zuhairi Abdullah, L. K. Teong, A. R. Mohamed; Lifetime and regeneration studies of various supported TiO_2 photocatalysts for the degradation of phenol under UV-C light in a batch Reactor; *Ind. Eng. Chem. Res.* 46 (2007) 9006-9014.

143 S-M. Lam, J-C. Sin, A. R. Mohamed; Parameter effect on photocatalytic degradation of phenol using TiO_2-P25/activated carbon (AC); *Korean J. Chem. Eng.* 27 (2010) 1109–1116.

144 Á. Veres, T. Rica, L. Janovák, M. Dömök, N. Buzás, V. Zollmer, T. Seemann, A. Richardt, I. Dékány; Silver and gold modified plasmonic TiO_2 hybrid films for photocatalytic decomposition of ethanol under visible light; *Catal. Today* 181 (2012) 156–162.

145 M. R. Nimlos, E. J. Wolfrum, M. L. Brewer, J. AFennell, G. Bintner; Gas-phase heterogeneous photocatalytic oxidation of ethanol: Pathways and kinetic modeling; *Environ. Sci. Technol.* 30 (1996) 3102–3110.

146 M. L. Sauer, D. F Ollis; Photocatalyzed oxidation of ethanol and acetaldehyde in humidified air**;** *J. Catal.* 158 (1996) 570–582.

147 Á. Veres, J. Ménesi, Á. Juhász, O. Berkesi, N. Ábrahám, G. Bohus, A. Oszkó, G. Pótári, N. Buzás, L. Janovák, I. Dékány; Photocatalytic performance of silver-modified TiO_2 embedded in poly(ethyl-acrylate-co methyl metacrylate) matrix; *Coll. Polym. Sci.* 292 (2014) 207–217.

148 R. Wang, K. Hashimoto, A. Fujishima, M. Chikuni, E. Kojima, A. Kitamura, M. Shimohigoshi, T. Watanabe, Photogeneration of highly amphiphilic TiO_2 surfaces, *Adv. Mater.* 10 (1998) 135–138.

149 N. Sakai, A. Fujishima, T. Watanabe, K. Hashimoto; Quantitative evaluation of the photoinduced hydrophilic conversion properties of TiO_2 thin film surfaces by the reciprocal of contact angle; 107 *J Phys. Chem. B* (2003) 1028–1035.

150 R. Tadmor; Line energy and the relation between advancing, receding, and Young contact angles; *Langmuir* 20 (2004) 7659–7664.

151 E. Chibowski, K. Terpilowski; Surface free energy of sulfur—Revisited: Yellow and orange samples solidified against glass surface; *J. Colloid Int. Sci.* 319 (2008) 505–513.

152 A. Kafizas, C. W. Dunnill, I. P. Parkin; The relationship between photocatalytic activity and photochromic state of nanoparticulate silver surface loaded titanium dioxide thin-films; *Phys. Chem. Chem. Phys.* 13 (2011) 13827–13838.

153 X. Pan, Y-J. Xu; Defect mediated growth of noble metal (Ag, Pt and Pd) nanoparticles on TiO_2 with oxygen vacancies for photocatalytic redox reactions under visible light; *J. Phys. Chem. C* 117 (2013) 17996–18005.

154 V. Subramanian, E. E. Wolf, P. V. Kamat; Catalysis with TiO_2/gold nanocomposites. Effect of metal particle size on the Fermi level equilibration; *J. Am. Chem. Soc.* 126 (2004) 4943–4950.

155 J. Lee, H. S. Shim, M. Lee, J. K. Song, D. Lee; Size-controlled electron transfer and photocatalytic activity of ZnO-Au nanoparticle composites*; J. Phys. Chem. Lett.* 2(2011) 2840–2845.

156 G. P. Smith; Photochromic glasses: Properties and applications; *J. Mater. Sci* 2 (1967) 139–152.

157 K. Kawahara, K. Suzuki, Y. Ohko, T. Tatsuma; Electron transport in silver-semiconductor nanocomposite films exhibiting multicolor photochromism; *Phys. Chem. Chem Phys.* 7 (2005) 3851–3855.

158 J. N. Yao, K. Hashimoto, A. Fujishima; Photochromism induced in an electrolytically pretreated MoO_3 thin film by visible light; *Lett. Nature* 355 (1992) 624–626.

159 H. Zhang, G. Wang, D. Chen, X. Lv, J. Li; Tuning photoelectrochemical performances of Ag−TiO_2 nanocomposites via reduction/oxidation of Ag; *Chem. Mater.*, 20 (2008) 6543–6549.

160 C. D. Wagner, W.M. Riggs, L. E. Davis, J.F. Moulder; Handbook of X-ray photoelectron spectroscopy; Perkin-Elmer Corp., Physical Electronic Division, Eden Prairie, MN, 1979.

161 I. M. Arabatzis, T. Stergiopoulos, M.C. Bernard, D. Labou, S.G. Neophytides, P. Falaras; Silver-modified titanium dioxide thin films for efficient photodegradation of methyl orange; *Appl. Catal. B* 42 (2003) 187–201.

162 X. Wang, S. Li, H. Yu, J. Yu, S. Liu; Ag_2O as a new Vis-light photocatalyst: Self-stability and high photocatalytic activity; *Chem. Eur. J.* 17 (2011) 7777-7780.

163 Y. Xu. M. Schoonen; The absolute energy positions of conduction and valence bands of selected semiconducting minerals; *Am. Mineral.* 85 (2000) 543–556.

164 D. Sarkar, C. K. Ghosh, S. Mukherjee, K. K. Chattopadhyay; Three dimensional Ag_2O/TiO_2 type-II (p−n) nanoheterojunctions for superior photocatalytic activity; *J. Am. Chem. Soc. Appl. Mater. Int.* 5 (2013) 331−337.

165 Á. Veres, J. Ménesi, C. Janáky, G. F. Samu, M. K. Scheyer, Q. Xu, F. Salahioglu, M. V. Garland, I. Dékány, Z. Zhong; New insights into the relationship between structure and photocatalytic properties of TiO_2 catalysts; *RSC Adv.* 5 (2015) 2421-2428.

166 H. Zhu, X. Gao, Y. Lan, D. Song, Y. Xi, J. Zhao; Hydrogen titanate nanofibers covered with anatase nanocrystals: A delicate structure achieved by the wet chemistry reaction of the titanate nanofibers; *J. Am. Chem. Soc.* 126 (2004) 8380-8381.

167 Y. Yu, D. Xu; Single-crystalline TiO_2 nanorods: Highly active and easily recycled photocatalysts; *Appl. Cat. B* 73 (2007) 166-171.

168 L. Shen, N. Bao, Y. Zheng, A. Gupta, T. An, K. Yanagisawa; Hydrothermal splitting of titanate fibers to single-crystalline TiO_2 nanostructures with controllable crystalline phase, morphology, microstructure, and photocatalytic activity; *J. Phys. Chem. C* 112(2008) 8809–8818.

169 G. A. Tompsett, G. A. Bowmaker, R.P. Cooney, J.B. Metson, K. A. Rodgers, J.M. Seakins; The Raman spectrum of brookite, TiO_2 (Pbca, Z = 8); J. Raman Spect. 29 (1995) 57 – 62.

170 K. Rajeshwar J. Ibanez, in Environmental Electrochemistry, Fundamentals and applications in pollution abatement, ed. K. Rajeshwar and J. Ibanez, Academic Press Inc, California, 1997, ch. 6, p. 541.

171 C. Janáky, N. R. de Tacconi, W. Chanmanee, K. Rajeshwar, Electrodeposited polyaniline in a nanoporous WO_3 matrix: An organic/inorganic hybrid exhibiting both p- and n-type photoelectrochemical activity; *J. Phys. Chem. C* 116 (2012) 4234-4242.

172 V. Thavasi, V. Renugopalakrishnan, R. Jose, S. Ramakrishna; Controlled electron injection and transport at materials interfaces in dye sensitized solar cells; *Mater. Sci. Eng. 63* (2009) 81–99.

173 H. Tang, K. Prasad, R. Sanjinés P. E. Schmid and F. Lévy; Electrical and optical properties of TiO_2 anatase thin films; *J. Appl. Phys.,* 75 (1994) 2042 – 2047.

174 B. Berglund, G. Clausen, J. de Ceaurriz, A Kettrup, T. Lindvall, M. Maroni, L. Mølhave, A. C. Pickering, U. Risse, H. Rothweiler, B. Seifert, M. Younes; Total Volatile Organic Compounds (TVOC) in indoor air quality investigations, Europen Commission, Indoor air quality & its impact on man; Report No 9 ISBN 92-828-1 078-X

175 L. Mølhave, B. Bach, O.F. Pedersen; Human reactions to low concentrations of volatile organic compounds; *Environ. Int.* 12 (1986) 167–175.

176 H. K. Hudnell, D. A. Otto, D. E. House, L. Mølhave; Exposure of humans to volatile organic mixture II. Sensory; *Environ. Health* 47 (1992) 31–38.

7. Acknowledgements

Foremost, I would like to express my sincere gratitude to my supervisor, Prof. Dr. Imre Dékány. I thank him for his guidance and for his invaluable professional and personal support he gave me throughout the years.

I would like to thank all my previous and present colleagues in the Department of Physical Chemistry and Materials Science for their technical and moral support. Special thanks to Judit Ménesi, Dr. László Janovák, Noémi Varga, Ádám Juhász, Dr. Tamás Ricza, Dr Nóra Ábrahám, Gabriella Bohus, Dr. Ottó Berkesi, Dr. Albert Oszkó, Dr. Gábor Pótári, Dr. Csaba Janáky and Gergő Samu who contributed to my publications with their useful work or advices. Furthermore, I would like to thank Viktória Varga and Dr Dániel Sebők for the valuable discussions. Dr. Tamás Szabó deserves special mention here who first supervised me as his master thesis student and he has shared a lot of knowledge with me ever since. I thank him for his time, patience and his kind support.

I am enormously grateful that I was given the opportunity to conduct a student attachment program at the Agency of Science Technology and Research (A*STAR) in the Institute of Chemical and Engineering Sciences, Singapore. I would like to express my deepest gratitude to Dr. Ziyi Zhong who gave me useful knowledge and supervision during the time I spent there and I would like to give my special thanks to Dr. Poernomo Gunawan for his guidance and friendship. I would also like to express my appreciation for my collaborators: Dr. Marc V. Garland, Dr. Martin Karl Schreyer, Dr. Fatma Salahioglu and Qisong Xu.

I am thankful for the financial support that was given by the Hungarian National Office of Research and Technology (NKTH) under contract no. TECH- 09-A2-2009-0129 (NANOSTER); by the European Regional Fund under "TAMOP-4.2.1/B-09/1/KONV- 2010-0005" and "TÁMOP-4.22.A-11/1/KONV-2012-0047". I also would like to acknowledge the Intergovernmental Science & Technology Cooperation between Hungary and South Korea (Project No. KR-8/2009) and the Mid-Career Researcher Program through a National Research Foundation grant funded by the Ministry of Education, Science and Technology of Korea (2011- 0029804) and A*STAR.

At last, but not least, I would like to thank the support and encouragement of my family and friends during the time of my Ph.D. work.

8. Summary

I have prepared and examined TiO_2-based photocatalysts and photocatalytic nanocomposites for the photocatalytic degradation of organic pollutants. The term *nanocomposite* refers to those heterostructured solids which contain two or more compounds and the size of at least of them is in the nanoscale range. This group of materials includes nanostructures with various chemical structures and properties, therefore they have a broad range of applicability, including heterogeneous catalysis. Their speciality is attributed to that the advantageous properties of these materials are merged thus giving better function.

Applicability of TiO_2 – graphene oxide (GO) nanocomposites (TiGO) as photocatalysts was studied in the photocatalytic degradation reaction of phenol in aqueous solution. As a result of optical shading of GO and surface loss, originated from the anchoring, the photocatalytic efficiency of TiO_2 slightly decreased. However owing to the very fast sedimentation of the nanocomposite, TiO_2 could be readily removed in a short amount of time which has a paramount importance in practical application. It was observed that under UV-light the GO converted into a graphene-like material (rGO) with a loss of many functional groups, but without the full restoration of the polyaromatic graphene structure. Despite the chemical transformation and low pH, the rGO held TiO_2 NPs anchored on its surface which suggests that the interparticle attractions were primarily van der Waals forces not electrostatic forces. These interactions could be reversed by strong mechanical impact, however, the process was reversible and the particles could be re-aggregated by gently shaking. TiGO-2, containing 2 wt% of GO was easily recovered after the photocatalytic cycle and reused 4 times without significant loss of the photocatalytic activity (~ 3%)

For practical reasons, it is very prevailing to immobilise catalyst NPs on a macroscopic surface (substrate, e.g. bottom and walls of the reactor), therefore endeavours to remove the photocatalyst after use can be omitted. The immobilising agent has to be suitable for the purpose from several points of view such as price, mechanical stability and preferably it should not interfere much with the activity of the photocatalyst. Polymers are widely applied as catalyst binders, however their limited UV-resistance can be a problem, especially in the presence of a photocatalyst which can be activated by the irradiating light. Furthermore, these materials are not porous thus complete coverage of the catalyst NPs can result in drastic decrease of photocatalytic activity. Application of controlled UV-irradiation cycles on the TiO_2/polymer nanocomposites can „activate”, that is, by partly destroying the polymer matrix can result in enhancement of photocatalytic activity. The rate of polymer degradation can also be controlled by addition of UV-resistant inorganic compounds into the nanocomposites which slow

down the degenerative processes in the polymer matrix and contribute to a more porous structure and good adsorption properties towards organic pollutants.

Addition of noble metal NPs to TiO_2 enhance the photocatalytic activity under UV-Vis irradiation which is partly owing to the plasmonic absorption of Vis light photons of noble metal NPs and more so the enhanced rate of transfer of charge carriers through the metal/semiconductor interface limiting the recombination process. Ag NPs deposited on the surface of TiO_2 show interesting photochromic properties and with the change of oxidation state which depends on the wavelength of the irradiating light source. Photocatalytic activity of various $Ag_x(O)$-TiO_2 samples, obtained from different sources of $Ag_x(O)$ NPs possessing different oxidation states, were compared. The difference was an average less than 3% in the conversion rates. It indicated that neither the preparation method (*in situ* deposition of physical mixing) nor the state of oxidation of silver did not result in drastic variations of the photocatalytic activity under UV-Vis irradiation.

Crystalline structure and morphology of TiO_2 samples, obtained from the acidic hydrothermal treatment of H-TNFs, were varied by changing the acid concentration in the reaction medium. Anatase, brookite, finally rutile rich samples were formed with various morphologies. The band gap energies were shifted towards lower band gap energies as the rutile phase was building up. The electron-transport processes and the rate of charge carrier formation/recombination processes fundamentally affect the photocatalytic activity. Photoelectrochemical measurements served information about these factors which correlated well with the photocatalytic tests.

Finally, the prototype of an air cleaning device for indoor use was constructed using Vis-light emitting LEDs and photocatalytic coating of the inner walls using Ag-TiO_2 immobilised in polymer. According to the ethanol photocatalytic tests, the device can be used to decompose VOCs above the concentration of average indoor VOC content.

9. Összefoglalás

Munkám során TiO_2-alapú fotokatalizátorokat és fotokatalitikus nanokompozitokat állítottam elő és vizsgáltam azok alkalmazhatóságát szerves szennyezőanyagok fotokatalitikus lebontására. Nanokompozit alatt értünk minden olyan két vagy több szilárd fázisból álló heterogén anyagot, amelyben legalább az egyik fázis a nano mérettartományba esik. Ezen anyagcsoportba változatos kémiai szerkezetű és tulajdonságú anyagok sorolhatók, ennek köszönhetően felhasználási lehetőségeik nagy teret hódítanak a heterogén katalízis területén is. Népszerűségük annak köszönhető, hogy két vagy több anyag hasznos funkcióit ötvözve olyan tulajdonságokat nyújtanak, amelyekre önmagában egyik anyag sem lenne képes; más szavakkal, szinergizmus lép fel.

TiO_2-grafén-oxid (TiGO) nanokompozitok fotokatalitikus alkalmazhatóságát vizsgáltam folyadék/szilárd határfelületen, fenol oldat fotodegradációján. Bár a GO lamellák optikai árnyékoló hatása és a felületi rögzítésből adódó felületvesztés miatt a katalizátor valamelyest veszített a hatékonyságából, azonban percek alatt bekövetkező ülepedése a katalizátor gyors elválasztását teszi lehetővé, aminek pedig a gyakorlati felhasználás szempontjából óriási jelentősége van. Megfigyeltem, hogy a GO vizes közegben, a felületén megkötött TiO_2 jelenlétében, UV bevilágítás hatására átalakul grafén-szerű, szén síkhálóval és kevés felületi funkciós csoporttal rendelkező redukált anyaggá (rGO). A kémiai átalakulás ellenére a rGO felületén kötve tartja a TiO_2 részecskéket. Ebből következik, hogy a fotokatalizátor részecskék között fellépő elektrosztatikus kötőerők gyenge diszperziós, van der Waals kötések egészülnek ki. A részecskék közti vonzó hatás erős mechanikai hatásra megszüntethető, ugyanakkor a kötőerők nem szűnnek meg véglegesen és a folyamat reverzibilis jellegéből adódóan a részecskék enyhe kevertetéssel újra koaguláltathatók. A 2 m/mt%-ban GO-t tartalmazó nanokompozit könnyen visszanyerhető volt és fotokatalitikus hatékonysága négy egymást követő ciklus után sem romlott.

Praktikus okokból közkedvelt megoldás a katalizátor makroszkópos felületen való rögzítése (pl. a reaktor falán, alján), így nem kell külön időt és energiát fordítani annak eltávolítására a fotokatalitikus ciklus végén. A rögzítő anyagnak több szempontból eleget kell tennie a kívánalmaknak: legyen olcsó, ellenálló és lehetőleg minél kevésbé csökkentse a fotokatalizátor hatékonyságát. A polimer alapú rögzítő anyagok igen népszerűek katalizátor részecskék immobilizálására is, azonban gyakran probléma azok csökkent UV-ellenálló képessége, különösen fotokatalizátor jelenlétében. Továbbá, mivel ezek nem pórusos anyagok, a katalizátor-részecskék teljes beborításával óhatatlanul csökkentik azok fotokatalitikus aktivitását. Szabályozott idejű és energiájú UV-kezeléssel a TiO_2/polimer réteg „elő-aktiválható”, így a kompakt polimer-réteg integrációjának részleges megbontásával növelhető a filmek fotokatalitikus aktivitása. A folyamat mértéke szabályozható továbbá UV-fényre nem bomló, szervetlen agyagásványok hozzáadásával, amelyek valamelyest csökkentik a polimer degradációját, ugyanakkor pórusosabbá teszik a filmet és jó adszorpciós tulajdonságaikkal hozzájárulnak a szerves szennyezők megkötéséhez.

Nemesfém nanorészecskék hozzáadásával növelhető a TiO_2 hatékonysága UV-látható fény alatt, mely részben a nemesfém részecskék plazmonikus sajátságának, részben pedig a fém/félvezető határfelületen megvalósuló jobb elektron-transzportnak köszönhető, amely csökkenti a töltéshordozók rekombinációra való hajlamát. A TiO_2 felületen depozitolt Ag azért érdekes, mert a besugárzó fény hullámhosszával hangolható az oxidációs állapota. Különböző oxidációs állapotú (Ag_2O, AgO és Ag)-TiO_2 filmek fotokatalitikus aktivitását összevetve nem találtam jelentős különbséget (± 2,5%

konverzió) etanol fotooxidációján. Úgy találtam, hogy sem az előállítás jellege (*in situ* depozíció vagy fizikai keverés), sem az előzetes fénybevilágítás nem eredményez jelentős különbséget azonos Ag (m/m_{Ag}%=0,5) tartalmú filmek esetében UV-látható megvilágítás alatt.

TiO_2 minták morfológiája és kristályszerkezete jól hangolható a sav koncentrációjának változtatásával hidrogén-titanát nanoszálak savas hidrotermális reakciója során. .Anatáz-brookit-, illetve rutil-dús minták keletkeztek a savkoncentráció növelésével, melynek következtében a minták változatos alakzatokban kristályosodtak ki. A minták optikai tulajdonsága és a számolt tiltott sáv energiák jól követték a mintában jelen levő többségi polimorf jellemző irodalmi értékét. Az elektron-transzport folyamatok és az elektron-lyuk rekombináció mértéke kétség kívül meghatározó faktora a fotokatalizátor aktivitásának. A fotovoltammetriás mérések erről adtak információt, ami jól korrelált a fotokatalitikus tesztekkel.

Végezetül, egy belső terek levegőjének tisztítására alkalmas berendezés került összeállításra beépített látható fényt emittáló LED-ekkel és polimerben rögzített Ag-TiO_2 fotokatalitikusan aktív bevonattal. A berendezés hatékonynak bizonyult az átlagos könnyen illó szerves koncentrációknak három nagyságrenddel nagyobb koncentrációjú etanol gőz fotokatalitikus degradációjára.

10. Appendices

Appendix 1
Emission spectra of light sources are introduced here:

a) GCL303T5/type 2 Low-pressure mercury lamp was used for photooxidation of EtOH vapour on $Ag_x(O)$ and Au-modified TiO_2 and nanocomposite films built with organic and inorganic supports

b) GCL303T5/type 1 Low-pressure mercury lamp was used for photooxidation of EtOH vapour on HPT-TiO_2 samples

c) GCL303T5VH/OH Low-pressure mercury lamp was used to destroy the polymer ("UV-treatment")

d) TQ-150 High-pressure Mercury lamp was used for photocatalytic degradation of phenol solution

e) Vis-emittig LED light sources: *Ledium* LED (λ_{max} = 405 nm) was used in the air cleaning device and LED from GE was used to study the optical behaviour of $Ag_x(O)$ on TiO_2

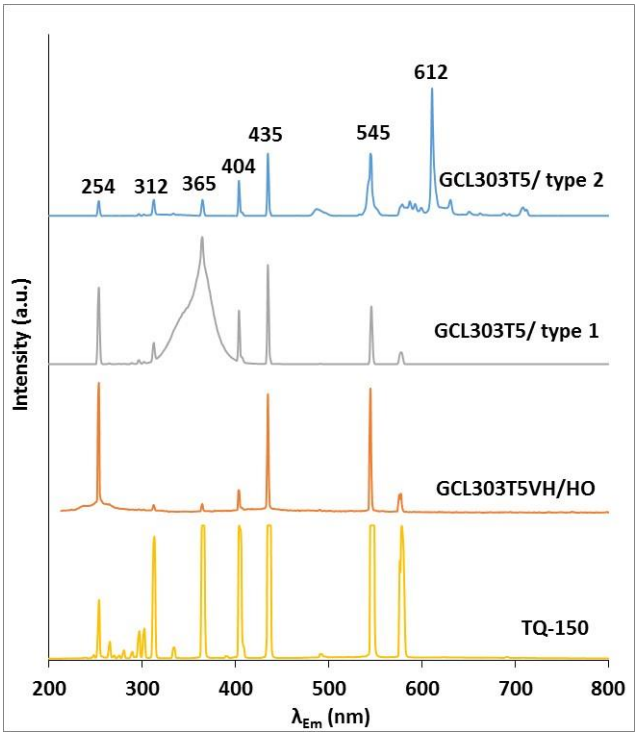

a)

b)

c)

d)

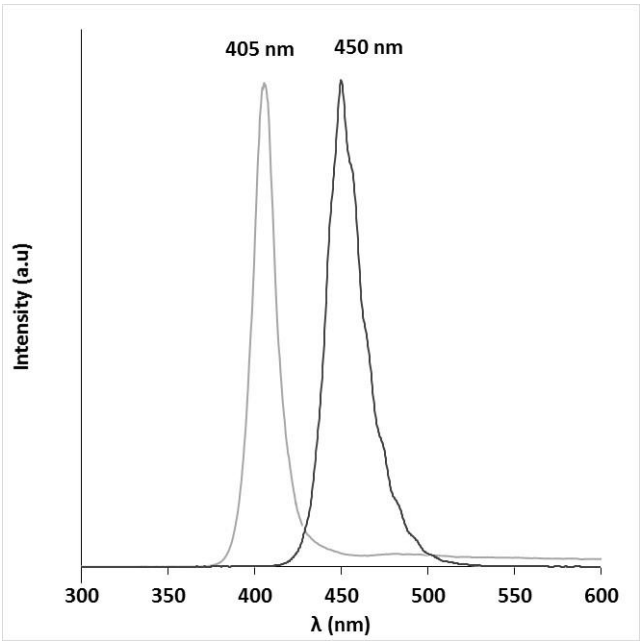

e)

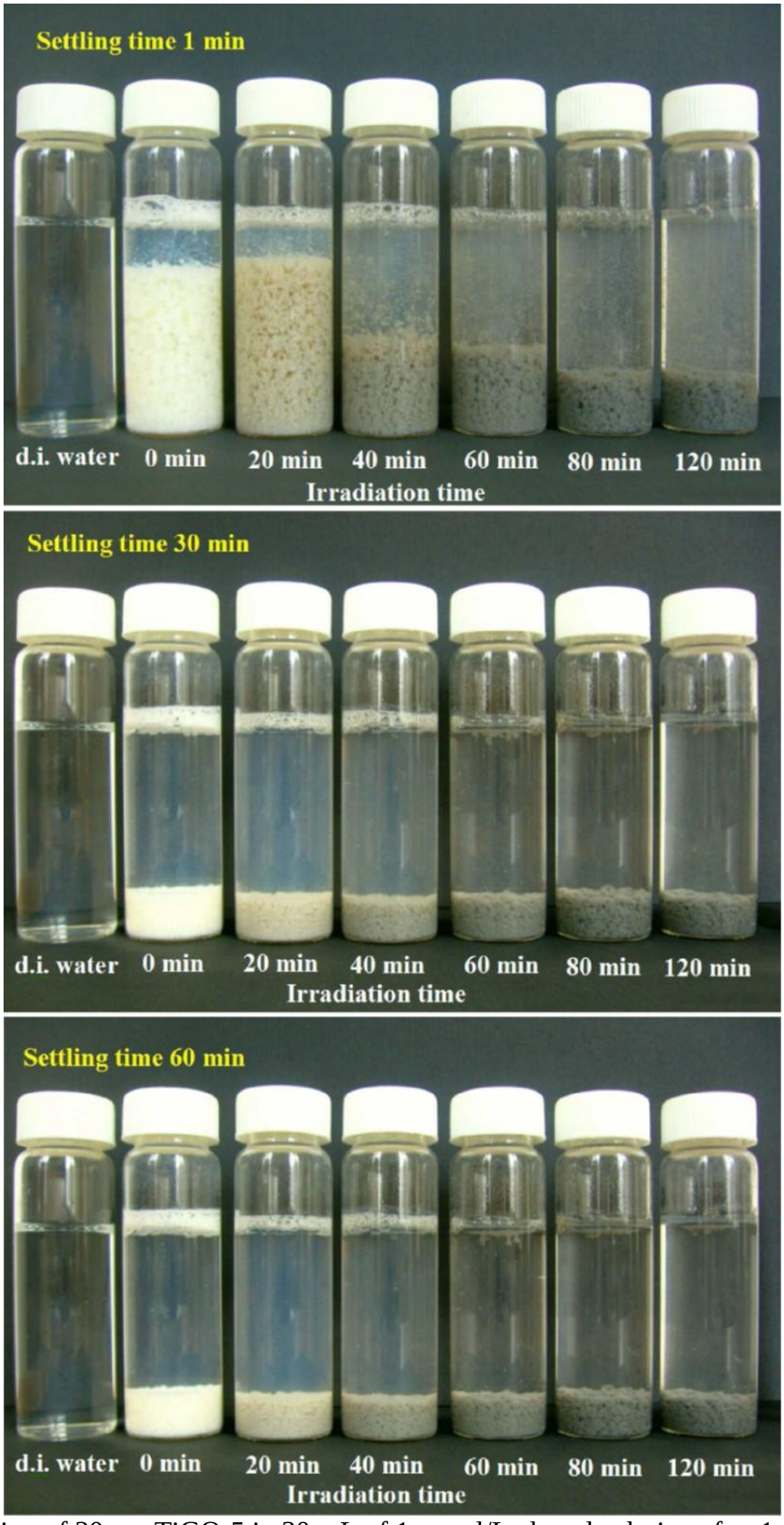

Appendix 2 Settling of 30 mg TiGO-5 in 30 mL of 1 mmol/L phenol solution after 1 min (top), 30 min (middle) and 60 min (bottom) at different irradiation times.